Cassini Program

Saturn Atmospheric Modeling Working Group Final Report

D-104871

Revision 0

Prepared By:

Scott G. Edgington Date
Cassini Deputy Project Scientist

Approved By:

Earl Maize Date
Cassini Project Manager

December 2019

Jet Propulsion Laboratory
California Institute of Technology
4800 Oak Grove Drive

Pasadena, CA 91109-8099

Change Log

Revision	Date	Changed By	Section(s)	Description
0	December 2019	S. Edgington		Document created

Table of Contents

Saturn Atmospheric Modeling Working Group Final Report

Darrell F. Strobel[1], Tommi T. Koskinen[2], Roger V. Yelle[2], Erick J. Sturm[3], Earl H. Maize[3], Scott G. Edgington[3,4]

[1]The Johns Hopkins University, Baltimore, MD
[2]Lunar and Planetary Laboratory, University of Arizona, Tucson, AZ
[3]Jet Propulsion Laboratory, California Institute of Technology, Pasadena, CA
[4]Corresponding Author: scott.g.edgington@jpl.nasa.gov

Acknowledgement: The research was carried out at the Jet Propulsion Laboratory, California Institute of Technology, under a contract with the National Aeronautics and Space Administration.

Preface

by Scott G. Edgington

This report reflects the Cassini Project's efforts to understand Saturn's atmosphere above the 1 bar (1 atmosphere) pressure level. With these goals in mind, the Saturn Atmospheric Modeling Working Group (SAMWG) was formed by Project Scientist, Dennis Matson, and consisted any Cassini scientist who wished to contribute. Andy Ingersoll, Darrell Strobel, and Scott Edgington were to coordinate these efforts.

The key objectives of the SAMWG were to:

- A. Determine of the shape of the 1 bar pressure level surface
  - see appendix for more detail.
- B. Characterize the upper atmosphere and for assessment of Cassini last 22 Proximal Orbits.
  - The bulk of this report
- C. Determine from near-IR and visible occultations the extinction levels to provide guidelines for Constraint Monitor Table (CMT) management
  - It was agreed that the project should continue to use the occultation timing based on the Tour Atlas (100 mbar NAIF reference surface) as their baseline for CMT management

The work of the SAMWG continued until the very end of the mission as new data collected by Cassini helped to inform its recommendations. Reports were made at least three times a year to the Saturn Working Group and Project Science Group and to Project Mission Planning when appropriate. This final report is a summary of these efforts. Much of it has been written by Strobel, et al. with appendixes from Erick Sturm (Jet Propulsion Laboratory) and Dr. Tommi Koskinen (Lunar and Planetary Laboratory, University of Arizona). Additional appendices rounding out the report (The Shape of Saturn and Saturn's Upper Atmosphere) have been added. We hope that meets your needs and interests.

Best Regards,
Scott G. Edgington, Ph.D.
Cassini Project Scientist/Saturn Target Working Team Lead/CIRS Investigation Scientist
Jet Propulsion Laboratory, California Institute of Technology

Timeline of key developments

- Winter 2007: Extended mission tour with Proximal Orbits approved by the Project Science Group
- Winter/Spring 2009: NASA approves Cassini's Solstice Mission
- Fall of 2009: Edgington/Atreya atmospheric model released based on Voyager data and UVIS occultations analyzed by Shemansky and Voyager Radio Science occultations Late 2009 - The Saturn Atmospheric Modeling Working Group formed.
- Early 2011: Shape of Saturn provided to the Cassini Project based on gravity results and Cassini Radio Science occultations (analyzed by Schinder and Flasar)
- August 2013: Strobel upper atmospheric model proposed based on reanalysis of UVIS data by Tommi Koskinen
- March 2014: Tommi Koskinen discovers Saturn's upper atmosphere is expanding, prompting the Project to consider various action scenarios for pop-up scenarios. Towards the end of the mission, the atmosphere ceased its upward trend.
- 2015 Onward: Saturn's atmosphere levels off, but does not retreat back to equinox state.
- April thru September 2017 - Cassini's 22 Proximal Orbits executed.

SAMWG Report

By

Darrell F. Strobel, Tommi T. Koskinen, Roger V. Yelle,

Erick J. Sturm, Earl H. Maize, Scott G. Edgington

I. Table of Contents

II. Executive Summary

This report is a legacy product of the Cassini Mission to document the plans, preparation, and execution of the Grand Finale Orbits 288-293 in 2017. It is not an engineering or scientific article in the normal sense, but more analogous to a personal history by the key participants in ensuring the successful execution of these orbits. It is highly recommended that readers who want access to data from these orbits to not use this report as a source, but rather go to NASA's Planetary Data System and published journal articles referenced in this report. This report was finalized approximately one year after the data was taken on these orbits and when the first data analyses appeared in journal publications. However, the interpretations of this extraordinary data set were in their infancy in many instances and still lively debated when the report was completed.

We found a density difference between non-invasive UVIS EUV stellar occultation measurements before the Grand Finale orbits and invasive, in situ density measurements made by the INMS, NAV and inferred from AACS in the southern hemisphere on Orbits 288-292 at latitudes of closest approach/ periapsis (~ -4°to -6°). On average the latter measurements were overall 2.8 times denser than inferred from the UVIS stellar occultation measurements acquired from 2014 to March 28, 2017 at these same latitudes. These stellar occultation measurements of consistent, unchanging density profiles within their error bars were used to develop the Strobel prediction model to fly the Grand Finale low orbits. The density differences between INMS and UVIS are beyond their respective reported error bars. The most plausible explanation is secular time variability in Saturn's thermosphere over the period from March 28, 2017 to August 14, 2017, the date of Proximal Orbit 288. Other explanations such as local solar time variability and some unknown significant process(s) associated with hypersonic flight through the thermosphere were deemed more implausible.

The Orbits 288-292 were selected to fly through the atmosphere at closest approach/ periapsis with factor of five margins in density. Based on the average of the measured in situ densities, which were higher by a factor of 2.8, the actual margin was only about 1.8 putting the Cassini spacecraft squarely in the "Goldilocks zone" where attitude control authority was maintained and the instruments were able to maximize their scientific return from Saturn's upper atmosphere.

III. Statement of Problem: Flying Through Saturn's Variable Atmosphere

The Cassini spacecraft (S/C) flew through Saturn's upper atmosphere that has a rotational velocity of approximately 10 km s^{-1} during Revs. 288-292 at an inertial speed of approximately 34 km s^{-1}. The center of mass velocity of H_2 molecules with respect to the S/C in the atmosphere was approximately 30 km s^{-1} and the kinetic energy of colliding H_2 molecules was ~ 9 eV, exceeding their dissociation energy by a factor of 2. The temperature of the H_2 molecules was expected to be in the range of 350-400 K with a sound speed of ~ 1.5 km s^{-1} with the S/C flying at a hypersonic Mach number ~ 20. For higher mass numbers, e. g. mass 28, in the exosphere at 34 km s^{-1}, the center of mass kinetic energy is 6 eV per amu and if upon impact the kinetic energy were equally partitioned among all degrees of freedom, it would be equivalent to a temperature of 1-2 million degrees.

From the AACS inferred torque on the S/C for Revs 288-292, the peak mass densities were in the range of (2.37-3.62) x 10^{-11} kg m^{-3}. The Cassini S/C has a diameter of ~ 5 m and length of 7 m and I take L = 6 m. The Knudsen number Kn is equal to the mean free path (mfp) divided by L and the mean free path is best calculated with the collision cross section from viscosity. The Knudsen number for the peak mass density, 3.62 x 10^{-11} kg m^{-3}, is 49 if I take the S/C temperature to be the atmospheric temperature of ~ 380 K, but if T S/C = 75 K, the Kn = 36. However at hypersonic velocities, the S/C is in essence a snowplow piling up molecules in front of it by a factor ~ S/C Mach number Msc = 47 for T S/C = 75 K and Msc = 21 for T S/C = 380 K. (The volume in front of the spacecraft with length on the order of L is filled by the S/C velocity and depleted by the thermal velocity assuming diffuse reflection, i. e., the enhancement factor is ~ Mach number.) This results in a decreased Knudsen number Kn_{sp} (sp for snowplow) = 1.3 for T S/C = 75 K and ~ 4 for T S/C = 380 K. Thus along the highest densities part of the S/C trajectory at C/A, the flow is in the transition regime: where the mean free path, mfp, is comparable to the dimensions of the S/C and collisions between molecules must be taken into account ($Re^{-1/2}$ < Kn < 10, where Re is the Reynolds number $\propto$ Msc/Kn_{sp}) rather than free molecular flow assumed in the data reduction and analysis. DSMC simulations of Space Shuttle reentry yield this density enhancement but with no net effect on the drag coefficient (Rault, 1994). Similarly, DSMC simulations of the Galileo Probe entry into Jupiter's atmosphere yield the density enhancement in the transition regime with a minor blip in the drag coefficient, probably due to pyrolysis of the heat shield, but an otherwise smooth drag coefficient through transition regime (Haas and Milo, 1995). The conclusion from these DSMC simulations is that there are competing effects that essentially self-cancel, such as scattering molecules that would not intersect the S/C into the S/C, whereas the molecules in the snowplow section scatter molecules that would intersect the S/C away. In comparison to this invasive method of determining the atmospheric density, the solar and stellar absorptive occultation method is non-invasive and self-calibrating. The intensities of the EUV/FUV radiation from the Sun and stars are linear, so no nonlinear effects need to be considered. Thus the statement of the problem is why are the non-invasive measurements by UV stellar occultations at radial distances and latitudes of periapsis and C/A for Revs 288-292 with no obvious time variability over the prior 3 years yield densities in the range of 2.3-3.1 lower than inferred from the invasive Mach 20 measurements by torque (AACS) and drag (NAV) on the S/C and by the onboard INMS. It is also surprising that INMS is in better agreement with AACS and NAV in Saturn's H_2 upper atmosphere than Titan's N_2 upper atmosphere.

IV. Data Available for Tackling the Problem

1. EUV Stellar and Solar Occultations (Full report in appendix and Executive Summary here)

Executive Summary (T. T. KOSKINEN, R. V. YELLE, D. F. STROBEL)

The density and temperature in Saturn's thermosphere were monitored regularly from 2005 to 2017 by UV solar and stellar occultations observed by the Cassini/UVIS instrument (e. g., Koskinen et al., 2013, 2015, 2016; Koskinen and Guerlet, 2018). In particular, stellar occultations near the equator were used to construct the engineering atmosphere model (Sec. V.1) that was used in planning the Grand Finale orbits and final plunge. The purpose of this appendix is to provide an overview of the stellar occultation data analysis procedure that summarizes and expands on the information already available (Koskinen et

al., 2015). This report focuses on the retrieval of H_2 densities and temperatures from stellar occultations in the EUV channel of the UVIS instrument that were relevant to the engineering model. A list of the relevant occultations is given in Table 1 of the Appendix and includes a brief discussion of trends based on the occultations denoted by the asterisk that primarily guided our expectations of the state of the atmosphere during the last orbits of the mission in the summer/fall of 2017. In general, results from occultations through the end of 2015 have been published (Koskinen et al., 2015; Koskinen and Guerlet, 2018). At the time of writing, results for occultations from 2016-2017 are unpublished.

If the pointing is stable during the occultation, the star remains at the same location on the detector and there is no need to calibrate the data to calculate transmission. Stable occultation experiments are essentially self-calibrating and highly repeatable. Most of the Cassini Saturn occultations are stable. Evidence for small pointing drifts were found in only a few occultations that have been excluded from published analyses. The occultation data are available through the PDS Atmospheres Node.

The uncertainty in temperature is the most significant source of uncertainty in the retrieved density profiles. For example, the formal uncertainty in some of the best occultations near 5° S is 10% at 915 km, 10% at 1500 km and 13% at 1800 km. We conclude based on these uncertainties and our exploration of the rest of the data that an overall uncertainty of 20-30 % captures the uncertainty in the number densities retrieved with the iterative retrieval below 2000 km for an effective altitude resolution of 30 km.

In general, these results indicate that Saturn's low-latitude thermosphere has exhibited relative stability during the four years leading to the Grand Finale. This is all the more remarkable when one considers the fact that solar heating is negligible in the thermosphere, which is instead believed to be heated by more transient mechanisms such as waves or redistribution of energy from the aurora, both of which are expected to be variable. Our results demonstrate that the heating mechanism in Saturn's thermosphere must operate continuously over long time scales while producing only small perturbations to the mean state of the atmosphere on short time scales.

2. Extrapolation of Shape of Saturn’s 1 bar Pressure Level

Data taken by the Cassini spacecraft was recorded in a spherical coordinate system referenced to the center of Saturn, which is the most oblate planet in our solar system. It is useful sometimes to display data by removing the planet’s shape factor and use an altitude scale referenced to the 1 bar pressure surface. For the UVIS stellar occultation data, the 1 bar pressure surface was taken from Anderson and Schubert (2007). One of us (DFS) occasionally used unpublished Cassini RSS radio occultation values as a check. The differences among the various sources were at most 15 km and in most instances fewer than 10 km. Given that a typical scale height of the thermosphere at periapsis on Orbits 288-292 was 150 km the conversion of radial distance to altitude was accurate enough for the purposes of this report.

V. Science Analysis

1. The Strobel Model

The Strobel Model development began in 2010 and was initially presented at the June 2010 PSG meeting in Munich. Rather than start at the 1 bar level and build a model upward to the ~ 1 nbar level, some 21 pressure scale heights above the 1 bar surface, I started with the Voyager solar and stellar occultations that were acquired at equatorial latitudes and recently reanalyzed by Vervack and Moses (2015, preprint available in 2010) as shown in Fig. 1, until Cassini UVIS occultation data became available.

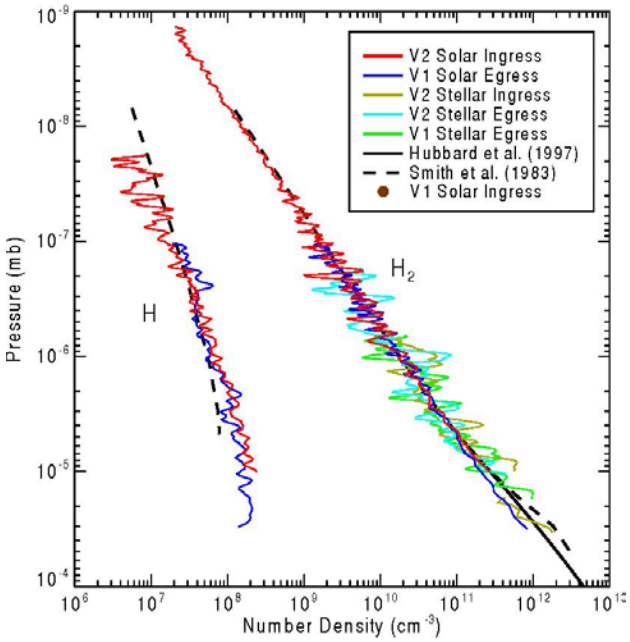

Figure 1. Density profiles of H_2 and H retrieved by Vervack and Moses (2015) from five low to mid latitude Voyager/UVS occultations. The results are compared with previous retrieval by Smith et al. (1983) and the density profile retrieved by Hubbard et al. (1997) from a ground-based stellar occultation. The figure is from Vervack and Moses (2015).

From these density profiles and CIRS density, pressure, and temperature data made available by Sandrine Guerlet, I constructed Fig. 2, which located the S/C tumble density level at a radial distance of 61,714 km at 3.8 N and -4.2 S (brown line) and for the then available UVIS 15.2° N stellar occultation at a radial distance of 61,150 km.

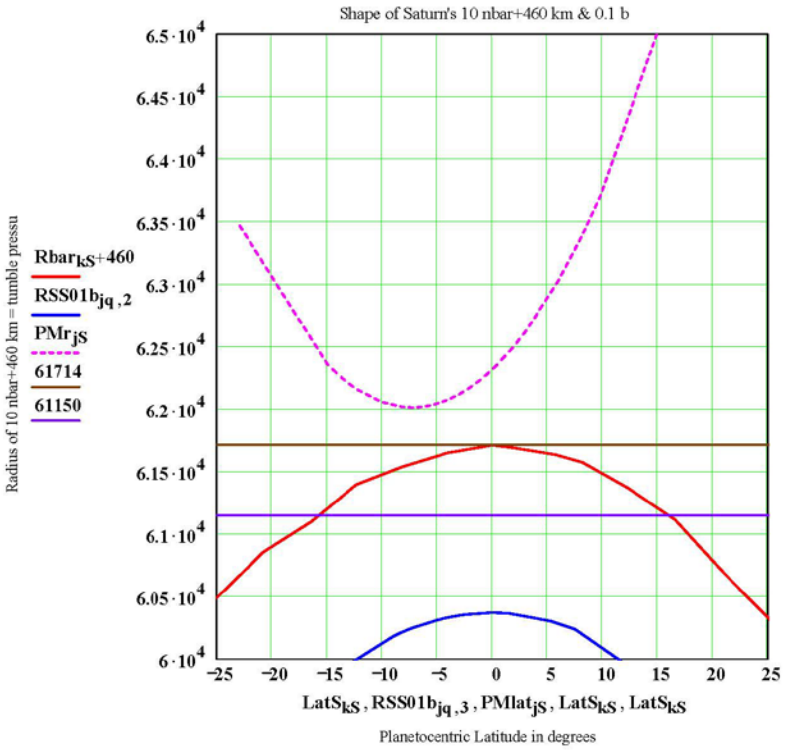

Figure 2. The blue line is the radius of the 0.1 bar surface from Radio Science (RSS) occultation measurements, the red line is the 10 nbar surface constructed using the RSS 0.1 bar surface and CIRS measurements of stratospheric pressure surfaces to which 460 km was added to the radius of the lowest (highest) CIRS pressure surface to obtain the radius of the Voyager UVS pressure from the V2 stellar egress atmosphere (3.8° N) and V1 stellar egress atmosphere (- 4.8° S) denoted by the brown line. The purple line is the tumble density level at 15.2° N from a UVIS stellar occultation. Note that August 27, 2017 trajectory is displayed by the dash magenta line. It is clear from this plot that the needed UVIS occultation data was confined to the latitude range of -10° S to the equator and from the oblate spheroidal shape of the atmosphere the highest densities would be equatorward of periapsis. See text for more description.

As more UVIS occultation data became available and analyzed by Tommi Koskinen (see appendix, Koskinen et al. 2013; Koskinen et al. 2015) I was able to construct better models of the critical tumble density surface and the ½ tumble density surface. The determination of the critical tumble density underwent a number of iterations and eventually was constrained to have the 3σ value of 6.5×10^{-11} kg m^{-3}. During these iterations I finally decided to adopt a canonical ½ tumble density value of 2.525×10^{-11} kg m^{-3}, so I did not have to update previous figures and this density was selected as the highest value that should be reached on any Grand Finale trajectory, except the final plunge. In Fig. 3, UVIS data analyzed by Koskinen et al. (2013, 2015) are shown at their respective planetocentric latitudes.

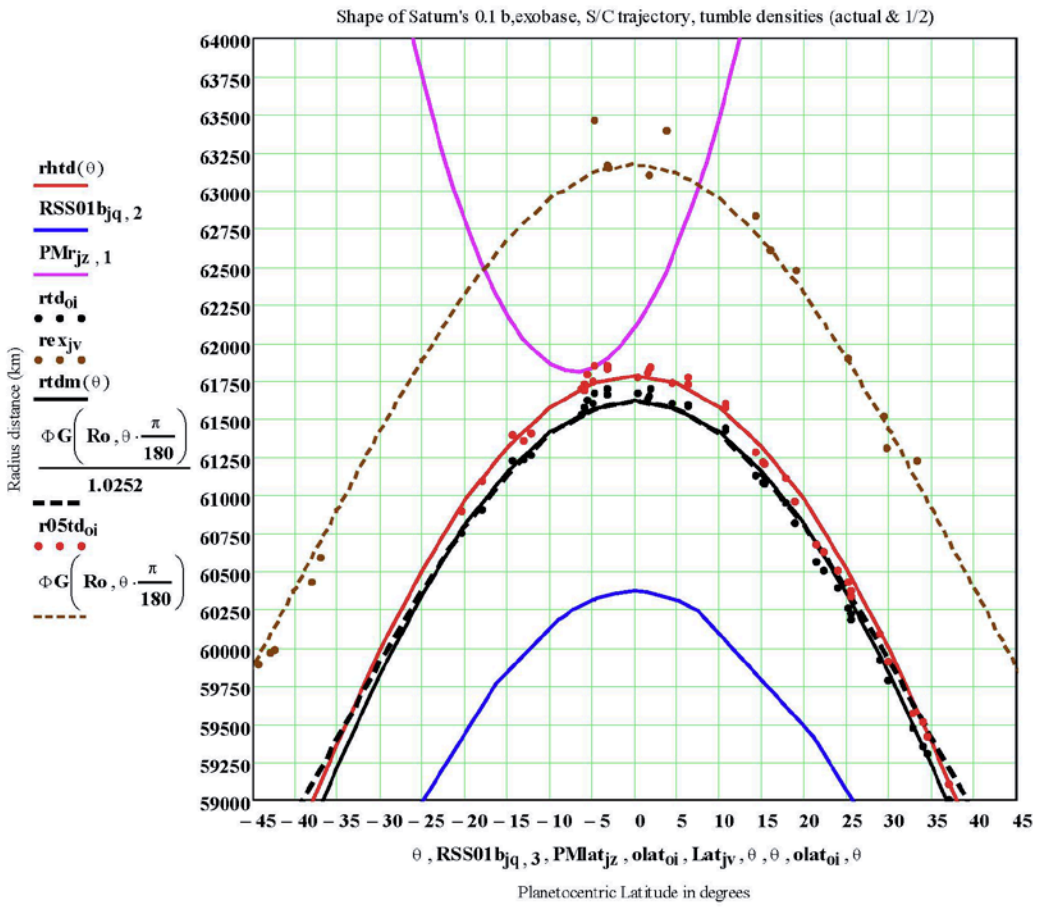

Figure 3. Surfaces are plotted as radial distance vs planetocentric latitude. The trajectory of Proximal Mission Orbit on 2017 August 27 is shown by magenta line. The red solid line is the constant n(H2) = 7.64 x 10^{9} cm^{-3} surface, i. e., the "1/2" tumble density (= 2.525 x 10^{-11} kg m^{-3}) in my simple model, whereas the red dots are the "1/2" tumble density points, the actual tumble density points (= 6.5 x 10^{-11} kg m^{-3} = 1.96 x 10^{10} H_2 cm^{-3}) are black dots, all from UVIS occultations, and the black solid line is my simple model of the tumble density surface. The brown dashed line is a rough analytic fit to exobase surface with brown dots from solar occultations (Koskinen et al. 2013). The black dashed line is the exobase surface divided by 1.0252 to show the shapes of the exobase and tumble density surfaces overlap at equatorial latitudes (± 15°). The blue solid line is the 0.1 bar surface.

For every UVIS stellar occultation that acquired data relevant to the 2017 August 27 trajectory below the exobase, an Excel file was maintained for equatorial occultations (Fig. 4). You will note that around spring equinox, which occurred 11 August 2009, the altitudes of the ½ and critical tumble densities were higher than later as the seasonal variation was headed for summer solstice in the northern hemisphere.

UVIS Stellar Occultations that cross Revs. 288-292 below the exobase with locations of "1/2" and "actual" engineering tumble densities

ID	Year	PC Lat	1 bar radius	r 0.01 nb	1/2 Tum den radius	1/2 Tum den altitude	tumble den radius	tumble den altitude	T_∞	Date	LST
		deg.	(km)	(km)	(km)	(km)	(km)	(km)	(K)		
ST30	2008	1.79	60265	62576	61837	1572	61702	1437	404	12/16/2008	19:04
ST32	2009	-3.31	60246	62625	61833	1587	61658	1412	427	1/3/2009	18:36
ST34	2009	-3.21	60247	62627	61850	1603	61703	1456	426	1/22/2009	18:35
ST35	2009	-5.6	60208	62539	61795	1587	61619	1411	407	1/31/2009	09:41
ST37	2010	-4.8	60228	62649	61847	1618	61671	1443	421	7/5/2010	07:09
ST42	2014	-5.91	60197	62343	61730	1533	61573	1376	402	10/3/2014	09:48
ST46	2015	1.65	60275	62476	61834	1559	61647	1372	383	2/18/2015	
ST61	2016	4.36	60236	62385	61735	1499	61603	1367	411	2/15/2016	
ST62	2016	1.45	60277	62413	61805	1528	61636	1359	361	2/15/2016	
ST64	2016	0.4	60282	62410	61774	1492	61668	1386	371	3/6/2016	
ST66	2016	-6.22	60191	62367	61695	1504	61530	1339	401	12/5/2016	
ST67	2016	-6.01	60196	62332	61687	1491	61577	1381	403	12/19/2016	
ST68	2017	-13.1	59888	61970	61358	1470	61237	1349	391	1/9/2017	
ST69	2017	-4.95	60224	62340	61745	1521	61603	1379	387	3/28/2017	

"1/2" tumble density = 2.525 E-11 kg/m^3 ; tumble density = 6.5 E-11 kg/m^3

"1/2" tumble density = 7.64 E09 n(H2) (cm^{-3}); tumble density 1.96 E10 n(H2) (cm^{-3})

Figure 4. UVIS stellar occultations that acquired data relevant to the 2017 August 27 trajectory below the exobase.

As the data became available, I constructed an analytic model to capture the essence of the data at the critical density levels where atmospheric drag and torque on S/C would be important and the density structure especially in the range of from ½ to actual tumble density. The analytic expression that I produced was

$$n(r,\theta) = n_0 \left\{ \exp[\lambda_0 \cdot (\frac{R_t}{r} - 1)] \right\} \times \exp\left[-\left[43 \sin\left[\left(\frac{\theta}{\Delta\theta} \right)^2 \right] \right] \right] \tag{1.1}$$

$$+ n_0 \left\{ 0.1 \exp\left[-\left(\frac{r - R_t}{H} \right) \right] \right\} \times \exp\left[-\left[200 \sin\left[\left(\frac{\theta}{\Delta\theta} \right)^2 \right] \right] \right]$$

The first term represents the density structure in the vicinity of and above the critical density region, whereas the second term represent the density structure substantially below the tumble density region and ensures the S/C flying through the model atmosphere on the final plunge would not fly through the atmosphere but be captured and destroyed. The coefficients adopted for the original model based on the first data sets were

$$n_0 = 1.8e10 \ cm^{-3};\ \lambda_0 = 310; R_t = 61700 \ km; H = 60 km;\ \Delta\theta = 1.05 \ radians \tag{1.2}$$

The UVIS stellar occultations were not analyzed in the chronological sequence of UVIS data acquisition due to the method that the UVIS team used to archive Saturn occultations. The atmosphere occultations were obtained as an add-on to ring occultations and they were labeled as ring occultations. Tommi Koskinen and I did not realize that the first analyzed occultations were heavily weighted by equinoctial ones and that later occultations showed a contraction of Saturn's equatorial thermosphere.

When 2014/2015 stellar occultation data became available, the contraction of Saturn's equatorial thermosphere was evident. Interestingly, the temperature profiles from December 2008 were generally hotter than the corresponding profiles from the spring of 2006 in the lower thermosphere (~ 0.1-10 nbar) while there were no detectable differences in the exospheric temperatures (cf. Fig. 4). The base of the thermosphere may also be at a higher pressure level in the December 2008 occultations. This supports the argument by Koskinen et al. (2015) that net warming (increased heating and/or decreased cooling) and extension of the thermosphere to deeper pressures can explain the expansion of the atmosphere and, by inference, that the contraction of the atmosphere that may have started after 2011 is accompanied by cooling of the lower thermosphere. The origin of these changes in thermal structure, however, is currently poorly understood.

The issue of timing for observations scheduled during Revs. 288-292 was raised as the coefficients in Eq. 1.2 were appropriate for equinoctial conditions and the Grand Finale orbits were predicted to experience reduced atmospheric drag on the S/C. Accordingly, a new set of coefficients was selected on the basis of best estimate for where solstitial densities would be in the summer of 2017 and are referred to as the revised model

$$n_0 = 1.26e10\ cm^{-3};\ \lambda_0 = 352.1; R_t = 61700\ km; H = 65\,km;\ \Delta\theta = 1.05\ radians \qquad (1.3)$$

I was also asked, based the contraction of Saturn's thermosphere from its expanded state during Saturn equinox, for my best guess at what the asymptotic lower bound density levels would be during Revs. 288-292 and 293, if the contraction continued at the then current rate. The lower bound model had the following coefficients

$$n_0 = 0.63e10\ cm^{-3};\ \lambda_0 = 352.1; R_t = 61700\ km; H = 65\,km;\ \Delta\theta = 1.05\ radians \qquad (1.4)$$

Note that the coefficients (n_0, λ_0) are normalized at R_t and the equator, a radial distance approximately between the predicted "1/2" tumble density and actual tumble density surfaces (Fig. 5, e.g. cf. Fig. 7). To help understand the latitudinal variation of model density surfaces, I plot in Fig. 5 the constant ½ tumble density surface in both the oblate spheroidal coordinate system in red and in the spherical coordinate system in blue. It is clear that the analytic model captures the equatorial structure of the oblate spheroidal shape of Saturn 1 bar surface and the 0.4 nbar surface in the thermosphere between ± 15° and especially the critical portion of the Revs. 288-292 trajectories, -10° S to 0°. It should be emphasized that the prediction model was developed to only be accurate at equatorial latitudes (± 15°) and as Fig. 5 shows it would become increasingly inaccurate at mid and high latitudes!

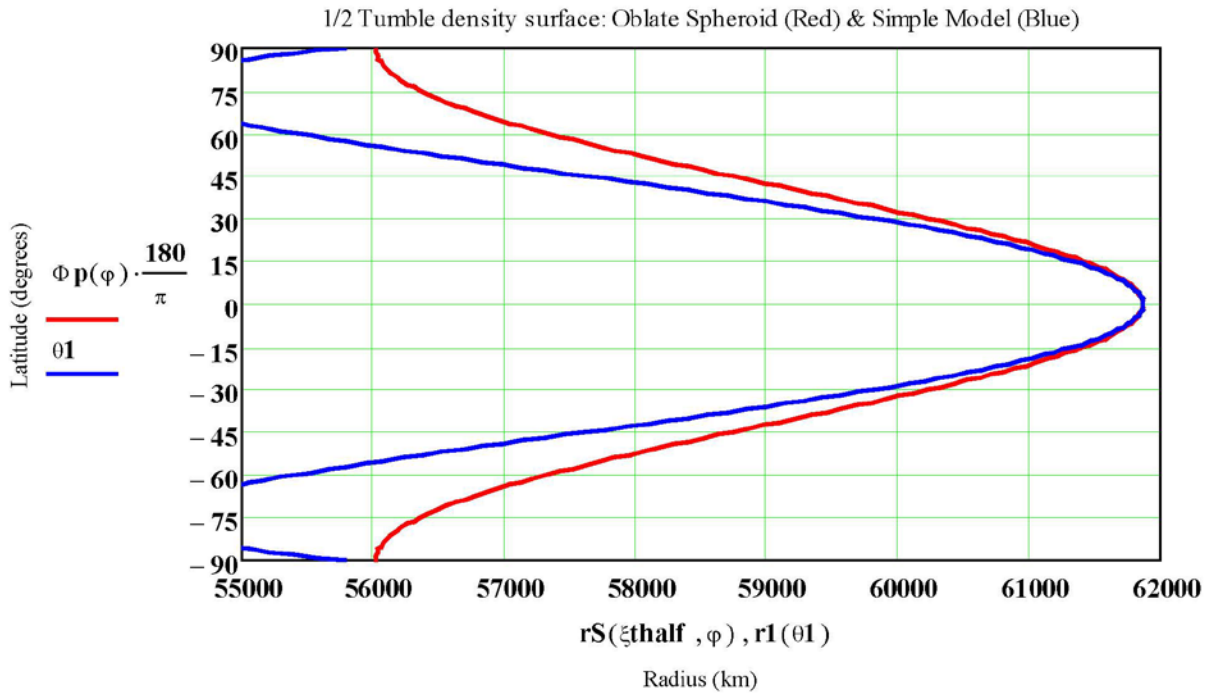

Figure 5. The constant ½ tumble density surface in the oblate spheroidal coordinate system (red) and the analytic model (blue), where the radius is measured in km from the center of Saturn and the latitude is planetocentric in degrees.

At the February 2017 PSG meeting the status of our knowledge of Saturn's thermospheric densities and the selection of the revised model coefficients (Eq. 1.3) is documented by the Excel file (Fig. 6), and the graph, (Fig. 7).

In the Fig. 6 Excel file, the critical occultations are the most recent ones ST42, ST66, ST67 highlighted in yellow and ST69 at time = 439 s, where the agreement ratio is tightly bounded by (0.87-1.04). Equinoctial occultations ST32, ST34, ST35, ST37 were not relevant as the thermosphere was expanded then and other occultations where the intersection occurred with mass densities significantly than lower than 10^{-11} kg m^{-3} were not relevant as the model was not developed and constrained by these low densities at high altitudes. An alternate presentation of the same conclusions is illustrated in Fig. 7 where the stellar occultations ST42, ST66, ST69 H_2 density profiles in the range of -6.2° S to -4.9° S and time frame of 2014-2017 show consistency at the highest density region of the trajectories for Revs. 288-292. The model density profiles yield, at the highest density portion on the predicted 27 August 2017 (Rev. 290) trajectory, a density ratio of model density divided by tumble density equal to 1.39/6.5 = 0.21, i. e., a factor of 5 density margin of safety. Note that the circled ST37 occultation in 2010 yielded a density at the intersection with Proximal Orbit 27 August 2017 that was almost equal to the ½ tumble density. This is also evident in Fig. 3, where a red dot intersects the magenta line.

Proximal orbit 27 August 2017				New Model		Occ	Stellar	Date	
Time (s)	Velocity (km/s)	radial distance (km)	trajectory angle (deg)	Mass density (kg/m^3)	Latitude (deg)	Mass density (kg/m^3)	Occ		Density ratio (occ to new model)
54	33.96	63384			6.044	exosphere	ST23/ST24	7/6/2008	
110	33.97	62992			4.350	exosphere	ST61	2/15/2016	
190	34.23	62263	4.675	1.67E-12	1.796	7.00E-13	ST30	12/16/2008	0.42
200	34.23	62236	4.528	1.97E-12	1.487	7.14E-13	ST46	2/18/2015	0.36
202	34.24	62230	4.52	2.04E-12	1.450	6.07E-13	ST62	2/15/2016	0.30
240	34.26	62134	3.94	3.58E-12	0.400	1.02E-12	ST64	3/6/2016	0.28
370	34.33	61903	2.02	1.18E-11	-3.212	1.32E-11	ST34	1/22/2009	1.12
375	34.33	61897	1.94	1.20E-11	-3.370	1.59E-11	ST32	1/3/2009	1.33
425	34.34	61850	1.2	1.37E-11	-4.797	2.38E-11	ST37	7/5/2010	1.74
439	34.345	61846	1.100	1.37E-11	-4.950	1.31E-11	ST69	3/28/2017	0.96
455	34.35	61832	0.755	1.24E-11	-5.591	2.17E-11	ST35	1/31/2009	1.75
465	34.35	61827	0.606	1.35E-11	-5.909	1.41E-11	ST42	10/3/2014	1.04
470	34.35	61826	0.531	1.34E-11	-6.010	1.28E-11	ST67	12/19/2016	0.96
475	34.35	61825	0.457	1.30E-11	-6.220	1.13E-11	ST66	12/4/2016	0.87
690	34.29	61972	-2.74	1.57E-12	-12.096	9.10E-13	ST41	5/21/2013	0.58
775	34.23	62143	-4.00	2.85E-13	-14.447	3.03E-13	ST36	6/12/2009	1.06
					-20.245	exosphere	ST33	1/22/2009	

Note $n(H_2)$ = 7.64 e9 cm^{-3} surface, i. e., "1/2" tumble density (= 2.525 e-11 kg/m^3) & the actual tumble density is = 6.5 e-11 kg/m^3 = 1.96 e10 H_2 cm^{-3} . Thus 6.5/2.525 = 2.6 = 0.95 scale height = 190 km of safety margin. 6.5/2.38 = 2.73 actual vs 6.5/1.37 = 4.7 model

Figure 6. Stellar occultations whose radial profiles intersected the predicted trajectory of Proximal Orbit 27 August 2017 below the exobase at the latitude of the occultation. The blue circled ST37 density is highest one and it occurred during the equinoctial season. The most relevant occultations for the Grand Finale orbits were ST42, 66, 67, 69. In the last column is the ratio of derived occultation density at the intersection of the predicted trajectory divided by the revised model density.

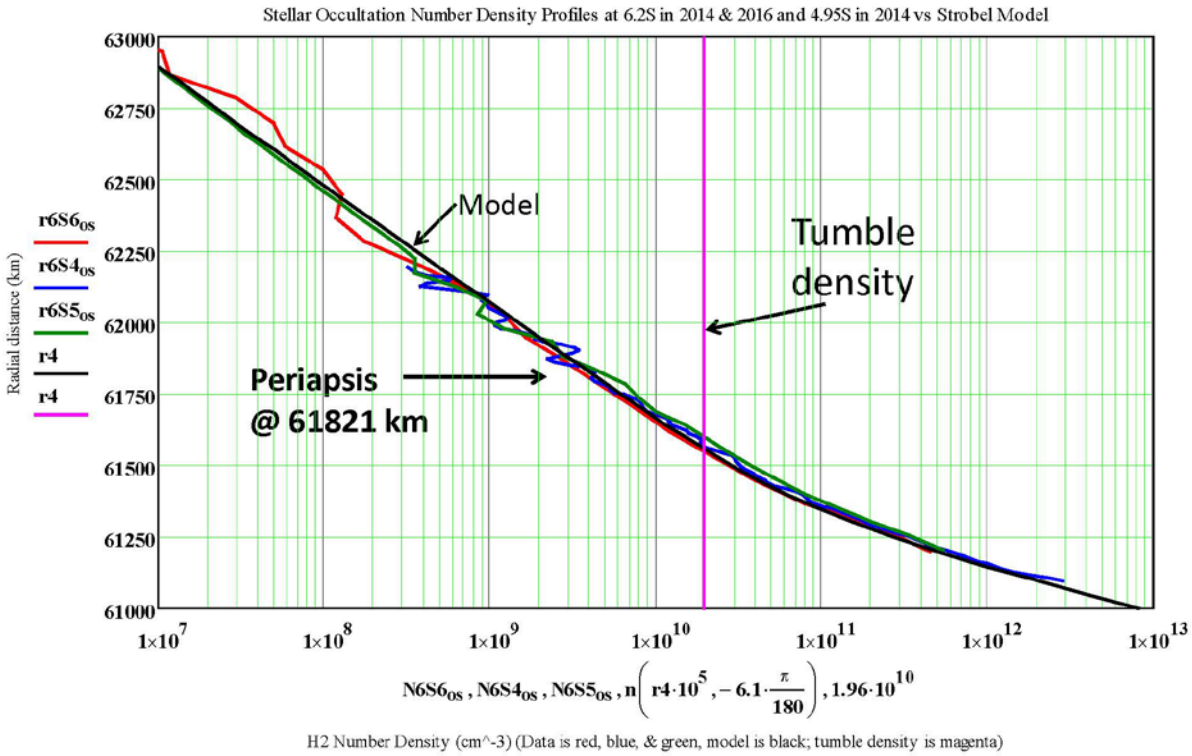

Stellar occultation ST66 2016 at -6.2 S (red); ST42 2014 at -6.0 S (blue); ST69 2017 at -4.95S. Black line is Strobel model; magenta line is tumble density. Maximum Density encountered on 27 Aug 2017 flyby is 1.39 x 10^{-11} kg m^{-3} = 4.19 x 10^{9} cm^{-3} at -5.3 S.

Figure 7. A comparison of stellar occultations ST66 2016 at -6.2° S (red); ST42 2014 at -6.0° S (blue); ST69 2017 at -4.95° S. Black line is the revised Strobel model; magenta line is tumble density. Maximum model density predicted for 27 Aug 2017 flyby is 1.39 x 10^{-11} kg m^{-3} = 4.19 x 10^{9} cm^{-3} at -5.3° S. Units are densities in H_2 molecules per cm^3 as a function of radial distance in km.

2. Analysis of the Grand Finale Orbits 288-293 Density Profiles in the Context of Model Predictions

The peak mass and equivalent H_2 number density results from the AACS inferred torques on the S/C for Revs 288-292, were in the range of (2.37-3.63) x 10^{-11} kg m^{-3}, as shown in the Excel file of Fig. 8. Note that the AACS derived densities are in agreement with the measured INMS densities over most of these orbits and that these peak densities are either equal to or exceed the defined "½" tumble density of 2.525 x 10^{-11} kg m^{-3} . The Revs occurred with a time cadence of approximately every 6 ½ days, and C/A occurred at East Longitudes -168°, -5°, +161°, -34°, and +130°, and local solar times 11:41, 11:37, 11:32, 11:28, 11:22, respectively, with 293 at 10:46 (cf. Fig. 12). Due to the oblate spheroidal shape of the equatorial thermosphere during C/A, there is a portion along the trajectory where the density reaches its maximum value but varies very little (< 3%) over 2° latitude. This can be visualized from Fig. 3. As a consequence it is possible to choose the common latitude of -5° S and a mean 1 bar radius of 60221 km for all five revs.

AACS Results for Revs. 288-292 where highest density is reached compared with Strobel model density										
			AACS	AACS				Model	Model	
Rev	SCET	Seconds ± peripasis	Density (kg/m**3)	H2 Number Density (cm-3)	Altitude (km)	Radius (km)	Latitude (deg)	H2 Number Density (cm-3)	Density (kg/m**3)	Actual/ Model Density ratio
288	2017-226T04:21:53.000	-70	2.69E-11	8.03E+09	1,705.68	61930.5	-4.848	2.58E+09	8.57E-12	3.14
289	2017-232T15:21:49.000	-71	3.41E-11	1.02E+10	1,652.36	61875.6	-4.914	3.50E+09	1.16E-11	2.93
290	2017-239T02:17:04.000	-66	3.62E-11	1.08E+10	1,626.61	61844.2	-5.151	4.08E+09	1.35E-11	2.67
291	2017-245T13:11:46.000	-74	3.63E-11	1.08E+10	1,638.85	61859.7	-5.018	3.79E+09	1.26E-11	2.88
292	2017-252T00:08:29.000	-76	2.37E-11	7.08E+09	1,674.92	61894.2	-5.08	3.09E+09	1.02E-11	2.31

Figure 8. A summary of the maximum mass and equivalent H_2 number density for Revs 288-292 as a function of radial distance and altitude at a common latitude of approximately -5° S. Note the decreasing trend in the density ratio with time given in the last column. Also, the highest densities during Revs. 288-291 exceeded the "½ tumble density" value.

Given common latitudes one can plot the H_2 peak number densities as a function of radial distances and extract scale heights for the thermospheric density structure at selected latitudes, as shown in Fig.9, if one has some knowledge of where the inferred density profiles from INMS measurements will merge with densities in lower thermosphere. To join the UVIS occultation density profiles would require that Saturn's thermosphere has higher temperatures than inferred from the occultations and from the INMS data (Yelle et al., 2018) as illustrated by two models with temperatures of 545 and 430 K in Fig. 9. The 545 K temperature corresponds to a scale height of 267 km and exceeds the typical ~ 400 K exospheric temperatures inferred from the recent UVIS stellar occultations over the past four years (cf. Fig. 4).

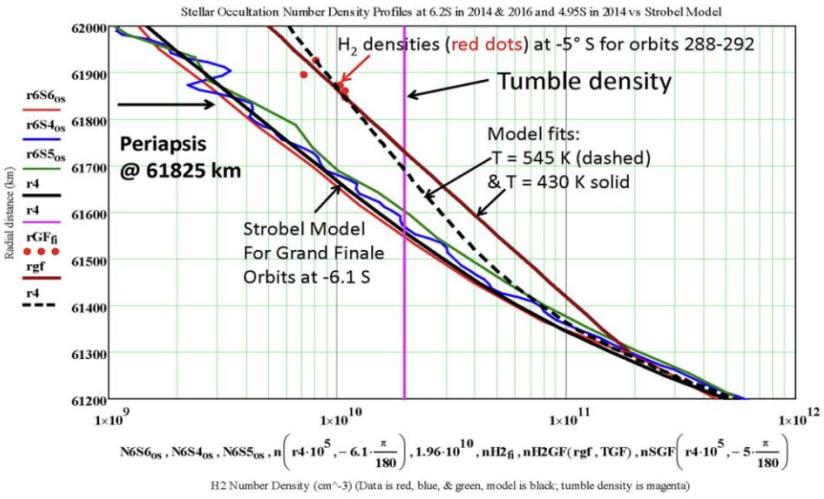

Figure 9. This is an updated Fig. 7 with the addition of the maximum AACS H_2 number density data points at -5° S and model fits with indicated isothermal temperatures. Units are densities in H_2 molecules per cm^3 as a function of radial distance in km.

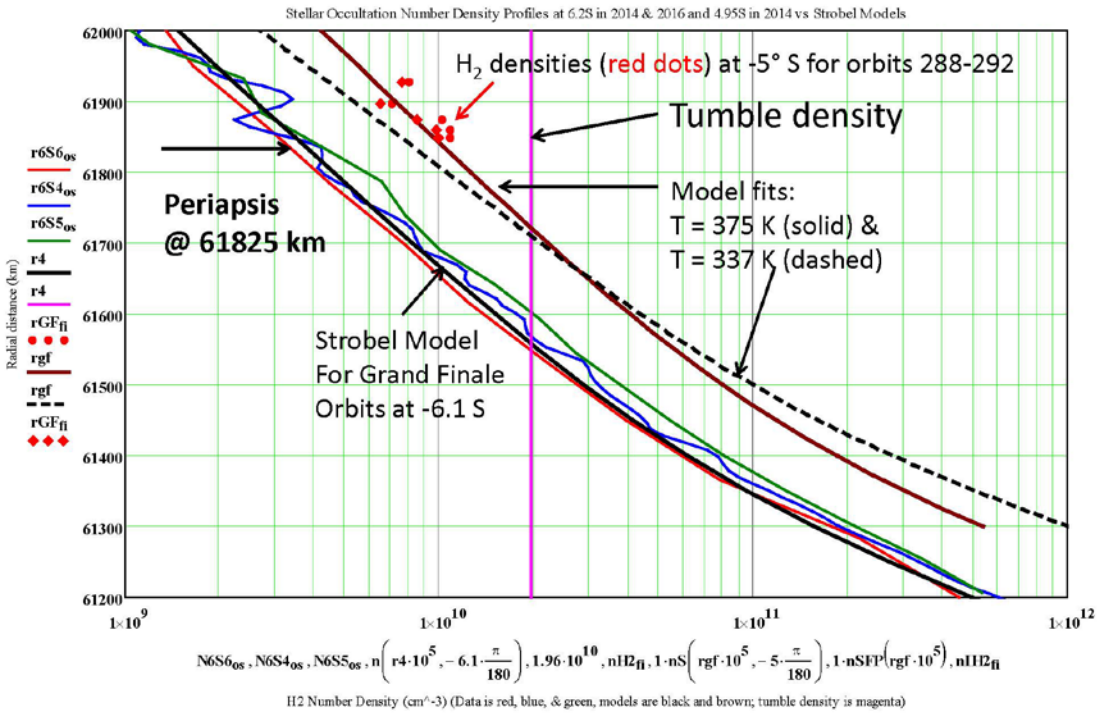

Figure 10. This is the same as Fig. 9, but with two new models with temperatures of 337 and 375 K which covers the range derived by Yelle et al. (2018) of 340-370 K. Note that r = 61200 km corresponds to an altitude of ~ 1000 km, where T ~ 240 K and p ~ 0.016 μbar. Units are densities in H_2 molecules per cm^3 as a function of radial distance in km.

Figure 10 illustrates the problem of joining the UVIS occultation density profiles with the colder temperatures derived from INMS measurements (Yelle et al., 2018). The base of the thermosphere is somewhere between 0.1 and 0.01 μbar with the latter corresponding to r = 61200 km in Fig. 10. At pressures greater than 3 μbar CIRS data has Saturn's stratospheric density, temperature, and pressure structure well constrained and thus the gap (0.01-3 μbar) is region where derived thermospheric densities must merge with the lower atmosphere.

An instructive approach is to analyze the INMS density profile for the S/C final plunge into Saturn's atmosphere which was very close to a radial trajectory with a latitudinal variation of only ~ 2° similar to most UVIS stellar occultations. To fit the final plunge data two coefficients in expression (1.1) had to be modified. The coefficient n_0 was slightly decreased from original model (1.2) and the λ parameter was increased from 310 to 420 which is equivalent to decreasing the isothermal temperature to 302 K from 410 K. The model comparison with Rev. 293 densities is shown in Fig. 11. This lower temperature in comparison to the higher exospheric temperatures ~ 400 K listed in Fig. 4 are actually close to what is inferred from the UVIS stellar occultations at lower radial distances ~ 61,500 km (cf. Fig. 13 of the Appendix: EUV STELLAR OCCULTATION DATA).

$$n_0 = 1.67\,e10\ cm^{-3};\ \lambda_0 = 420; R_t = 61700\ km; H = 65\,km;\ \Delta\theta = 1.05\ radians \qquad (1.5)$$

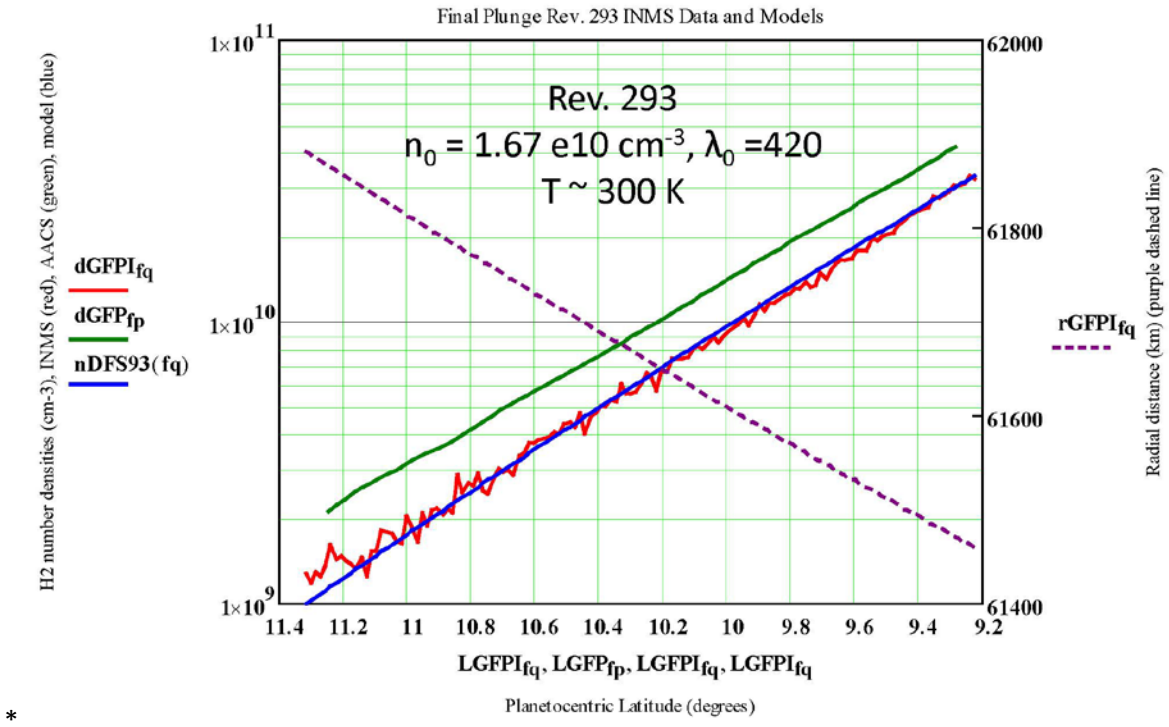

*

Figure 11. Cassini S/C final plunge (Rev. 293). AACS densities (green line, left y-axis) and INMS densities (red line, left y-axis) as a function of north latitude (x-axis). Radial distance (right y-axis, dash line) plotted as function of latitude (x axis). Model density profile (blue line, left y-axis) as a function of latitude (x-axis) with (1.1) and (1.5).

While the Strobel revised model based on UVIS stellar occultation data failed to accurately predict the INMS highest densities at the same latitudes in the southern hemisphere by an average factor of ~ 2.8, it would have predicted the Rev. 293 final plunge INMS densities to within ~ 90% at the highest altitudes decreasing to ~ 57% at the lowest altitudes, although the prediction model was not constructed to be valid below ~ 61,550 km. The inferred (assumed isothermal) temperature at 10° N from Rev. 293 densities was 302 K. Yelle et al. (2018) assumed a variable temperature profile with value of 300 K at the lowest data point and asymptotically approaching 351 K. They implicitly assumed a barotropic atmosphere, with parallel constant density, pressure, and temperature surfaces.

The Strobel revised model for the Grand Finale orbits had an equivalent temperature of 359 K. But inference of temperature from an assumed constant Jeans λ_0 parameter is not straightforward as the effective gravitational acceleration is a function of both radial distance and latitude, whereas Eq. (1.1) only includes the r^{-2} variation of gravity and not the radial derivative of the centrifugal potential. This implies that λ_0 is also a function of latitude as well as radial distance to the extent that g(r,θ) departs from r^{-2} behavior as it must in a rapidly rotating atmosphere. For the centrifugal potential, the rotation period of 10h 32m 5s was adopted to compute the radial derivatives $g_r(r,\theta)$ and the latitudinal

derivatives $g_\theta(r,\theta)$ of the total potential (centrifugal and gravitational) in spherical coordinates. Within ± 12° the equator, the ratio $g_\theta(r,\theta)/\, g_r(r,\theta)$ is at most 0.05 and of course zero at the equator.

As discussed in Sec. III.1 (or Appendix) UV Stellar and Solar Occultations, the anchor radial distance for derived density profiles is the half-light radii which for the C/A latitudes ~ -5° S for Revs. 288-292 is about 61,500 km. To account for the red dot densities ~ 10^{10} cm^{-3} at 61,850 km in Fig. 9 with a model anchored to densities ~ (3-4) x 10^{10} cm^{-3} at 61,500 km, one would require a thermospheric temperature ≥ 550 K. For lower temperatures, one would have to anchor the model density profiles to progressively lower radial distances on the stellar occultation density profiles as illustrated in Fig. 10 with temperatures of 337 K (black dashed line) and 375 K (brown line) and compare with temperatures of 545 K (black dashed line) and 430 K (brown line) in Fig. 9. The last stellar occultation (ST69, cf. Fig. 6 Excel file) occurred on 28 March 2017 less than 180 days before S/C entered Saturn's atmosphere for the last time.

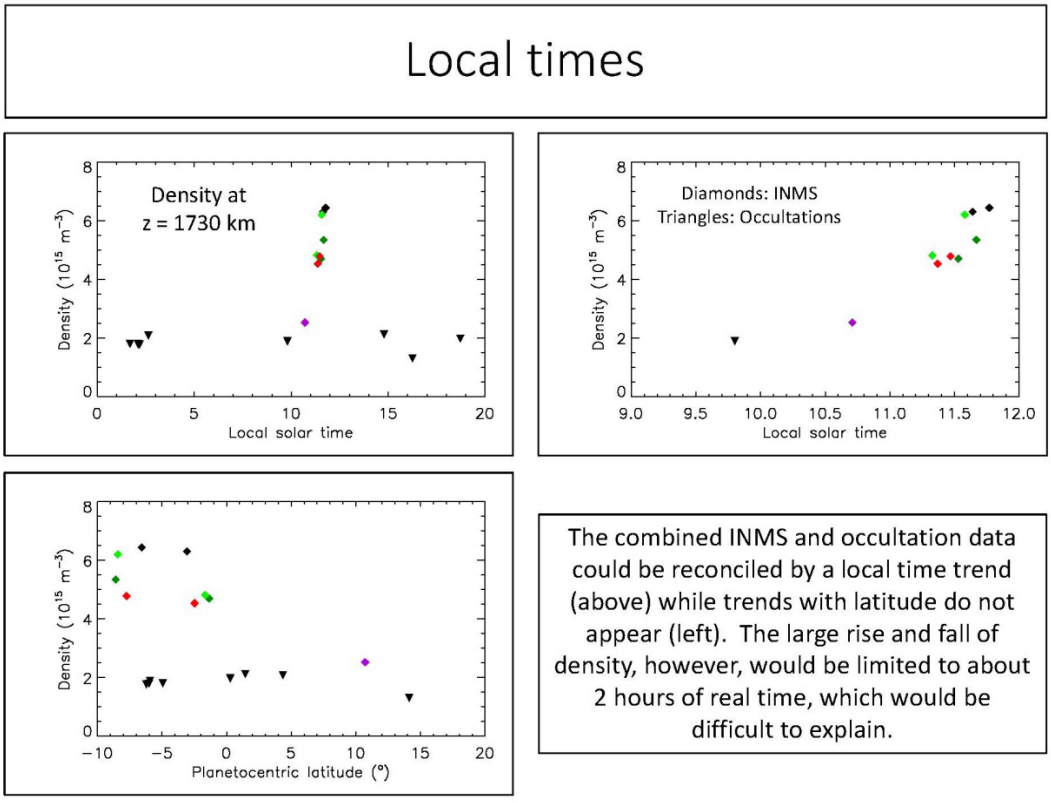

Figure 12. Stellar occultation (triangles) and INMS densities (diamonds) plotted as functions of local solar time and planetocentric latitude. (credit T. T. Koskinen)

We found density differences between non-invasive UVIS EUV stellar occultation measurements before the Grand Finale orbits and invasive, in situ density measurements made by the INMS, NAV and inferred from AACS in the southern hemisphere on Orbits 288-292 at latitudes of closest approach/ periapsis (~ -4°to -6°). It would appear to be beyond the reported error bars of all measurements. Thus we can

either attribute the density differences to time variability in Saturn's thermosphere driven in situ or from below as one might infer from Figs. 9 & 10 to connect would the stratosphere or to some important process(s) associated with hypersonic flight through the thermosphere that we omitted in our analysis. Time variability is a definite possibility, as illustrated by INMS data in Fig. 12, if it would be highly localized within a 2 hour window around local solar noon with an equivalent vertical upward parcel displacement of ~ 1.1 scale height (H ~ 150 km) = 165 km. As an example, invoking linear wave theory for a saturated hydrostatic, but not Boussinesq, gravity wave, a vertical displacement of 165 km would require for N ~ 0.004 s^{-1}, a net large $|c - u_0|$ horizontal speed > 800 m s^{-1}, and imply a vertical wavelength ~ 2000 km, if the relevant wave equation were solved by WKBJ short wavelength approximation. This is not valid for non-Boussinesq conditions. Even so, it seems implausible that density enhancements would just be restricted to local solar noon.

In summary, the Orbits 288-292 were selected to fly through the atmosphere at closest approach/ periapsis with factor of five margins in density. Based on the average of the measured densities, which were higher by a factor of 2.8, the actual margin was only about 1.8 putting the Cassini spacecraft squarely in the "Goldilocks zone" where attitude control authority was retained and the instruments were able to maximize their scientific return from Saturn's upper atmosphere.

VI. Engineering Team Contingency Strategies (Earl Maize, Erick Sturm, et al.)

The flight path design of Cassini's final five orbits required substantial conservatism with respect to the distance from Saturn's atmosphere during closest approach. The design goal was to find Saturn flyby altitudes that maintained the best balance between flight system safety and science return. If the spacecraft were to fly too deeply into atmosphere, the attitude control system would be overwhelmed by atmospheric torques; too high and the science instruments would not be able to effectively sample the atmosphere for analysis. The SAMWG models were used to establish and validate these limits. Margin had to be established in case the actual densities were either higher or lower than predicted.

The final trajectory design satisfied the objectives with significant allowable variation in Saturn's atmosphere. Nevertheless, the project chose to develop contingency plans to counter unexpected variations in Saturn's atmospheric density. These variations could result from large trajectory variations, un-modeled effects, or unknown unknowns.

The Proximal Orbit Atmospheric Transits Contingency Plan (JPL D-94787) provided a process for detecting and responding to an unacceptably denser-than-predicted Saturn atmosphere in the Proximal Orbits. The basic technique was to use the attitude control system's response to assess the atmosphere and then use the propulsion system to raise the spacecraft's periapsis altitude (a so-called pop-up maneuver). More details are available in the reference.

The project also developed the Proximal Orbit Pop-Down Scenario (JPL D-96898) that considered an atmosphere was surprisingly less dense. In this case, the anticipated science return from sampling

Saturn's atmosphere would have been significantly compromised. As in the contingency plan above, attitude control performance would be translated into density and if the density were deemed unacceptably low, the project could consider using the propulsion system to execute a pop-down maneuver to lower the flyby altitude. This was a "make-better" action that would have only been considered after careful discussion with the key project stakeholders. Again, more details are available in the reference.

Fortunately, neither option was required. With the baseline trajectory design, the Cassini spacecraft was squarely in the "Goldilocks zone" where attitude control authority was maintained and the instruments were able to effectively sample Saturn's upper atmosphere.

VII. References

Anderson, J. D., Schubert, G., 2007. Saturn's gravitational field, internal rotation, and interior structure. Science, 317, 1384–1387.

Haas, B. L., and Milos, F. S., 1995, Simulated rarefied entry of the Galileo Probe into the Jovian atmosphere, Journal of Spacecraft and Rockets, 32, No. 3,398-403, 1995

Hubbard, W. B., Porco, C. C., Hunten, D. M., Rieke, G. H., Rieke, M. J., McCarthy, D. W., Haemmerle, V., Haller, J., McLeod, B., Lebofsky, L. A., Marcialis, R., Holberg, J. B, 1997. Structure of Saturn's mesosphere from the 28 Sgr occultations. Icarus, 130, 404–425, doi:10.1006/icar.1997.5839.

Koskinen, T.T., B.R. Sandel, R.V. Yelle, F.J. Capalbo, G.M. Holsclaw, W.E. McClintock, S. Edgington, 2013. The density and temperature structure near the exobase of Saturn from Cassini UVIS solar occultations. Icarus, 226, 1318–1330, doi:10.1016/j.icarus.2013.07.037.

Koskinen, T.T., B.R. Sandel, R.V. Yelle, D. F. Strobel, I.C.F. Müller-Wodarg, J. Erwin, 2015. Saturn's variable thermosphere from Cassini/UVIS occultations, Icarus, doi:10.1016/j.icarus.2015.07.008.

Koskinen, T. T., et al., 2016. The detection of benzene in Saturn's upper atmosphere. Geophys. Res. Lett., 43, 7895{7901.

Koskinen, T. T., Guerlet, S., 2018. Atmospheric structure and helium abundance on Saturn from Cassini/UVIS and CIRS observations. Icarus, 307, 161{171.

Rault, D. F. G.. "Aerodynamics of the Shuttle Orbiter at high altitudes", Journal of Spacecraft and Rockets, Vol. 31, No. 6 (1994), pp. 944-952.

Smith, G. R., Shemansky, D. E., Holberg, J. B., Broadfoot, A. L., Sandel, B. R., 1983. Saturn's upper atmosphere from the Voyager 2 EUV solar and stellar occultations. J. Geophys. Res., 88, 8667 – 8678, doi:10.1029/JA088iA11p08667.

Vervack, R. J. Jr., Moses, J. I., 2015. Saturn's upper atmosphere during the Voyager era: Reanalysis and modeling of the UVS occultations. Icarus, 258,135–163, doi: 10.1016/j.icarus.2015.06.007.

Yelle, R. V., Serigano, J., Koskinen, T. T. , et al., 2018. Thermal Structure and Composition of Saturn's Upper Atmosphere from Cassini/INMS Measurements, Geophys. Res. Lett., submitted.

VIII. Appendix:

1. EUV Stellar and Solar Occultations Data (T. T. Koskinen et al.)
2. Proximal Atmospheric Transits Contingency Plan JPL D-94787
3. Proximal Orbit Pop-Down Scenario JPL D-96898

APPENDIX: EUV STELLAR OCCULTATION DATA

T. T. KOSKINEN ET AL.

1. Introduction

The density and temperature in Saturn's thermosphere were monitored regularly from 2005 to 2017 by UV solar and stellar occultations observed by the Cassini/UVIS instrument (Shemansky and Liu, 2012; Koskinen et al., 2013, 2015, 2016; Koskinen and Guerlet, 2018). In particular, stellar occultations near the equator were used to construct the engineering atmosphere model that was used in planning the Grand Finale orbits and final plunge. The purpose of this appendix is to provide an overview of the stellar occultation data analysis procedure that summarizes and expands on the information already available (Koskinen et al., 2015). This report focuses on the retrieval of H_2 densities and temperatures from stellar occultations in the EUV channel of the UVIS instrument that were relevant to the engineering model. A list of the relevant occultations is given in Table 1. Section 3 includes a brief discussion of trends based on the occultations denoted by the asterisk that primarily guided our expectations of the state of the atmosphere during the last orbits of the mission in the summer/fall of 2017. In general, results from occultations through the end of 2015 have been published (Koskinen et al., 2015; Koskinen and Guerlet, 2018). At the time of writing, results for occultations from 2016–2017 are unpublished.

Table 1. Stellar occultation locations

ID	PDS label	Date	Star	LST	$\phi_{\rm pc}$ (°)
ST23	EUV2008_188_23_30	07/06/2008	β Cen	07:50	6.3N
ST24	EUV2008_203_01_17	07/21/2008	β Cen	07:48	6.3N
ST30	EUV2008_351_19_08	12/16/2008	α Cru	19:00	1.7N
ST32	EUV2009_003_04_20	01/03/2009	β Cru	18:31	3.5S
ST33	EUV2009_022_04_39	01/22/2009	β Cru	13:51	20S
ST34	EUV2009_022_08_00	01/22/2009	β Cru	18:30	3.4S
ST35	EUV2009_031_22_00	01/31/2009	β Cen	09:41	5.6S
ST37	EUV2010_186_11_07	07/05/2010	α Vir	07:10	4.9S
ST41*	EUV2013_141_05_36	05/21/2013	θ Car	03:58	12S
ST42*	EUV2014_276_06_17	10/03/2014	ζ Pup	09:47	6.1S
ST46*	EUV2015_049_21_10	02/18/2015	κ Ori	19:54	1.7N
ST61*	EUV2016_045_02_15	02/14/2016	α Vir	02:38	4.4N
ST62*	EUV2016_045_08_50	02/14/2016	α Vir	08:50	1.5N
ST64*	EUV2016_094_18_01	04/03/2016	γ Ori	18:43	0.5N
ST65*	EUV2016_296_06_40	10/22/2016	ζ Cen	16:18	14N
ST66*	EUV2016_339_04_47	12/04/2016	β Cru	02:11	6.2S
ST67*	EUV2016_353_13_13	12/18/2016	β Cru	02:07	6.0S
ST69*	EUV2017_087_21_53	03/28/2017	β Cru	01:41	5.0S

2. Data analysis

2.1. **Basic principle.** In general, a stellar occultation consists of a time series of uncalibrated spectra $S(\lambda_b, t)$ of the star in wavelength bands λ_b where the exposures t correspond to line of sight (LOS) tangent altitudes $a_z(t)$ i.e., the shortest distance from

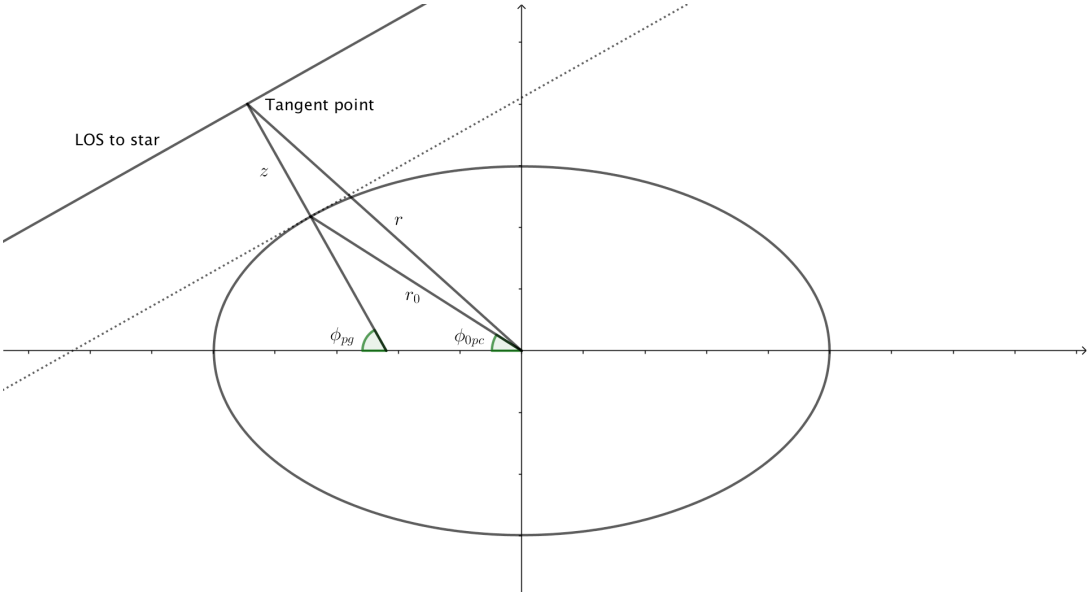

FIGURE 1. Illustration of occultation geometry. Saturn geometry is not to scale and oblateness is significantly enhanced for ease of viewing.

the LOS to the 1 bar level surface of the planet, measured along the local surface normal (see Figure 1). The spectra at sufficiently high tangent altitudes for the starlight to be unattenuated are averaged to derive a reference spectrum $S_0(\lambda_b)$. All spectra are divided by the reference spectrum to obtain a time series of atmospheric transmission spectra $T(\lambda_b, t)$, which are fitted to retrieve LOS column density profiles $N_s(a_z)$ for different species s. The column density profile of each species is inverted to obtain a number density profile $n_s(z)$ at altitudes z above the 1 bar level. The number density profile of the major species H_2 can be used to retrieve a temperature-pressure (T-P) profile under the assumption of hydrostatic equilibrium. If the pointing is stable during the occultation, the star remains at the same location on the detector and there is no need to calibrate the data to calculate transmission. Stable occultation experiments are essentially self-calibrating and highly repeatable. Most of the Cassini Saturn occultations are stable. Evidence for small pointing drifts have been found in only a few occultations that have been excluded from published analyses.

2.2. **UVIS occultation data.** The wavelength range of the EUV channel is 563–1182 Å with a point source resolution of about 2.8 Å and a pixel spacing of about 0.6 Å. The detector consists of an array of 1024 x 64 spectral and spatial pixels known as bands and lines, respectively. More information about the UVIS instrument can be found in Esposito et al. (2004) and in the UVIS User Guide available through the Planetary Data System (PDS) Planetary Rings Node. The occultation data are available through the PDS Atmospheres Node. Because interstellar hydrogen absorbs starlight at wavelengths shorter than 911 Å (the ionization threshold of H), the spectra of UV-bright stars (Table 1) are observed only at wavelengths longer than this limit. For example, Figure 2 shows the image of ζ Puppis (occultation ST42 in Table 1). The image is concentrated in detector line 28 (counting from 0), with only residual counts in surrounding lines, as expected based on the UVIS point spread function (PSF, McClintock et al., 1993).

In order to extract spectra from the stellar images, we sum the signal over spatial lines in each wavelength band. We smooth each spectrum by applying a 1-4-6-4-1 filter to reduce fixed pattern noise across wavelength bands. If required, we use the dark

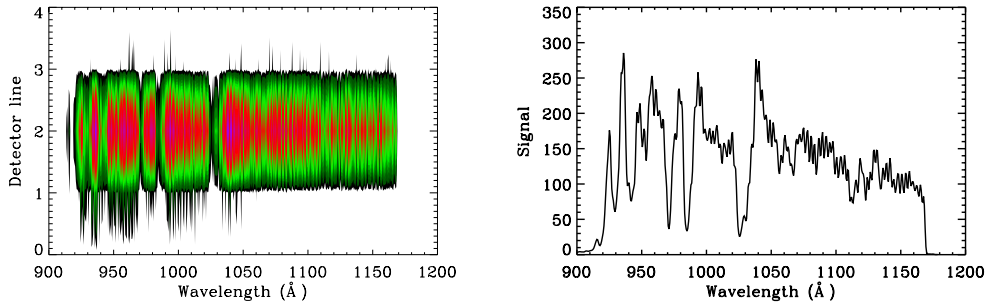

FIGURE 2. **Left**: Color contour illustrating the detector image of ζ Puppis (ST42 in Table 1) at the tangent altitude of 4804 km above the 1 bar level at ϕ_{pc} = -5.16°. White background indicates no signal. Lines 0-4 in the image correspond to lines 26–30 on the UVIS detector. **Right**: Reference spectrum obtained by summing the signal over spatial lines and averaging at tangent altitudes of 4000–4800 km.

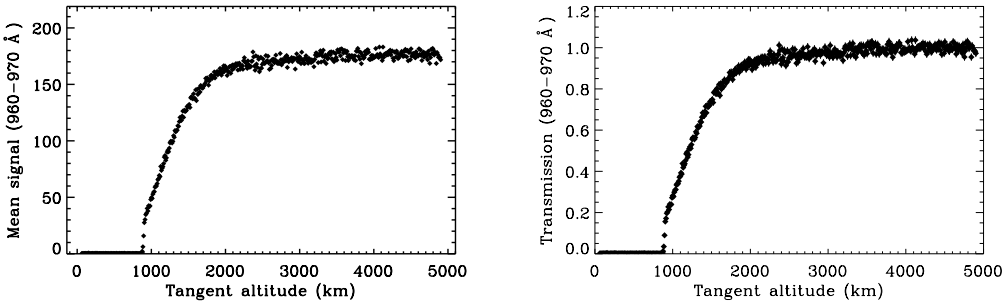

FIGURE 3. Mean signal (left) and transmission (right) at 960–970 Å for occultation ST42. The background signal (below 900 km) is negligible.

region at the lowest tangent altitudes (see Figure 3) to obtain the background signal and deduct the average background from the spectra. Occultation exposures are short, only a few seconds, and most of the known background sources are much weaker than the stars. Therefore, the background is either negligible or very weak. We inspect the signal in different wavelength bands and identify the tangent altitudes where the signal is constant with altitude to calculate the reference spectrum (Figure 2). Finally, we calculate the transmission time series (light curves) by dividing all the spectra by the reference spectrum. The transmission time series is the simplest measure of absorption by the atmosphere, obtained with minimum processing, and comparing the light curves from different observations provides stringent constraints on the variability of the atmosphere (see Section 3).

2.3. **Altitudes on Saturn.** Saturn is the most oblate of the giant planets in the solar system and this leads to a number of complications for the geometry of the occultation data. The observed shape of the planet at the 1 bar and 100 mbar levels can be approximated by a surface of constant gravitational potential as described by Anderson and Schubert (2007) (hereafter, the AS model). The planetary rotation rate adopted by this model minimizes the zonal wind-driven perturbations to the shape of the pressure levels and reproduces the observed shape to within 15 km. The occultation geometry calculations, however, rely on the routines from the NASA Navigation and Ancillary Information

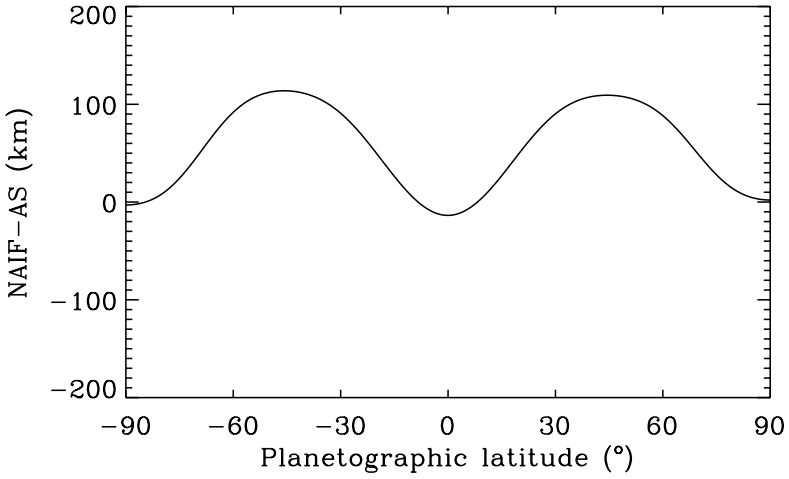

FIGURE 4. The difference of the NAIF ellipsoid from the AS model.

Facility (NAIF), which assume that the 1 bar level is a simple ellipsoid of revolution with the radius given by:

$$R(\phi_{pc}) = \frac{R_S R_{pol}}{\sqrt{R_{pol}^2 \sin^2\theta + R_S^2 \cos^2\theta}} \quad (1)$$

where the polar and equatorial radii are $R_{pol} = 54{,}364$ km and $R_S = 60{,}268$ km, respectively, and $\theta = \pi - \phi_{pc}$. This ellipsoid differs from the observed shape (see Figure 4) and the tangent altitudes obtained from standard geometry must be corrected to reflect this. Details of this correction and the geometry calculations are provided below.

We use routines from NAIF to calculate the occultation geometry. We obtain the stellar RA and DEC coordinates from the Hipparcos catalogue for each target and use the given proper motion to adjust them from the J1991.25 epoch to the time of the observations. We then obtain the LOS vector that points from the spacecraft to the stellar coordinates in the IAU Saturn coordinate system. This calculation is not affected by the UVIS pointing uncertainty - it depends only on the known position of the spacecraft and stellar coordinates. The NAIF nearpoint routine calculates the tangent altitude i.e., shortest distance between the LOS vector and the assumed 1 bar level on Saturn. The tangent altitude vector is perpendicular to the NAIF ellipsoid at a given latitude. Note that planetographic latitude ϕ_{pg} is constant along the altitude vector while planetocentric latitude ϕ_{pc} varies along this vector (see Figure 1).

We use the law of cosines to calculate the radial distance from Saturn's center to each tangent point i.e., the intersection of the LOS with the local vertical:

$$r(\phi_{pg}) = \sqrt{r_0(\phi_{pg})^2 + z^2 - 2r_0(\phi_{pg}) z \cos(\pi - |\phi_{pg} - \phi_{0pc}|)}. \quad (2)$$

where the geometry and the meaning of the variables are illustrated by Figure 1. We note that the radial distance to the tangent point r differs from the shortest distance to the LOS from Saturn's center unless the LOS lies in the equatorial plane. The highest atmospheric density along the LOS is expected to occur at the tangent point.

The deviation of the AS model from the NAIF ellipsoid is about 100 km at mid-latitudes, compared with the equatorial radius of 60,268 km (see Figure 4). Thus the altitudes based on the two models can differ by up to 100 km but the direction of the

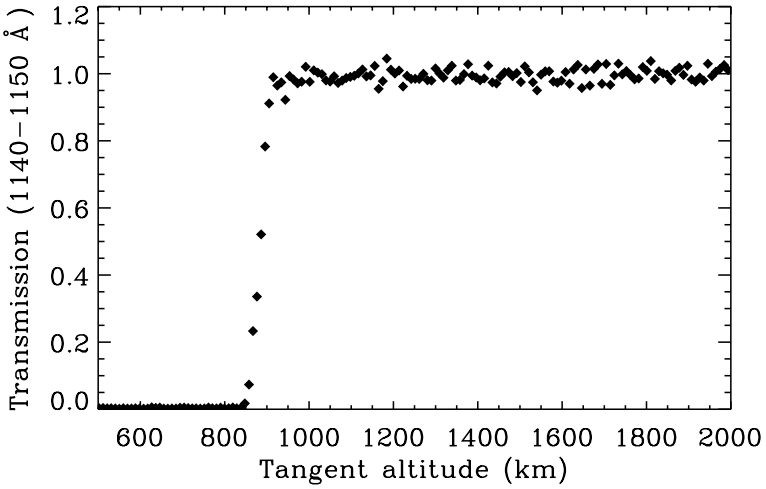

FIGURE 5. Transmission at 1140–1150 Å where absorption is dominated by CH_4.

local vertical and the point of highest density along the LOS in the AS model are indistinguishable from the NAIF ellipsoid. In order to calculate the revised tangent altitudes, we therefore integrate the differential equations of the local vertical (Lindal et al., 1985)

$$\mathrm{d}\phi_{pc} = \frac{1}{r}\tan\psi \mathrm{d}r \tag{3}$$

$$\mathrm{d}z = \frac{\mathrm{d}r}{\cos\psi}. \tag{4}$$

numerically with a 1 km altitude step down from $r(\phi_{pg})$ to the 1 bar level in the AS model. The angle

$$\psi = \arctan\left(\frac{g_\phi}{g_r}\right) = \phi_{pg} - \phi_{pc} \tag{5}$$

where g_ϕ and g_r are the meridional and radial components of gravitational acceleration, respectively.

2.4. **Fits to transmission spectra.** We fit transmission spectra to retrieve LOS column densities for H_2. The retrieval relies on the high resolution absorption cross section of H_2 in the Lyman and Werner electronic bands at 910–1120 Å, which depends on temperature. For this reason, the retrieval of temperature and density is iterative (see Section 2.7). In this section, however, we focus on the retrieval of column densities from LOS spectra, and illustrate it with a few simple examples for the ST42 occultation.

In general, we fit the transmission spectra at wavelengths of 925–1085 Å. Absorption in this wavelength region is dominated by the electronic bands of H_2 but CH_4 and C_2H_6 also provide continuum absorption near the homopause at the lowest tangent altitudes in the thermosphere. The hydrocarbon absorption is clearly detectable at $\lambda > 1120$ Å. Distinguishing absorption by H_2, CH_4 and C_2H_6 based on a narrow wavelength window near the edge of the EUV detector is difficult. For this reason, we decided to exclude tangent altitudes where hydrocarbon absorption is significant and fit the data with H_2 only. We use the light curve at 1140–1150 Å where absorption is dominated by CH_4 to identify tangent altitudes that are excluded from the fit (see Figure 5). This determines the lowest tangent altitude in our H_2 column density retrieval i.e., 900 km for ST42.

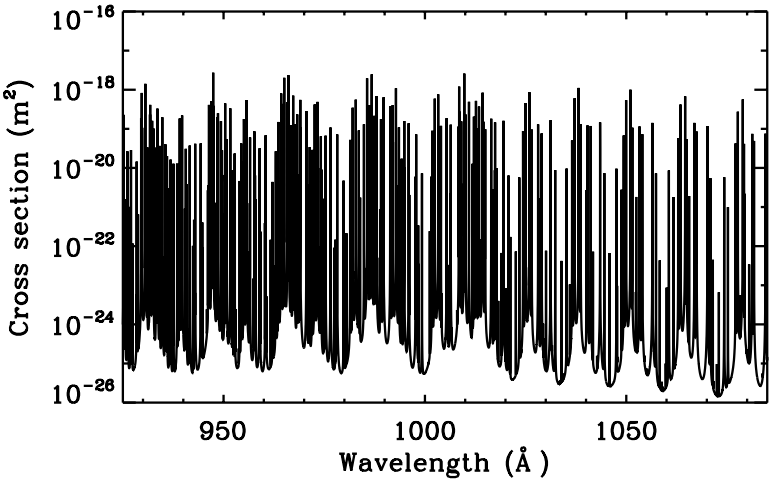

FIGURE 6. Cross section of H_2 calculated at $T = 340$ K and a resolution of 0.001 Å.

We use the Levenberg-Marquardt (L-M) iteration (Press et al., 1992) to fit the transmission spectra. The forward model is

$$T(\lambda_b, a_z) = \int R(\lambda_b, \lambda) \exp\left[-\sigma_{av}(\lambda, a_z) N(a_z)\right] \mathrm{d}\lambda \tag{6}$$

where σ_{av} is the column-averaged cross section:

$$\sigma_{av}(\lambda, a_z) = \frac{1}{N(a_z)} \int_{a_z} \sigma(\lambda, l) n(l) \mathrm{d}l \tag{7}$$

and the integral is along the LOS with tangent altitude a_z. We calculate the cross section at a resolution of 0.001 Å for different temperatures by using detailed line lists (e.g., Abgrall et al., 1993a,b, 2000). The average cross section accounts for changes in temperature along the LOS. We note that it is not an approximation if the temperature profile is known and the atmosphere is roughly horizontally uniform. $R(\lambda_b, \lambda)$ is the UVIS line spread function that includes a Gaussian core and extended wings to account for internal scattering (see the UVIS User Guide). We note that the forward model does not account for structure in the stellar spectrum. We have tested the retrieval by constructing a forward model that incorporates the stellar spectrum but found that this additional complexity did not yield significantly different column densities.

In the remainder of this section, we illustrate the dependency of the forward model on temperature and column density by using cross sections calculated with a single temperature to fit the ST42 data. For example, Figure 6 shows the high resolution cross section for a temperature of 340 K. Figure 7 shows the best fit to the observed absorption spectrum at the tangent altitude of 1608 km based on this cross section. The quality of the fit is good ($\chi^2_\nu = 1.3$) and the LOS column density is 3.5×10^{22} m^{-2}. If we calculate the cross sections at temperatures of 150 K and 450 K instead, the derived column densities are 6×10^{22} m^{-2} ($\chi^2_\nu = 2.1$) and 2.7×10^{22} m^{-2} ($\chi^2_\nu = 1.3$), respectively. Thus a change of 300 K in the cross section temperature changes the retrieved column density by a factor of 2. The quality of the fit is not particularly sensitive to the cross section temperature, preventing us from constraining the temperature based on the observed absorption lines alone. Figure 7 also compares the data at 1608 km with a forward model based on the column density of 1.05×10^{23} m^{-2} i.e., three times higher than the best fit value, with

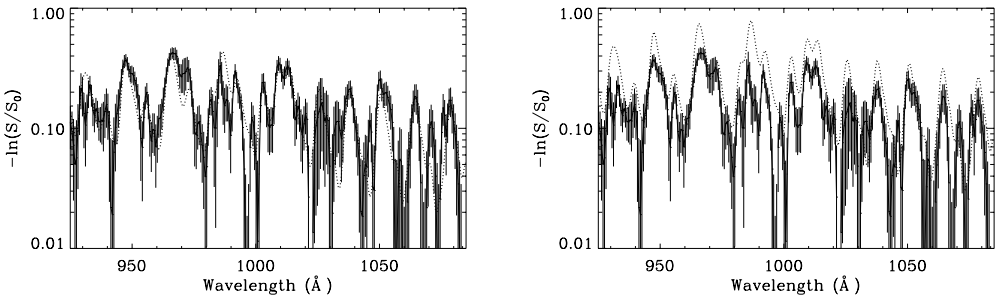

FIGURE 7. **Left**: Observed optical depth fitted with our best fit forward model (dotted line) with H_2 column density of 3.5×10^{22} m^{-2} and $\chi^2_\nu = 1.3$ obtained with the cross section calculated for a temperature of 340 K. **Right**: A poor fit ($\chi^2_\nu = 6.1$) with a column density of 1.05×10^{23} m^{-2} i.e., three times higher than the best fit.

the cross section at 340 K. This results in a very poor fit ($\chi^2_\nu = 6.1$). *We conclude that, at minimum, we measure the column density to better than a factor of 2 at 1608 km.*

2.5. **Line of sight integral.** In this section we relate the column density profile to the local number density profile. Measuring one column density provides no constraint on the underlying number density profile. Measuring the column density profile at different tangent altitudes, however, places relatively strong constraints on the number density profile, provided that the atmosphere is horizontally uniform on length scales that dominate the LOS integral. In preparation for the theory in this section, we define some general properties of occultation geometry. The intersection of the plane that includes the LOS and the local surface normal with a planet and its atmosphere is a known as a normal section. The normal section of a spherical planet and its atmosphere is a circle and we define this normal section so that the LOS is tangent to this circle (imagine Figure 1 for spherical geometry). We assume that the density levels above the tangent altitude form concentric circles with the normal section. In this geometry, the LOS column density is:

$$N(a_z) = 2\int_{a_z}^{\infty} \frac{n(r) r \mathrm{d}r}{\sqrt{r^2 - r_z^2}} \tag{8}$$

where $r_z = R_p + a_z$ is the tangent radius. We discretize the column density integral for tangent altitude a_{zi} as

$$N_i = \sum_{j \geq i}^{L} M_{ij} n_j \tag{9}$$

where L is the number of altitude layers in the grid and

$$\begin{aligned} M_{ij} &= 2\sqrt{r_{j+1/2}^2 - r_i^2} \text{ for } j = i \\ M_{ij} &= 2\left(\sqrt{r_{j+1/2}^2 - r_i^2} - \sqrt{r_{j-1/2}^2 - r_i^2}\right) \text{ for } i < j < L \\ M_{ij} &= 2\left(\sqrt{r_{j+1/2}^2 - r_i^2} - \sqrt{r_{j-1/2}^2 - r_i^2}\right) \\ &+ 2\int_{r_{j+1/2}}^{\infty} \exp\left[\left(\frac{1}{n}\frac{\partial n}{\partial r}\right)\left(r' - r_{j+1/2}\right)\right] \frac{n(r) r' \mathrm{d}r'}{\sqrt{r'^2 - r_i^2}} \text{ for } j = L. \end{aligned} \tag{10}$$

In order to calculate N_i, we use a radius grid that coincides with the tangent radii derived for the occultation exposures.

We adapt the above formulae to oblate geometry by using a technique based on osculating circles. In order to do so, we need to define a few more properties of the geometry. The NAIF ellipsoid, given by equation (1), is a simple Clairaut spheroid i.e., limited to zonal harmonic J_2. The normal section of a Clairaut spheroid is an ellipse with standard eccentricity e. The radius of curvature for a normal section with an azimuth α with respect to local north is given by (Deakin and Hunten, 2013):

$$\rho_\alpha = \frac{\rho\nu}{\rho \sin^2\alpha + \nu\cos^2\alpha} \tag{11}$$

where ρ and ν are the radii of curvature of the meridian normal section and the prime vertical normal section, respectively. These are given by:

$$\nu = \frac{r_{\rm eq}}{W} \tag{12}$$

$$\rho = \frac{r_{\rm eq}(1-e^2)}{W^3} \tag{13}$$

$$W = 1 - e^2\sin^2\phi_{\rm pg} \tag{14}$$

where $r_{\rm eq}$ is the equatorial radius of the normal section, given by

$$r_{\rm eq} = \frac{r(\phi_{pc})}{1 - f\sin^2\phi_{pc}} \tag{15}$$

where f is the flattening of the normal section.

We treat Saturn as a Clairaut spheroid and assume that the normal section corresponding to each LOS is an osculating circle with a radius equal to the local radius of curvature of the actual normal section ellipse at the tangent point. As we demonstrate below, these assumptions should not lead to a significant error in our integrals. We map the density levels above the tangent point to circles concentric with the osculating circle. In equation (9), this means that the tangent radius is

$$r_i = c_i\left[r_s(\phi_{pc}) + a_z\right] \tag{16}$$

where c_i is the 'curvature factor' based on equation (11) and r_s is the effective surface radius. The mapping must preserve the altitude spacing of the occultation grid or otherwise it will modify the density gradient. Thus the curvature factor c_j at altitudes $j > i$ higher than $z_i = a_z$ is

$$c_j z_j - c_i z_i = z_j - z_i \rightarrow c_j = 1 + \frac{z_i}{z_j}\left(c_i - 1\right) \tag{17}$$

This means that

$$r_j = c_i r_s(\phi_{pc}) + c_j z_j \text{ where } j > i \tag{18}$$

for concentric osculating circles.

The theory outlined above is complex. In fact, it is to some degree too complex for the problem at hand. The modifications due to oblate geometry do not produce large differences in LOS integrals from spherical geometry or even simple isothermal path length estimates. Let us consider an example based on the 'bog standard' line integral:

$$N(a_z) = n(a_z)P \approx n(a_z)\sqrt{2\pi r_z H} \tag{19}$$

where H is the pressure scale height in an isothermal atmosphere. The simple path length integral for ST42 at 1608 km is $P \approx 8035$ km ($H = 166$ km, $r_z = 61806$ km). Our final column density for this tangent altitude is 3.2×10^{22}, implying a number density

of 4×10^{15} m^{-3}. Our final number density, based on the full inversion and path length integral, agrees with this value to within 2%. The reason for such a good agreement with the simple formula above is twofold. First, the half-light latitude of ST42 is $\phi_{pg} = 7.4°$S and the oblateness correction is minimum at the equator, rising to about 6% at mid-latitude and about 10% at the poles (Koskinen et al., 2013). Second, the contribution function of the LOS integral is sharply peaked around the tangent point, so that H applies along the effective path. *We conclude that the inversion does not contribute significantly to the uncertainty in the retrieved number densities and, at minimum, we measure the number densities to better than a factor of 2 at 1608 km.*

The path length integral provides guidance on the horizontal resolution of the occultation data. An effective path length of 8000 km corresponds to 7.4° in latitude/longitude. A careful exploration of the occultation LOS at $a_z = 1608$ km for ST42 reveals that, due to the orientation of the LOS, the planetocentric latitude changes from about 3.5°S to about 8.3°S over 8000 km around the tangent point. This is a measure of the horizontal resolution of the number density retrieved from the ST42 occultation at 1608 km because the inversion effectively assumes horizontal uniformity along the integration path. This result has interesting consequences for waves in Saturn's thermosphere. We detect evidence for waves in several occultations, with a vertical wavelength of the order of a scale height. The impact of these waves on the heating and circulation of the thermosphere also depends on their horizontal wavelength. To be detectable in the occultation data, the waves must have horizontal wavelengths in excess of 8000 km.

2.6. **Forward model temperature fit.** We use the L-M iteration to fit the observed density profiles with a parameterized temperature profile for our final results and in order to recalculate absorption cross sections during the iterative retrieval of temperature and density (see Section 2.7). The parameterized temperature profile has the form (Yelle et al., 1996):

$$T(z) = T_0 + \frac{T_\infty - T_0}{1 + \exp\left[-\alpha(z - z_m)\right]} \tag{20}$$

where T_0, α, and z_m are treated as free parameters. T_∞ is the exospheric temperature that we fit to the data above 1800 km, assuming an isothermal atmosphere. The number density profile based on this profile is

$$n(z) = n(z_0)\frac{T(z_0)}{T(z)} \exp\left[-\int_{z_0}^{z} \frac{kT(z')\mathrm{d}z'}{2m_H g_z(z')}\right] \tag{21}$$

where $g_z = \sqrt{g_\phi^2 + g_r^2}$, m_H is the mass of hydrogen and $n(z_0)$ is treated as a free parameter. We integrate this equation numerically with an altitude spacing of 1 km along the local vertical. We then calculate the LOS column densities based on the resulting number density profile by using equation (9).

2.7. **Iterative retrieval of density and temperature.** We start the iteration by calculating the H_2 cross section with a temperature of 300 K and retrieve the first column density profile. Our standard iteration procedure fits the parameterized temperature profile directly to the column density profile in order avoid any additional error from the inversion. We have recently noted that the fit to the column densities does not always converge well, leading to deviations from the direct temperature retrieval (see Section 2.9). In cases where deviations are observed, we invert the column density profile (see Section 2.8) and fit number densities with a parameterized model instead. This leads to a model temperature profile that always agrees well with direct retrieval. Having derived

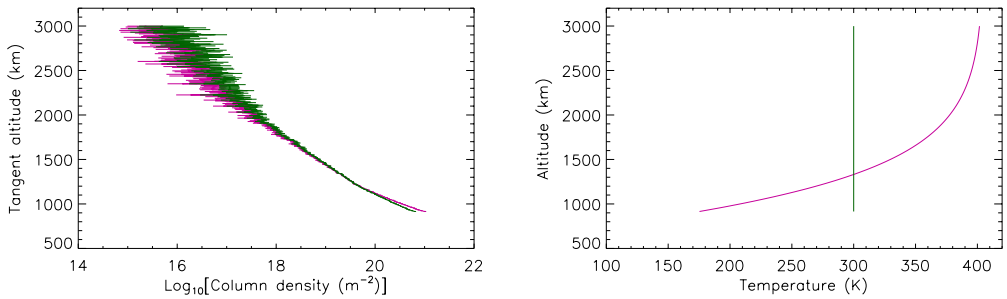

FIGURE 8. **Left**: Column density profiles for ST42 from the first iteration step (green) and after convergence (purple). See Section 2.7 for the details of the iterative retrieval. **Right**: Temperature profiles that were used to calculate the H_2 cross section for the first and last iteration. The purple profile is identical to the final forward model temperature profile for ST42.

the forward model temperature profile, we use it to calculate the column-averaged cross section by using equation (7) and retrieve the column density profile again. We repeat this process until the iteration converges, which typically occurs after a few iterations.

Figure 8 shows the retrieved column density and the temperature profiles for the first and last iteration of the ST42 retrieval. The final converged column density profile differs from the first iteration by a factor of 1.6 at 915 km, a factor of 1.04 at 1500 km and a factor of 2.3 at 2500 km. These results agree with the range of changes in the fitted column densities that we found in Section 2.4 by changing the temperature of the absorption cross section. This indicates that the uncertainty in temperature is the most significant source of uncertainty in the retrieved density profiles and the iteration is critical for getting the density retrieval right. *After the retrieval converges, the final uncertainties in the retrieved column density profile for ST42 are 4% at 915 km, 7% at 1500 km and 24% at 2000 km.*

2.8. **Inversion of the column density profiles.** After the iteration converges or occasionally during the iteration, we also invert the column density profile to retrieve number densities (we refer to the inverted number density profile as 'direct retrieval' number densities to distinguish it from the forward model number density profile). We use a Tikhonov regularization technique to achieve this (Quémerais et al., 2006; Koskinen et al., 2011). We write equation (9) in matrix notation as

$$\mathbf{N} = \mathbf{M}\mathbf{n} + \mathbf{e} \tag{22}$$

where $\mathbf{M}$ is an upper triangular matrix and $\mathbf{e}$ is a vector of measurement uncertainties on the retrieved column densities. Because of the retrieval uncertainties and discretization, there is no unique vector $\mathbf{n}$ that solves this equation. Instead, we seek a statistical solution that minimizes the cost function

$$\chi^2 = \xi_0 \mathbf{n}^{\mathrm{T}} \mathbf{H} \mathbf{n} + (\mathbf{N} - \mathbf{M}\mathbf{n})^{\mathrm{T}} \, \mathbf{S_e}^{-1} \, (\mathbf{N} - \mathbf{M}\mathbf{n}) \tag{23}$$

where ξ_0 is the Tikhonov regularization parameter and $\mathbf{S_e}$ is the diagonal covariance matrix constructed of squared measurement errors on the column densities. The regularization matrix is (Quémerais et al., 2006):

$$\mathbf{H} = \mathbf{L}^{\mathrm{T}} \mathbf{S_H}^{-1} \mathbf{L} \tag{24}$$

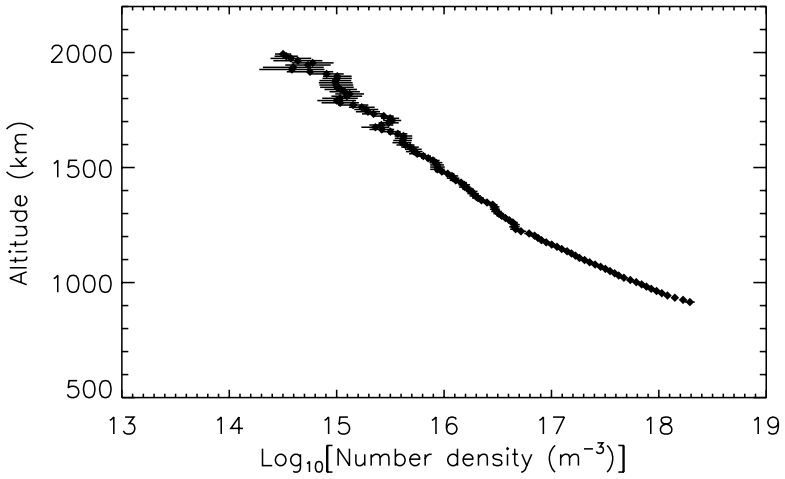

FIGURE 9. Direct retrieval (inverted) number density profile of H_2 retrieved for occultation ST42.

where $\mathbf{S_H}$ is a diagonal covariance matrix built of the squared uncertainties of the number densities and the matrix $\mathbf{L}$ is:

$$\mathbf{L} = \begin{pmatrix} -1 & 1 & 0 & 0 & ... & 0 \\ 1 & -2 & 1 & 0 & ... & 0 \\ 0 & 1 & -2 & 1 & ... & 0 \\ ... & ... & ... & ... & ... & ... \\ 0 & ... & 0 & 1 & -2 & 1 \\ 0 & ... & 0 & 0 & 1 & -1 \end{pmatrix}. \tag{25}$$

Because the number density uncertainties that enter equation (24) are not known *a priori*, the inversion is an iterative process. For each iteration $k+1$, the number density estimator is

$$\mathbf{n}_{k+1} = \left[\mathbf{K}^{\mathrm{T}}{\mathbf{S_e}}^{-1}\mathbf{K} + \xi_0\mathbf{L}^{\mathrm{T}}({\mathbf{S_H}}^{-1})_k\mathbf{L}\right]^{-1}\mathbf{K}^{\mathrm{T}}{\mathbf{S_e}}^{-1}\mathbf{N}. \tag{26}$$

The first density estimator ($k = 1$) is obtained by minimizing equation (23) with $\mathbf{H} = 0$. This action is known as the 'direct inversion' that tends to result in large uncertainties on the derived number densities. Iterative Tikhonov regularization is designed to decrease the uncertainty by effectively smoothing the densities in altitude (see matrix 25). The strength of the smoothing and the effective altitude resolution is controlled by the parameter ξ_0. For example, the effective altitude resolution of our inverted density profile for ST42 is about 30 km (see Figure 9) while the sampling resolution of the occultation is about 10 km. The uncertainty on the retrieved number densities for each iteration and the final results, propagated through the inversion, is given by the diagonal elements of

$$\mathbf{S_n} = \left(\mathbf{K}^{\mathrm{T}}{\mathbf{S_e}}^{-1}\mathbf{K} + \lambda_0\mathbf{L}^{\mathrm{T}}{\mathbf{S_H}}^{-1}\mathbf{L}\right)^{-1}. \tag{27}$$

For ST42, this uncertainty is 10% at 915 km, 16% at 1500 km and 17% at 2000 km.

2.9. **Direct temperature retrieval.** After the number density retrieval has converged, we retrieve the temperature directly from the final number density profile, in addition to the usual forward model temperature fit. Effectively, we fix the temperature above 1700–1800 km to the isothermal fit temperature and integrate downward to calculate pressure from the equation of hydrostatic equilibrium below this altitude. We then use the

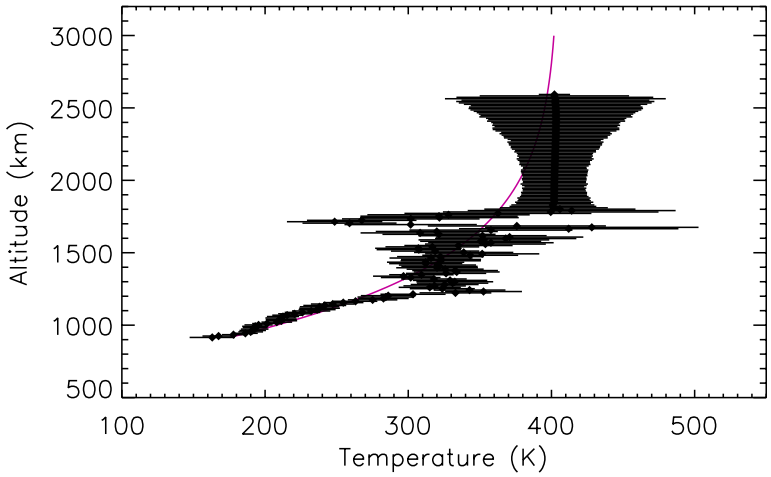

FIGURE 10. Direct retrieval temperature profile with uncertainties for ST42. Note that we fitted the density profile with an isotherm above 1800 km prior to retrieval. The purple line is the forward model temperature profile.

retrieved pressure to calculate temperature from the ideal gas law. We use a Monte Carlo-type procedure to determine the uncertainty in the retrieved temperature profile based on 1000 trial values for the densities at different altitudes. This procedure is adapted from Snowden et al. (2013) and outlined by Koskinen et al. (2015) for Saturn. Figure 10 shows a comparison of the forward model temperature fit with the direct temperature retrieval for ST42. The formal uncertainty in direct retrieval temperature is 10% at 915 km, 10% at 1500 km and 13% at 1800 km. *We conclude, based on these uncertainties and the uncertainties derived above for the column and number density profiles, that an overall uncertainty of 20–30% captures the uncertainty in the number densities retrieved with the iterative retrieval below 2000 km for an effective altitude resolution of 30 km.*

3. TEMPORAL AND SPATIAL BEHAVIOR FROM THE OCCULTATION DATA

3.1. **Light curves.** In this section, we focus on the stability and overall density structure of Saturn's equatorial thermosphere as derived from the occultation data. The left panel of Figure 11 shows the comparison of the mean transmission as a function of radial distance for the 960–970 Å wavelength bin that includes absorption by a strong H_2 absorption band (see Figure 7) based on the occultations obtained in 2013–2017 (Table 1) that best represent the expected state of the atmosphere during the Grand Finale. The variation in these light curves is largely due to the expected latitude variation of an oblate planet. This is illustrated by the right panel that shows the half-light (i.e., transmission equal to 0.5) radial distance of the light curves as a function of planetocentric latitude, clearly showing the equatorial bulge with an amplitude of about 400 km in density levels ranging from the latitude of 12S to 14N.

In order to test whether the data points in Figure 11 comply with the expected shape of the atmosphere, we derived the equatorial radius corresponding to each radius and latitude on surfaces of constant gravitational potential in the AS model. If the atmosphere is horizontally uniform and the model is correct, the equatorial radii should be the same for each point. Figure 12 show the resulting equatorial radii. They show a residual equatorial bulge with a reduced amplitude of about 80 km at 12S–14N. This is not

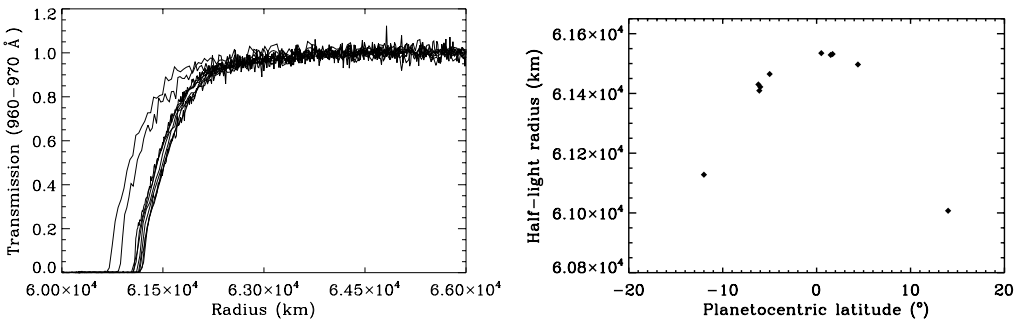

FIGURE 11. **Left**: Mean transmission at 960–970 Å as a function of radial distance from Saturn's center for occultations from 2013–2017 (Table 1). **Right**: Radial distance to the half light points of the light curves on the left as a function of planetocentric latitude.

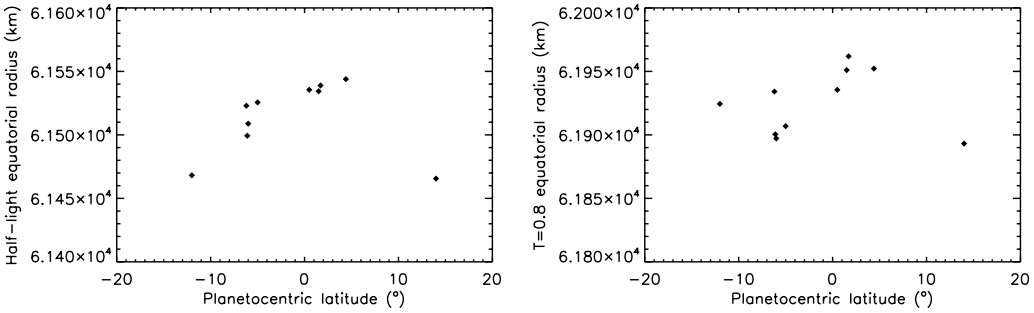

FIGURE 12. **Left**: Equatorial radii of the surfaces of constant gravitational potential in the AS model corresponding to the half light radii and latitudes in Figure 11. **Right**: The same for the level where transmission equals 0.8.

surprising because the AS model was not designed to capture the equatorial shape exactly and does not necessarily apply at high altitudes in the thermosphere. The residual that we observe is, however, about twice as large as the expected error margin of about ±20 km for the AS model and our result could, for example, imply the existence of a more pronounced zonal jet around the equator in the upper atmosphere. Alternatively, the equator could be warmer than the surrounding latitudes, although in that case the similarity of the residual with the equatorial bulge would be a mere coincidence.

Figure 12 also shows the corresponding equatorial radii for the level where transmission equals 80% as a function of planetocentric latitude. This is the level of transmission roughly consistent with the spacecraft altitude during the Grand Finale in-situ measurements. The amplitude of the deviation from the AS model is similar to the half-light level but the equatorial bulge is less pronounced in the southern hemisphere. This could be due to cooler thermospheric temperatures around the latitudes of 5-6S relative to the occultation near 12S (see Figure 13).

The above results are based on light curves only i.e., they are robust and independent of any uncertainties in the density and temperature retrieval. In general, these results indicate that Saturn's low-latitude thermosphere has exhibited relative stability during the four years leading to the Grand Finale. This appears remarkable when one considers the fact that solar heating is negligible in the thermosphere, which is instead believed to be heated by more transient mechanisms such as waves or redistribution of energy from the aurora, both of which are expected to be variable. Our results demonstrate that the

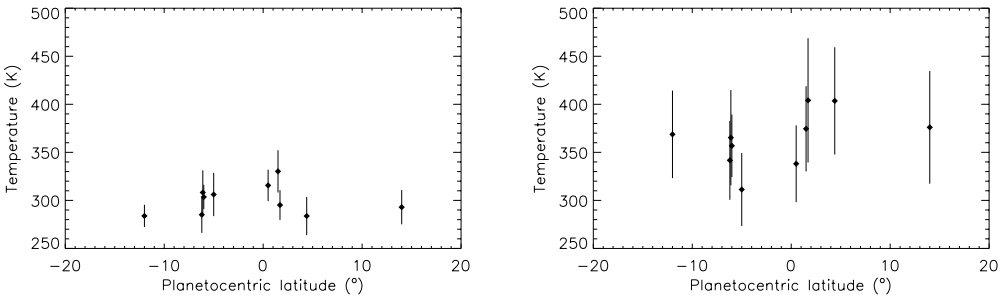

FIGURE 13. **Left**: Temperatures corresponding to the half light equatorial radii in Figure 12. **Right**: At level where transmission equals 0.8.

heating mechanism in Saturn's thermosphere must operate continuously over long time scales while producing only small perturbations to the mean state of the atmosphere on short time scales.

Finally, we conclude with a brief exploration on how the trends observed in the light curves above are reflected by the retrieved densities and temperatures. First, we compared the half light densities retrieved from each occultation. The half light density at 960–970 Å is about 5×10^{16} m^{-3} with a standard deviation of ±12%, consistent with the expected uncertainty of the iteratively retrieved number density profiles. At the level where transmission equals 0.8 the density is about 3.4×10^{15} m^{-3} with a standard deviation of ±20%. The left panel of Figure 13 shows the temperatures at the 960–970 Å half light radius as a function of planetocentric latitude. The spread in the observed temperature can represent the statistical error of the iterative retrieval, changes with time or small meridional variations.

REFERENCES

Abgrall, H., Roueff, E., Launay, F., Roncin, J.-Y., Subtil, J.-L., 1993a. Table of the Lyman band system of molecular hydrogen. Astron. Astrophys. Suppl., 101, 273–321.

Abgrall, H., Roueff, E., Launay, F., Roncin, J.-Y., Subtil, J.-L., 1993b. Table of the Werner band system of molecular hydrogen. Astron. Astrophys. Suppl., 101, 323–362.

Abgrall, H., Roueff, E., Drira, I., 2000. Total transition probability and spontaneous radiative dissociation of B, C, B', and D states of molecular hydrogen. Astron. Astrophys. Supp., 141, 297–300.

Anderson, J. D., Schubert, G., 2007. Saturn's gravitational field, internal rotation, and interior structure. Science, 317, 1384–1387.

Deakin, R. E., Hunter, M. N., 2013. Geometric geodesy, Part A. RMIT University, Melbourne, Australia.

Esposito, L. W., et al., 2004. The Cassini ultraviolet imaging spectrograph investigation. Space Sci. Rev., 115, 299–361.

Gates, L. W., 2004. Derivation of the equations of atmospheric motion in oblate spheroidal coordinates. J. Atmos. Sci., 61, 2478–2487.

Koskinen, T. T., et al., 2011. The mesosphere and thermosphere of Titan revealed by Cassini/UVIS stellar occultations. Icarus, 216, 507–534.

Koskinen, T. T., et al., 2013. The density and temperature structure near the exobase of Saturn from Cassini UVIS solar occultations. Icarus, 226, 1318–1330.

Koskinen, T. T., et al., 2015. Saturn's variable thermosphere from Cassini/UVIS occultations. Icarus, 260, 174–189.

Koskinen, T. T., et al., 2016. The detection of benzene in Saturn's upper atmosphere. Geophys. Res. Lett., 43, 7895–7901.

Koskinen, T. T., Guerlet, S., 2018. Atmospheric structure and helium abundance on Saturn from Cassini/UVIS and CIRS observations. Icarus, 307, 161–171.

Lindal, G. F., Sweetnam, D. N., Eshleman, V. R., 1985. The atmosphere of Saturn: An analysis of the Voyager radio occultation measurements. Astron. J., 90, 1136–1146.

McClintock, W. E., Lawrence, G. M., Kohnert, R. A., Esposito, L., 1993. Optical design of the Ultraviolet Imaging Spectrograph for the Cassini mission to Saturn. Opt. Eng., 32, 12.

Press, W. H., Teukolsky, S. A., Vetterling, W. T., Flannery, B. P., 1992. Numerical Recipes in FORTRAN: The Art of Scientific Computing (2nd ed.). Cambridge University Press, Cambridge, England.

Quémerais, E., et al., 2006. Stellar occultations observed by SPICAM on Mars Express. J. Geophys. Res., 111, E09S04.

Shemansky, D. E., Liu, X., 2012. Saturn upper atmosphere structure from Cassini EUV and FUV occultations. Can. J. Phys., 90, 817–831.

Snowden, D. S., et al., 2013. The thermal structure of Titan's upper atmosphere, I: Temperature profiles from Cassini INMS observations. Icarus, 226, 552–582.

Yelle, R. V., et al., 1996. Structure of Jupiter's upper atmosphere: Predictions for Galileo. J. Geophys. Res., 101, 2149–2161.

Cassini Program

Proximal Orbit Atmospheric Transits Contingency Plan D-94787

Revision B

Prepared By:

Erick Sturm Mission Planning Team Lead	Date

Approved By:

Earl Maize Project Manager	Date
William Heventhal Science Planning & Sequencing Team Lead	Date
Julie Webster Spacecraft Operations Office Manager	Date

August 2017

Jet Propulsion Laboratory
California Institute of Technology
4800 Oak Grove Drive
Pasadena, CA 91109-8099

Change Log

Revision	Date	Description
0	June 2015	Document created
A	October 2015	Incorporated comments from MPWG review
B	August 2017	Updated to from minimum aero-torque option to pop-up option

Table of Contents

1 Introduction

1.1 Purpose and Scope

The purpose of the Cassini Program Proximal Orbit Atmospheric Transits Contingency Plan is to provide a concise, comprehensive overview of the plan for detecting and responding to a denser-than-predicted Saturn atmosphere in the Proximal Orbits.

1.2 Change Control

Change control for this document is specified in the Cassini Program Mission Operations Configuration Management Plan. All revisions to this documents must be approved by the signatories listed on the title page.

1.3 Applicable Documents

1) Mission Operations Configuration Management Plan, Cassini Program, CASTL 699-514

1.4 Reference Documents

1) Solstice Mission Plan, Cassini Program, CASTL 699-100
2) Saturn Thermosphere Model, Summary Presentation Package on MP website

2 Background

2.1 Proximal Orbits

The proximal orbits, also known as Cassini's Grand Finale, are the final 22½ orbits of the Cassini Solstice Mission, which conclude with the spacecraft permanently entering Saturn's atmosphere. They get their name from their proximity to Saturn and its rings as their periapsis passages fly between the lower fringes of the D ring and the upper reaches of Saturn's atmosphere. Figure 1 shows Cassini's Grand Finale, which starts at the apoapsis of Rev 271. After completing 22 full orbits (shown in blue), the spacecraft will make the journey from Titan to Saturn one last time (shown in orange). Finally, diving deep into Saturn's atmosphere on Rev 293, it will be destroyed.

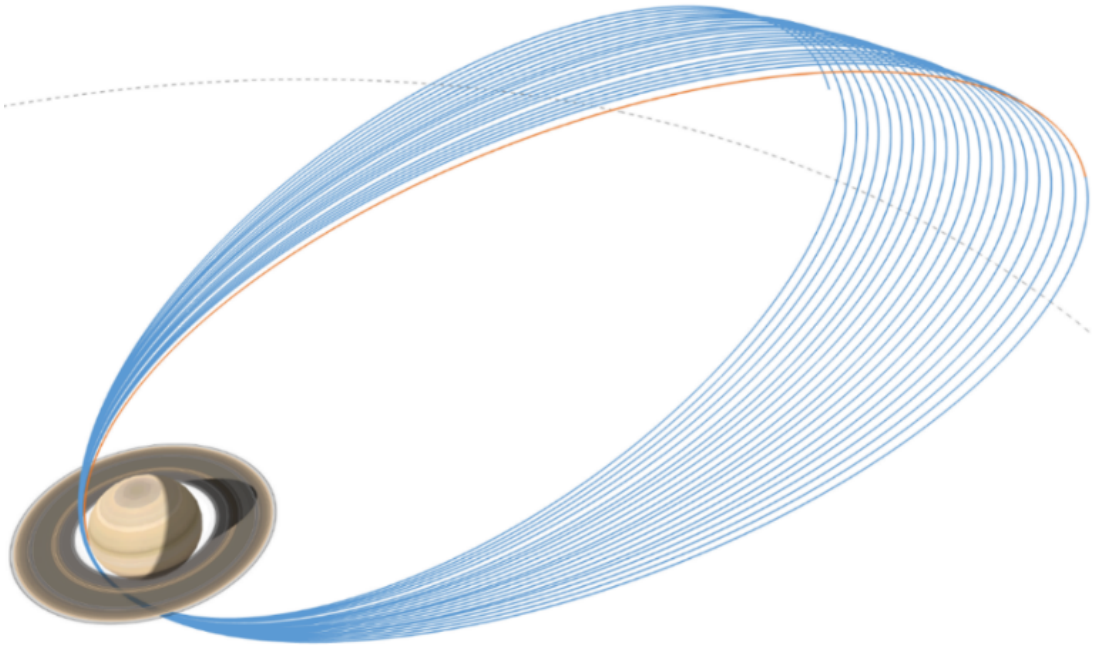

Figure 1: Cassini's Grand Finale with the 22 full proximal orbits in blue, the final half-orbit in orange, and Titan's orbit in gray.

While the Grand Finale consists of 22½ orbits, it is completed less than five months from its start. The short duration is due to the size of the orbits; with periapsis so close to Saturn and apoapsis only slightly outside of Titan's orbit, the period of each orbit is less than one week. Thus, the entire span of this scenario is about one month.

2.1.1 The Final Five

While all the proximal orbits have periapsis passages between Saturn's atmosphere and rings, the exact altitudes of periapsis vary by over 2000 km. Distant, non-targeted Titan flybys out near the orbits' apoapses cause these differences. As shown in Figure 2, the altitudes of the final five orbits (revs 288-292) are the lowest in the Grand Finale by 1000 km.

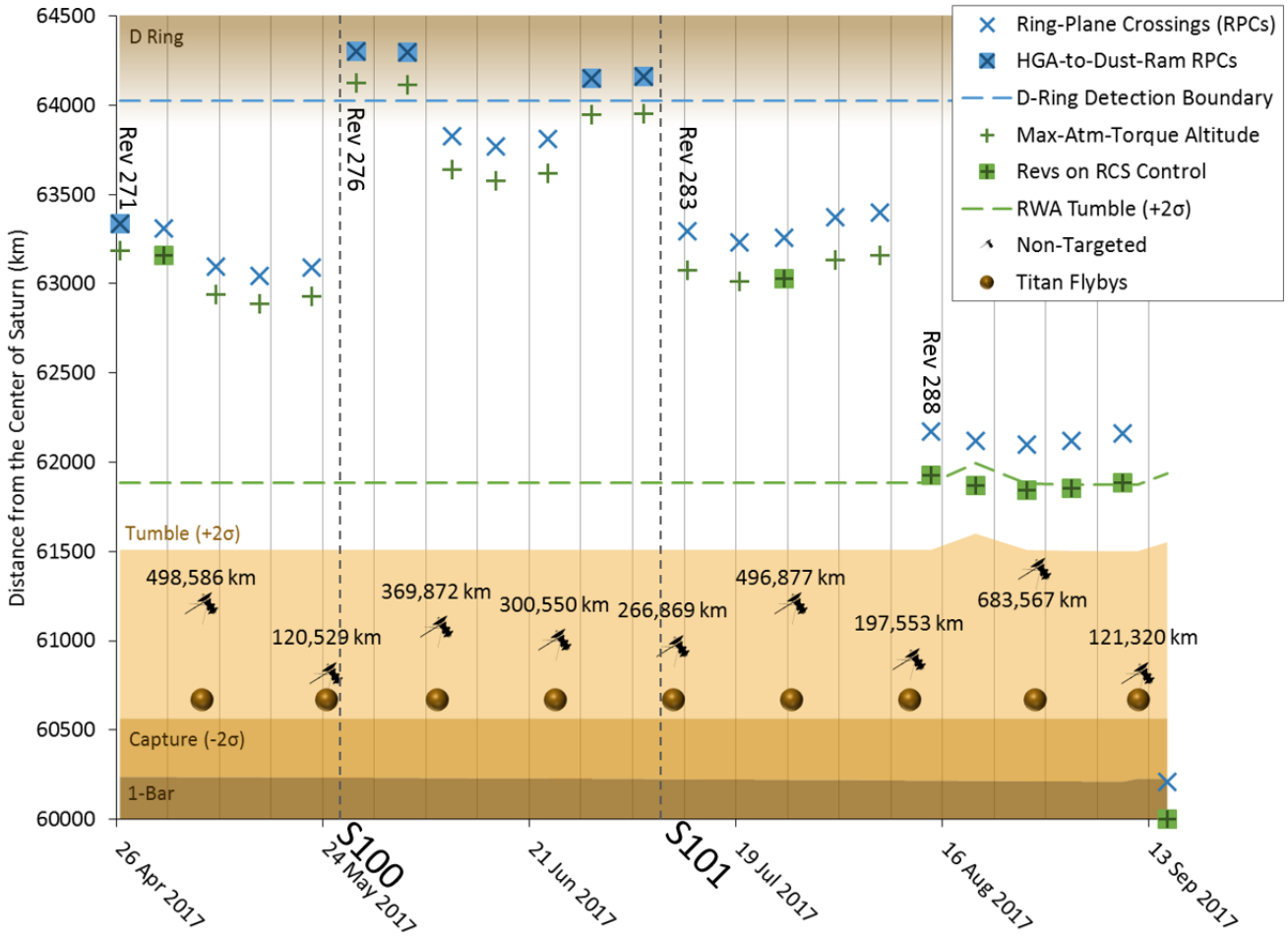

Figure 2: Variations in the altitudes of ring-plane crossings (blue) and points of maximum-atmospheric-torque (green) during the proximal orbits. The non-targeted Titan flyby distances that cause the variations are also shown (on a separate scale).

Zooming in on Figure 2 to show only the final five orbits, results in Figure 3, which shows that the final five orbits go progressively deeper into Saturn's atmosphere until Rev 290 and then start to climb back out again.

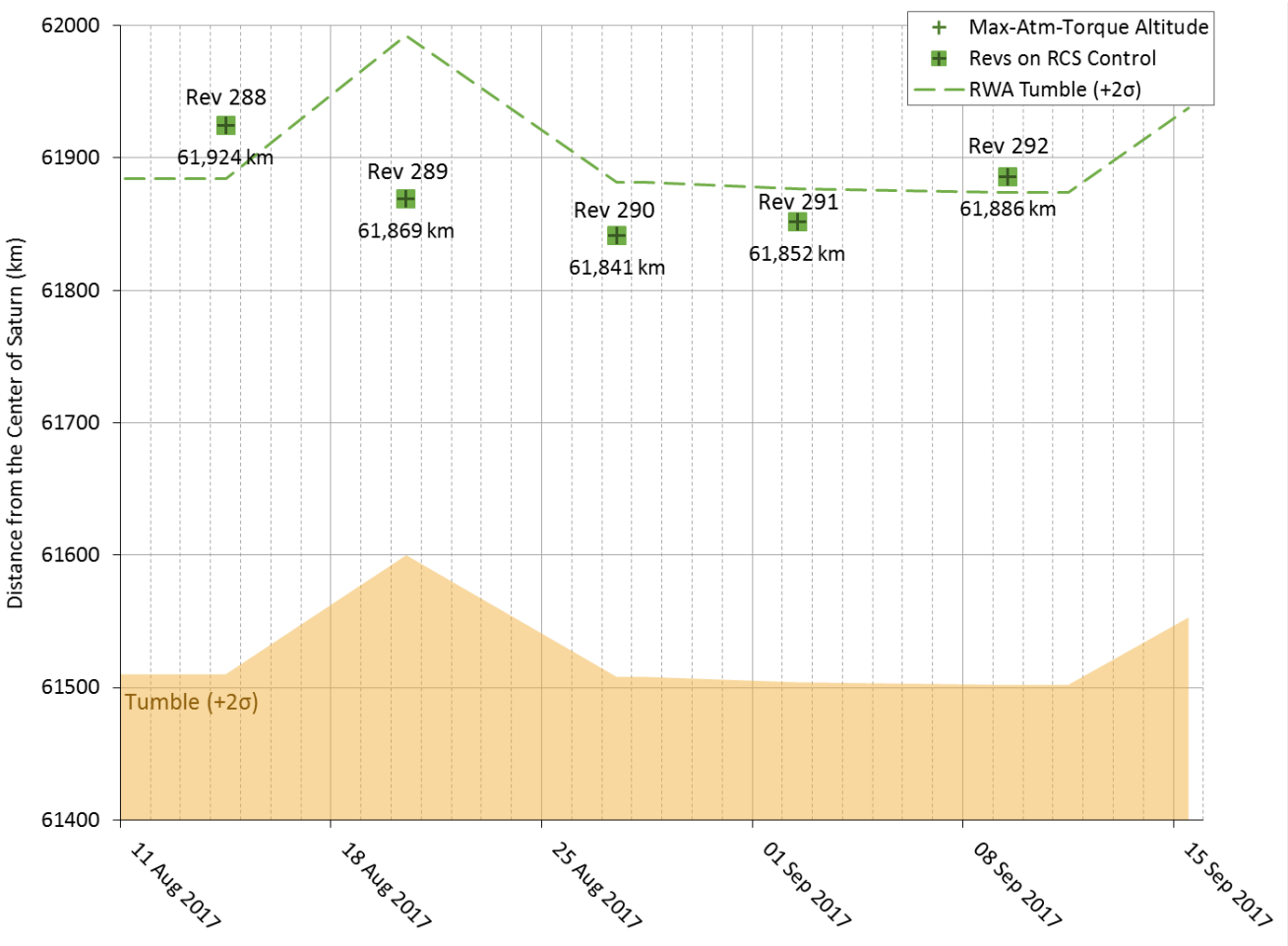

Figure 3: Maximum-atmospheric-torque altitudes of the final five proximal orbits.

Figure 3 also shows that there is a 300-400 km margin between the spacecraft altitudes and the 2σ tumble boundary. Back when these orbits were designed, this margin was only tens-of-kilometers; however, recent occultation data suggest that Saturn's atmosphere is contracting and with it, the tumble altitude. For additional detail, see reference document by T. Koskinen et al.

2.1.2 End of Mission

The Cassini Program End of Mission Scenario (D-96083) describes the final orbit of the Cassini mission in detail; however, a very brief summary is given here for reference.

The last non-targeted Titan flyby, 292TI, is just before apoapsis of Rev 293 and sets up the final plunge of the spacecraft into Saturn. The last 14.5 hours of the mission will have continuous DSN coverage with the final 3.5 hours providing a near-real-time downlink. Figure 4 shows the geometry of the final orbit with key events labeled.

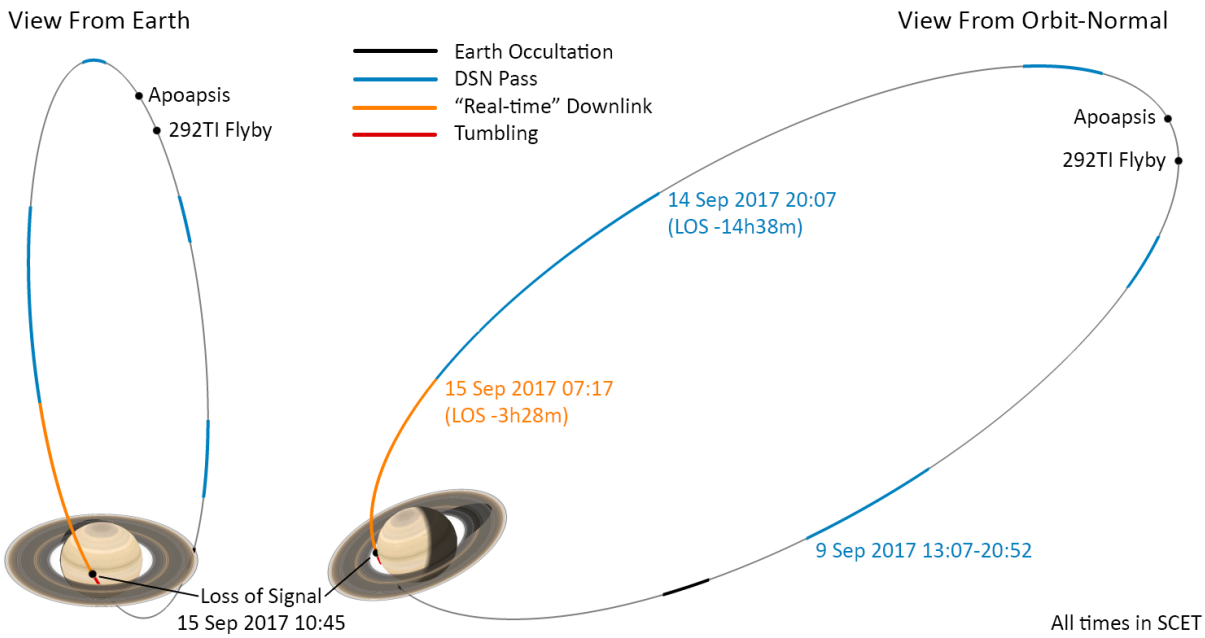

Figure 4: End-of-mission orbit geometry from Rev 292 periapsis to Saturn impact. On the left, is the view from Earth. On the right, is the view along the orbit normal. Times shown are in spacecraft event time (SCET).

The project is currently predicting loss of signal to occur on September 15, 2017 at 10:41 (SCET). The only effect this contingency would have on the End of Mission is a slight change in loss of signal time due to the small trajectory change from a pop-up maneuver.

2.2 Saturn Thermosphere Model

The Saturn thermosphere model is a two-dimensional model of density that varies with radius and latitude. D. Strobel and T. Koskinen developed the model through analysis of ultraviolet solar and stellar occultations of Saturn's atmosphere. The Saturn Thermosphere Model presentation available on the Cassini mission-planning website documents the details of the model.

The model provides estimates for the atmospheric densities the spacecraft will fly through during the proximal orbits. When combined with the planned attitudes of the spacecraft, the Cassini flight-system-dynamics simulator (FSDS) can predict the peak RCS thruster duty cycles required to fight the atmospheric torque. In addition, the model, the planned attitudes, and the maximum RCS thruster torque combine to define a spacecraft tumble boundary, the radius at which the density is sufficient to overwhelm the RCS thrusters and cause the spacecraft to lose control authority. This boundary is shown as the light yellow area in Figure 2 and Figure 3.

The model was originally developed using occultation data from 2009. While not fully known at the time, these data corresponded to an expanded state of Saturn's thermosphere. As a result, the tumble boundary was high and margin was low; the project was concerned with flying through too much atmosphere, not too little. More recent occultation data suggest that not only has the expansion of the atmosphere stopped but that a contraction has likely begun. The most recent version of the model (January 2017) shows that the current state is about two-thirds the density of the 2009 values.

2.3 Cassini Spacecraft

The two key subsystems of the Cassini spacecraft related to this plan are the attitude and articulation control subsystem (AACS) and the propulsion module subsystem (PMS). The AACS will serve as a density detector during the atmospheric transits of the final five proximal orbits, while the PMS will perform the contingency pop-up maneuver.

2.3.1 Attitude and Articulation Control

The AACS has two methods for maintaining control authority of the spacecraft: the reaction wheel assemblies (RWAs) and the reaction control system (RCS) thrusters of the PMS. The majority of the time, the spacecraft is on RWA control, occasionally switching to RCS control for momentum management. The spacecraft uses the RCS most often for high-speed turns and during low Titan flybys, to maintain control authority against the large torque exerted by Titan's atmosphere. Similarly, the spacecraft will be on RCS control during Saturn atmospheric transits in the proximal orbits. The project will take advantage of this in order to estimate the density of Saturn's thermosphere, as the percentage of time the thrusters fire during a transit is directly proportional to the atmospheric torque, which is a function of density. Thruster duty cycle has the additional advantages of being relatively quick to downlink and calculate, as well as an accuracy of about ±1% (2σ).

2.3.2 Propulsion Module

The Cassini propulsion module subsystem is comprised of two separate propulsion systems: a bipropellant system with the main-engine assembly (MEA) and a monopropellant, reaction-control system (RCS). The locations of the main engines and RCS thruster pods are shown in Figure 5.

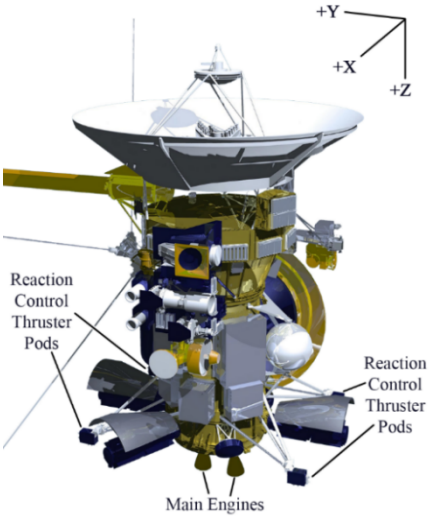

Figure 5: Cassini Spacecraft Thrusting Components

The Cassini spacecraft has two main engines and four RCS pods, each with four thrusters. Each RCS pod has two thrusters pointed along the +Z-axis and two thrusters pointed along either the +Y-axis or the –Y-axis depending on whether the pod is located on the +Y or –Y side of the X-Z plane. The thrusters are also separated into two branches, A and B, each with four +Z thrusters, two +Y thrusters, and two –Y thrusters. The spacecraft currently uses the B branch due to premature degradation of some of the +Z thrusters in the A branch. While there is no indication of any B branch thruster degradation at this time, should it occur before the end of mission, the spacecraft could operate in a mixed branch mode, using thrusters from both the A and B branches.

The bipropellant system uses nitrogen tetroxide (NTO) as its oxidizer and monomethylhydrazine (MMH) as its fuel. The spacecraft uses the MEA solely for orbital trim maneuvers greater than 250 mm/s. The spacecraft uses the RCS for small translational maneuvers, attitude control, and spacecraft momentum management. The spacecraft can also use the RCS for larger translational maneuvers, the maximum being approximately 4 m/s in a single burn executed during a standard nine-hour pass.

2.4 Orbital Trim Maneuvers

An orbital trim maneuver (OTM) requires time for orbit determination, maneuver design, and execution windows (primary and back-up). A pop-up maneuver is most efficient when performed at apoapsis, which means the Navigation Team would have a little over three days to obtain tracking data, determine the orbit, and design the maneuver. The minimum duration required to perform the aforementioned tasks is shown in Table 1.

Table 1: Minimum durations for pop-down maneuver design.

Task	Minimum Duration
Obtain tracking data (two, daily, nine-hour passes)	33 hours
Orbit determination	3 hours
Maneuver design	3 hours
Navigation team review	1 hour
Total	**40 hours**

2.5 Propellant Levels

The amount of propellant predicted to be remaining in the spacecraft during the proximal orbits is of vital importance to feasibility of this scenario, as without sufficient propellant the spacecraft could not perform a pop-up maneuver.

As of the completion of OTM-472 (15 Jul 2017), there are 2.25 m/s of bipropellant left in the tanks (90^{th} percentile). However, even with the assumption that the spacecraft depleted its bipropellant, there are about 26 m/s of margin (90^{th} percentile) over the ΔV required to fly the remaining.

2.6 Nominal Plan for Atmospheric Transits

Of the 22 proximal orbits, only five (the final five) are low enough in Saturn's atmosphere to require switching to thruster control. The lowest of the five, Rev 290, is predicted to have tens-of-kilometers of margin (3σ) between its trajectory and the tumble boundary (the altitude at which the atmosphere is thick enough that the spacecraft would lose control authority without performing a pop-up maneuver). Given that, the nominal plan is to fly the final five proximal orbits on thruster control and not baseline in a pop-up.

3 Environmental Hazard Detection

As discussed in section 2.3.1, this plan uses the AACS as a density detector. By analyzing the RCS thruster duty cycles during the atmospheric transits and comparing them to the predicted values, the project can infer the density of the atmosphere. Each atmospheric transit will result in two, peak, duty cycle estimates, one for the Y-thrusters and one for the Z-thrusters. The AACS team calculated the predicted peak Y and Z duty cycles for the atmospheric transits of the final five orbits. In addition, the Mission Planning team did an uncertainty analysis to

determine the feasibility of distinguishing differences between predicted and actual duty cycles caused by the density of the atmosphere from those caused by other uncertainties. The sources of the other uncertainties that MP considered are navigation dispersions, spacecraft aerodynamics, mass properties, and RCS characteristics. The sources and their associated uncertainty values are shown in Table 2.

Table 2: Uncertainty sources of the duty cycle uncertainty analysis

Source	Unc. (1σ)	Units
Duty Cycle Calculation	0.5%	---
Navigation		
Radius	6.9	km
Velocity	10	m/s
Spacecraft		
Drag Coefficient	0.033	---
Drag Area	0.117	m^2
Center of Press.		
CPx	0.011	m
CPy	0.204	m
CPz	0.080	m
Center of Mass		
CMx	0.003	m
CMy	0.007	m
CMz	0.019	m
RCS Thrust	0.010	N

The results of the uncertainty analysis are shown in Figure 6. The peak duty cycles (Y and Z) for the final five orbits are shown with 2σ error bars from the sources identified above assuming a nominal atmosphere as predicted by the model, as well as 2σ-off-nominal atmospheres (high and low).

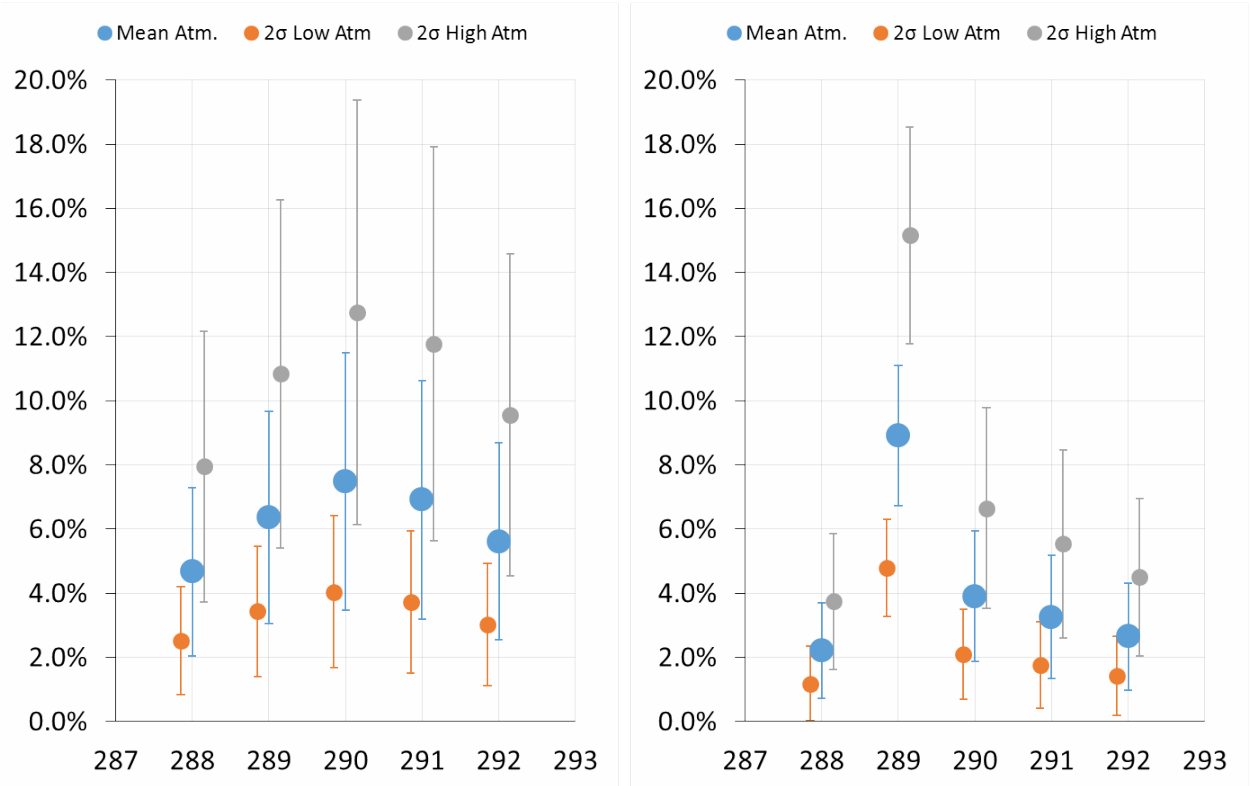

Figure 6: Predicted peak duty cycles of the RCS thrusters during the final five proximal orbits for nominal (blue) and off-nominal atmospheres, high (gray) and low (orange). Y duty cycle is on the left, Z is on the right.

Both plots in Figure 6 show that the predicted duty cycles, even for a 2σ high atmosphere, are well below the RCS limit. As a point of reference, the T57 Titan flyby, the lowest in the Cassini Equinox Mission, had a peak duty cycle of 69%. The plots also show that Z-thruster duty cycle is a slightly better indicator of atmospheric density than the Y-thruster duty cycle, though they both suffer from the uncertainties in Table 2 making it difficult to distinguish between atmospheric densities.

The Y-thruster duty cycles have significantly larger error bars due to the larger uncertainty in the y-coordinate of the center of pressure. Looking back at Table 2, the y-coordinate of the center of pressure has an uncertainty that is nearly an order of magnitude larger than the other two coordinates. The Z-thruster duty cycles show less overlap between the nominal and 2σ-off-nominal atmospheres; however, Rev 289 is the only one with a distinct separation between them, a result of the planned attitude during that transit. However, even given these results, the spacecraft should the atmosphere be thick enough to pose a threat to the spacecraft the duty experienced on Rev 288 would have to be off the above charts, literally, and as such, could easily be distinguished from any uncertainty in duty cycle caused by the sources in Table 2.

4 Risk Assessment and Decision Process

The results of the duty cycle analysis from AACS and MP during the transits will be used to reassess the risk of losing control authority due to atmospheric torque on future transits. The results of this analysis will be a modified Saturn density profile based on engineering measurements. If, when this new model is applied, the predicted thruster duty cycle of any subsequent transit is exceeds 70% (2σ), the project will execute the contingency response (in the following section) to mitigate the risk. The decision to execute the contingency response will be made by the project manager with consultation from the MP, SCO, PS, and SAUL teams.

5 Contingency Response

If the atmospheric density encountered during the first transit is found to be significantly higher than predicted, the spacecraft will perform a contingency pop-up maneuver near the Rev 289 apoapsis. Two constraints envelope the magnitude of such a maneuver: maximum burn time in a single nine-hour pass and minimum periapsis change to reach a safe thruster duty cycle on subsequent atmospheric transits. The former requires the burn to be no larger than 4 m/s if performed with the RCS thrusters; the latter depends entirely on the state of the atmosphere. However, the maximum 4 m/s maneuver is capable of raising periapsis by around 250-300 km, which is equivalent to about 1.5 scale heights. Thus, that maneuver could reduce a predicted duty cycle of 285% to the safe limit of 70%. Given that the current 2σ-high predict for the largest peak duty cycle is 31%, it is extremely unlikely that the spacecraft would require more the 4 m/s to reach a safe altitude.

6 Reference Timeline

The events necessary to prepare and implement the atmospheric transit contingency are shown in Table 3.

Table 3: Timeline of Key Events

Relative Time	Date	Time (PDT)	Team	Event/Action
OTM -2.5 days	8/14	15:00	NAV	Deliver OD to MP
	8/14-15	18:45-00:45		Post-periapsis downlink
OTM -43 hr	8/15	09:00	AACS	Deliver duty cycle data to MP
OTM -41 hr	8/15	11:00	MP	Deliver periapsis target to NAV
OTM -34 hr	8/15	18:00	NAV	Preliminary navigation review
OTM -13 hr	8/16	13:00	NAV	Final navigation review
	8/16-17	22:15-07:15		OTM-473 Pass
OTM	8/17	04:14		OTM-473 Pop-up

A plot of the spacecraft trajectory from the Rev 288 transit to the Rev 289 transit is shown in Figure 7. The black regions depict the periods during which the Earth is occulted by the Rings/Saturn. The blue regions are the planned DSN passes between the two transits. The first of which will playback the duty cycle data from the Rev 288 transit.

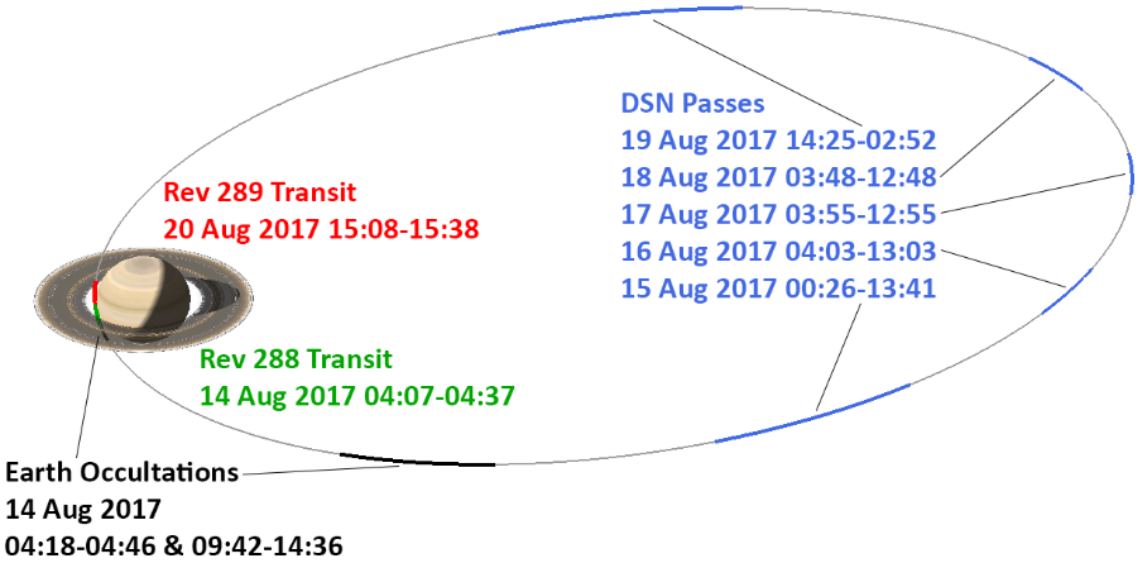

Figure 7: Trajectory from Rev 288 transit to Rev 289 transit with Earth occultations (black) and planned DSN passes (blue).

Cassini Program

Proximal Orbit Pop-Down Scenario D-96898

Revision 0

Prepared By:

Erick Sturm Date
Mission Planning Team Lead

Approved By:

Earl Maize Date
Project Manager

Duane Roth Date
Navigation Team Lead

Julie Webster Date
Spacecraft Operations Office Manager

Kathryn Weld Date
Science and Uplink Office Manager

January 2017

Jet Propulsion Laboratory
California Institute of Technology
4800 Oak Grove Drive
Pasadena, CA 91109-8099

Change Log

Revision	Date	Changed By	Section(s)	Description
Preliminary	January 2016	E. Sturm		Document created
Prelim A	February 2016	E. Sturm	1.2 & 2.3 4.2 & 4.3	Revised bulleted lists and added prose Added/updated plots and discussion
Rev 0	January 2017	E. Sturm	All Table 4 Tbl. 2 & Fig. 6 3.5, 4.2, 6.2.1	Fixed typos, revised wording Extended to include last half of Rev 287 Updated for CPz of 0.080 m (was 0.028 m) Removed assumption of only using RCS

Table of Contents

1 Introduction

1.1 Purpose and Scope

This document explores a “make-better” science scenario for modifying the Cassini spacecraft’s trajectory to dip deeper into Saturn’s atmosphere during the final five Proximal orbits.

This scenario describes the detection of an atmosphere that is significantly less dense than predicted during the early orbits of the final five by comparing reaction control system (RCS) thruster duty cycles during atmospheric transits to their predicted values. The scenario also describes the locations and approximate sizes of orbit trim maneuvers (OTMs) that could reduce the periapsis altitudes during the latter of the final five orbits in order to obtain in-situ science data from a denser portion of Saturn’s atmosphere. The scenario goes on to describe the consequences of performing such maneuvers in terms of the timing errors they introduce into the remaining trajectory.

This document is in many ways the counterpart to the “Proximal Orbit Atmospheric Transits Contingency Plan”, D-94787, which describes the project’s plan for dealing with an atmosphere that is significantly more dense than predicted.

1.2 Objectives

The main objective of this document is to establish the feasibility of performing a pop-down maneuver during the final five orbits of the Cassini mission. To that end, the document provides the following:

- Predicted RCS thruster duty cycles for mean and off-nominal atmospheres
- Dates and times of the DSN passes for
    - RCS duty-cycle data downlink
    - Orbit determination tracking post-transit/pre-OTM
    - Pop-down OTM execution (prime and backup)
    - Orbit determination tracking post-OTM/pre-transit
- Time available for atmospheric state detection and pop-down OTM design
- Effects of pop-down OTM magnitude on periapsis altitude and orbital period

1.3 Change Control

Change control for this document is specified in the Cassini Program Mission Operations Configurations Management Plan. All revisions to this document require approval from the signatories listed on the title page.

1.4 Applicable and Reference Documents

Applicable documents levy requirements on this document. Reference documents provide supplemental information beyond that documented in this scenario.

1.4.1 Applicable Documents

1) D. Seal, Mission Engineering & Planning Roles & Responsibilities
2) Cassini Program, Mission Operations Configuration Management Plan, CASTL 699-514

1.4.2 Reference Documents

1) Cassini Program, Solstice Mission Plan, August 2012, CASTL 699-100, JPL D-81137
2) Cassini Program, Proximal Orbit Atmospheric Transits Contingency Plan, Rev. A, D-94787

3) Cassini Program, End of Mission Scenario, Rev. 0, D-96083
4) Cassini Program, Bipropellant Depletion Mission Contingency Plan, Rev. B, D-94788
5) Cassini Program, Saturn Thermosphere Model, D. Strobel & T. Koskinen, July 2015, MP Website
6) T. Koskinen, B. Sandel, R. Yelle, D. Strobel, I. Muller-Wodarg and J. Erwin, "Saturn's Variable Thermosphere from Cassini/UVIS Occultations," *Icarus,* vol. 260, pp. 174-189, 2015.
7) E. Sturm, T. Barber, D. Roth, “Ensuring Cassini’s End-of-Mission Propellant Margins”, IEEE Aerospace Conference, Big Sky, 2014
8) T. J. Barber and R. T. Cowley, "Initial Cassini Propulsion System In-Flight Characterization," in 38th AIAA/ASME/SAE/ASEE Joint Propulsion Conference, Indianapolis, 2002.

2 Scenario Overview

2.1 Synopsis

This scenario takes place during the final five orbits of the Cassini Solstice Mission. These orbits have the lowest periapsis altitudes of the entire Saturnian System tour spanning all the Cassini missions. As such, they provide a unique opportunity for obtaining in-situ science data of Saturn’s atmosphere. Recent occultations of Saturn’s atmosphere suggest that it may be contracting; because of this, the spacecraft may no longer be flying through atmosphere of sufficient density to obtain high quality in-situ measurements. This scenario describes the detection of a thin atmosphere and the method for modifying the trajectory to fly lower in the atmosphere while still respecting spacecraft health and safety limits.

The scenario begins with the downlink of the RCS thruster firing data for the Rev 288 atmospheric transit. The attitude and articulation control subsystem (AACS) team will use these data to calculate the peak thruster duty cycles of the transit, which will then be compared to the predicted values. This will give the project an initial indication of the state of Saturn’s atmosphere; however, no action will be taken until after the process is repeated at least one more time for Rev 289.

After the Rev 289 peak duty cycle is compared to the predict, the project has three options: continue with the current trajectory, invoke the atmospheric transit contingency plan (D-94787), or perform a pop-down maneuver near the next apoapsis to lower the following periapsis altitude. Note that *all* subsequent periapsis altitudes will be affected by the maneuver not just the next one, unless an additional maneuver is performed to return to the reference trajectory. These same options will also be available after the transits in revs 290 and 291. These choices yield eight different paths through this scenario, ranging from fully ballistic (no maneuvers) to performing a pop-down maneuver near the apoapses of all three revs, 290-292, each one dipping the trajectory a little farther into Saturn’s atmosphere. The baseline option is to perform a single pop-down maneuver near the Rev 291 apoapsis.

2.2 Requirements and Objectives

The only project-level requirement during this phase of the mission pertains to planetary protection, specifically proper disposal of the spacecraft, which the project will accomplish through permanent capture within Saturn’s atmosphere. For this scenario, that requirement effectively means that any modifications to the spacecraft’s flight path (i.e. pop-down maneuvers) shall maintain a ballistic, Saturn-impacting trajectory. Furthermore, the location of Saturn impact shall have line-of-sight to Earth, such that loss-of-signal coincides with loss of attitude control and not an occultation from Saturn or its rings.

In addition, this scenario shall respect the End of Mission Scenario (D-96083) and not invalidate any of the plans or assumptions contained therein, with the exception of the absolute timing of Saturn impact.

The sole objective of this scenario is to modify some portion of the spacecraft's trajectory during the final five proximal orbits such that it passes through the thickest atmosphere possible while still respecting spacecraft health-and-safety limits. In addition, the pop-down implementation should minimize the impact to the background sequence activities downstream of the maneuver.

2.3 Assumptions and Constraints

This scenario assumes the Cassini spacecraft to be operating nominally. The scenario also assumes sufficient propellant to perform not only the pop-down maneuver(s) but also the remaining planned spacecraft activities. An assumption is not made as to which type of propellant (hydrazine or bipropellant) must be used to perform the pop-down maneuver(s); however, bipropellant is considered the baseline option. Should a pop-down be performed with the RCS thrusters (hydrazine), the maximum ΔV of a single burn is constrained to no more than 4.0 m/s as larger burns would require more time than is available in a single, 9-hour DSN pass.

All analyses contained herein used the 150901 reference trajectory and the 2015-07 thermosphere model, unless noted otherwise.

3 Background Information

3.1 Proximal Orbits

The proximal orbits, also known as Cassini's Grand Finale, are the final 22½ orbits of the Cassini Solstice Mission, which conclude with the spacecraft permanently entering Saturn's atmosphere. They get their name from their proximity to Saturn and its rings as their periapsis passages fly between the lower fringes of the D ring and the upper reaches of Saturn's atmosphere. Figure 1 shows Cassini's Grand Finale, which starts at apoapsis of Rev 271. After completing 22 full orbits (shown in blue), the spacecraft will make the journey from Titan to Saturn one last time (shown in orange). Finally, diving deep into Saturn's atmosphere on Rev 293, it will be destroyed.

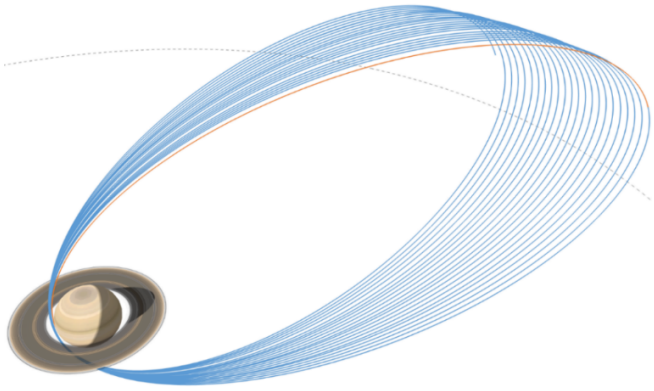

Figure 1: Cassini's Grand Finale with the 22 full proximal orbits in blue, the final half-orbit in orange, and Titan's orbit in gray.

While the Grand Finale consists of 22½ orbits, it is completed less than five months from its start. The short duration is due to the size of the orbits; with periapsis so close to Saturn and apoapsis only slightly outside of Titan's orbit, the period of each orbit is less than one week. Thus, the entire span of this scenario is about one month.

3.1.1 The Final Five

While all the proximal orbits have periapsis passages between Saturn's atmosphere and rings, the exact altitudes of periapsis vary by over 2000 km. Distant, non-targeted Titan flybys out near the orbits' apoapses cause these differences. As shown in Figure 2, the altitudes of the final five orbits (revs 288-292) are the lowest in the Grand Finale by 1000 km. As such, these orbits provide the opportunity to obtain the best in-situ atmospheric measurements of the Grand Finale.

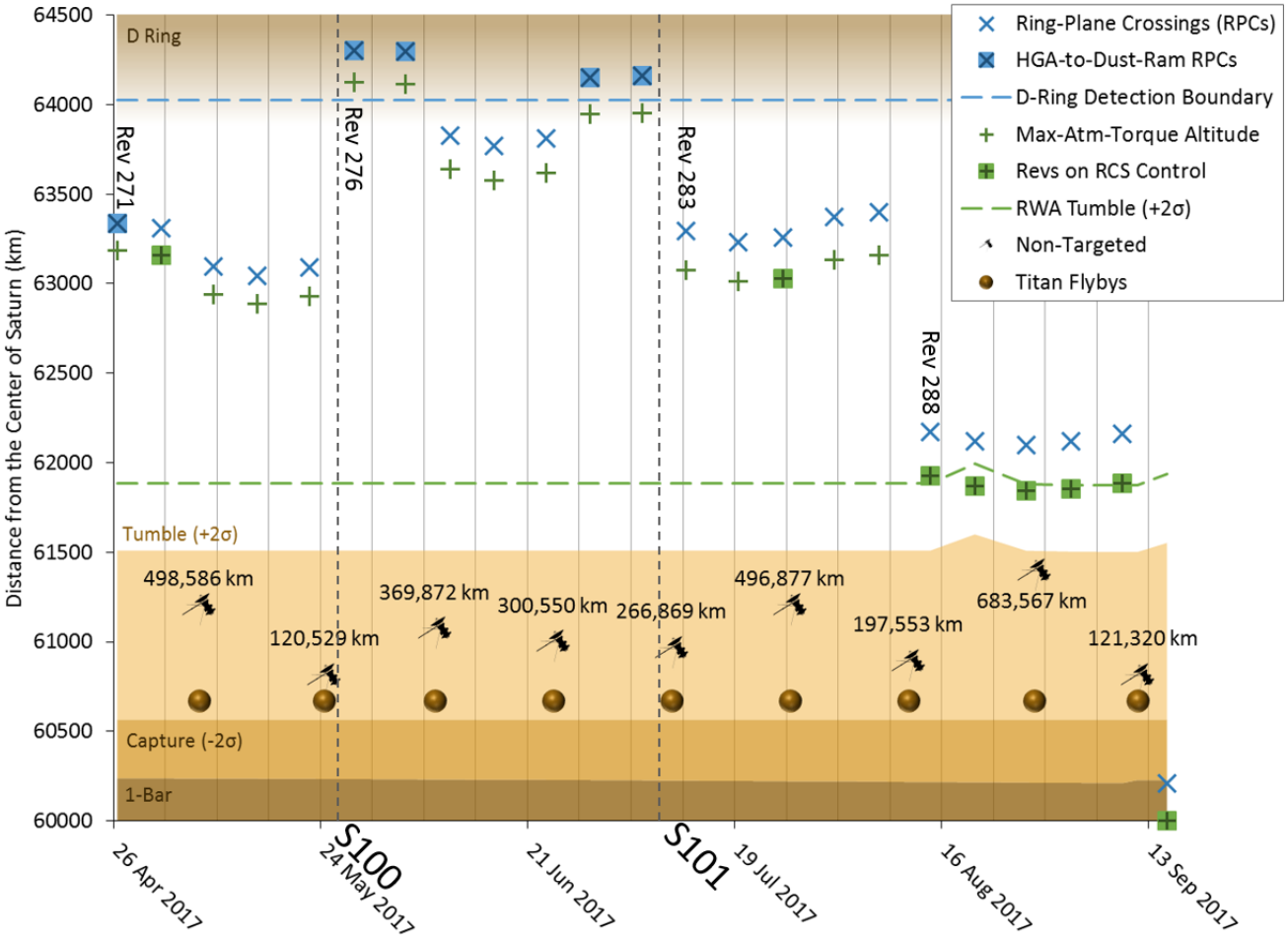

Figure 2: Variations in the altitudes of ring-plane crossings (blue) and points of maximum-atmospheric-torque (green) during the proximal orbits. The non-targeted Titan flyby distances that cause the variations are also shown (on a separate scale).

Zooming in on Figure 2 to show only the final five orbits, results in Figure 3, which shows that the final five orbits go progressively deeper into Saturn's atmosphere until Rev 290 and then start to climb back out again.

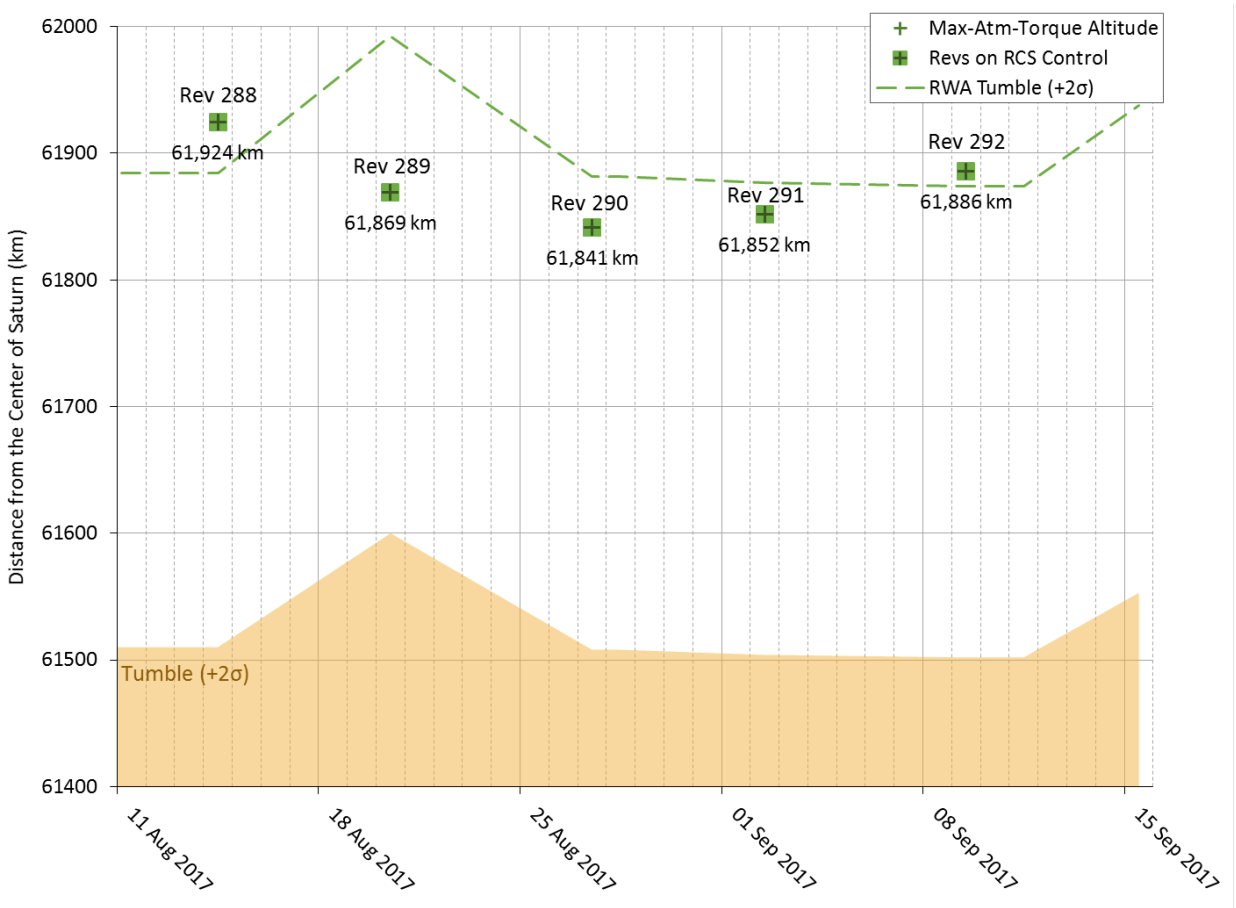

Figure 3: Maximum-atmospheric-torque altitudes of the final five proximal orbits.

Figure 3 also shows that there is a 300-400 km margin between the spacecraft altitudes and the 2σ tumble boundary. Back when these orbits were designed, this margin was only tens-of-kilometers; however, recent occultation data suggest that Saturn's atmosphere is contracting and with it, the tumble altitude. For additional detail, see reference document by T. Koskinen et al.

3.1.2 End of Mission

The Cassini Program End of Mission Scenario (D-96083) describes the final orbit of the Cassini mission in detail; however, a very brief summary is given here for reference.

The last non-targeted Titan flyby, 292TI, is just before apoapsis of Rev 293 and sets up the final plunge of the spacecraft into Saturn. The last 14.5 hours of the mission will have continuous DSN coverage with the final 3.5 hours providing a near-real-time downlink. Figure 4 shows the geometry of the final orbit with key events labeled.

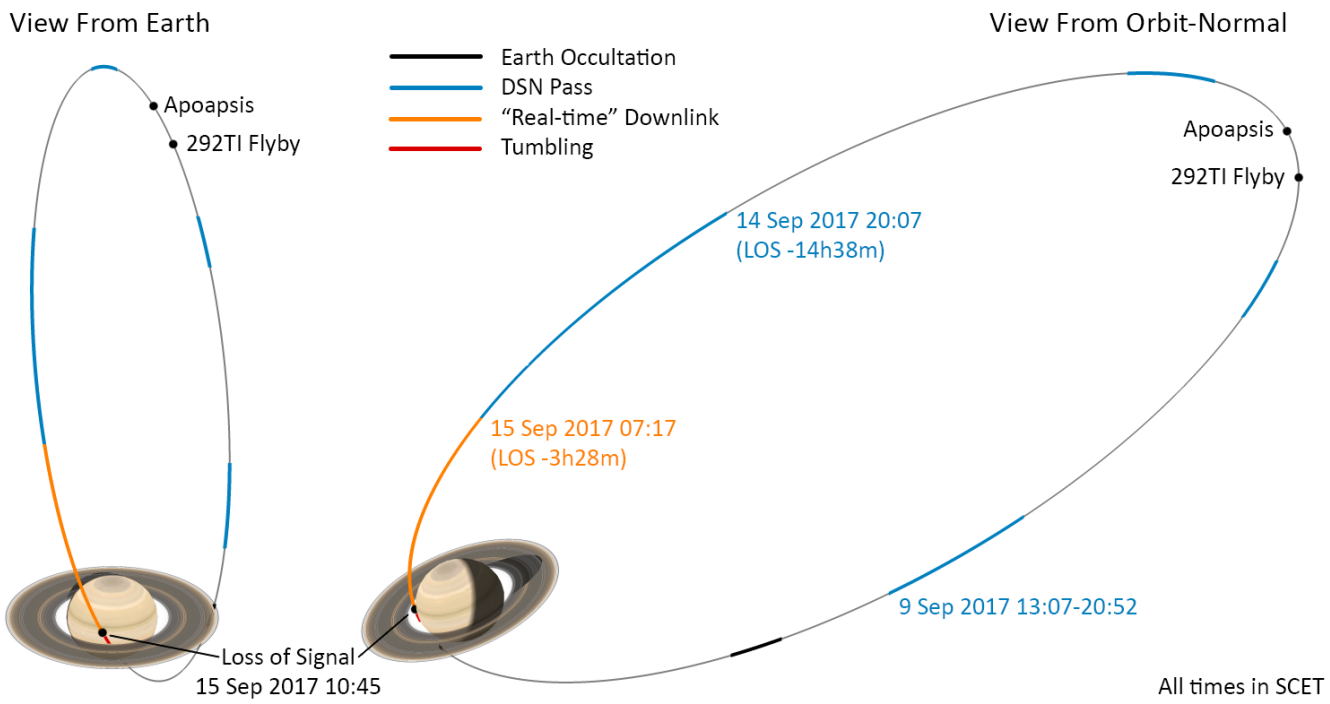

Figure 4: End-of-mission orbit geometry from Rev 292 periapsis to Saturn impact. On the left, is the view from Earth. On the right, is the view along the orbit normal. Times shown are in spacecraft event time (SCET).

The project is currently predicting loss of signal to occur on September 15, 2017 at 10:45 (SCET).

3.2 Saturn Thermosphere Model

The Saturn thermosphere model is a two-dimensional model of density that varies with radius and latitude. D. Strobel and T. Koskinen developed the model through analysis of ultraviolet solar and stellar occultations of Saturn's atmosphere. The Saturn Thermosphere Model presentation available on the Cassini mission-planning website documents the details of the model.

The model provides estimates for the atmospheric densities the spacecraft will fly through during the proximal orbits. When combined with the planned attitudes of the spacecraft, the Cassini flight-system-dynamics simulator (FSDS) can predict the peak RCS thruster duty cycles required to fight the atmospheric torque. In addition, the model, the planned attitudes, and the maximum RCS thruster torque combine to define a spacecraft tumble boundary, the radius at which the density is sufficient to overwhelm the RCS thrusters and cause the spacecraft to lose control authority. This boundary is shown as the light yellow area in Figure 2 and Figure 3.

The model was originally developed using occultation data from 2009. While not fully known at the time, these data corresponded to an expanded state of Saturn's thermosphere. As a result, the tumble boundary was high and margin was low; the project was concerned with flying through too much atmosphere, not too little. More recent occultation data suggest that not only has the expansion of the atmosphere stopped but that a contraction has likely begun.

The most recent version of the model (July 2015) now includes two number densities: one for the current (2015) state of the thermosphere and one for the predicted (2017) state. The current state is about two-thirds the

density of the 2009 values. The predicted state is half of that, about one-third the 2009 values. Now, spacecraft health and safety no longer seems to be at risk from the atmosphere, but the science teams are concerned the spacecraft may not be flying through enough atmosphere for instruments to adequately sample the density. More occultations are scheduled for 2016 and early 2017, which will give a better indication of the state the atmosphere will be in during the proximal orbits. If necessary, the thermosphere model will be updated to account for those occultation data.

3.3 Cassini Spacecraft

The two key subsystems of the Cassini spacecraft for this scenario are the attitude and articulation control subsystem (AACS) and the propulsion module subsystem (PMS). The AACS will serve as a density detector during the atmospheric transits of the final five proximal orbits, while the PMS will perform the pop-down maneuver.

3.3.1 Attitude and Articulation Control

The AACS has two methods for maintaining control authority of the spacecraft: the reaction wheel assemblies (RWAs) and the reaction control system (RCS) thrusters of the PMS. The majority of the time, the spacecraft is on RWA control, occasionally switching to RCS control for momentum management. The spacecraft uses the RCS most often for high-speed turns and during low Titan flybys, to maintain control authority against the large torque exerted by Titan's atmosphere. Similarly, the spacecraft will be on RCS control during Saturn atmospheric transits in the proximal orbits. The project will take advantage of this in order to estimate the density of Saturn's thermosphere, as the percentage of time the thrusters fire during a transit is directly proportional to the atmospheric torque, which is a function of density. Thruster duty cycle has the additional advantages of being relatively quick to downlink and calculate, as well as an accuracy of about ±1% (2σ).

3.3.2 Propulsion Module

The Cassini propulsion module subsystem is comprised of two separate propulsion systems: a bipropellant system with the main-engine assembly (MEA) and a monopropellant, reaction-control system (RCS). The locations of the main engines and RCS thruster pods are shown in Figure 5.

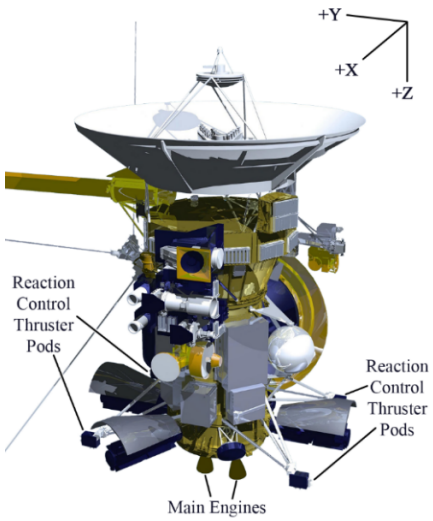

Figure 5: Cassini Spacecraft Thrusting Components

The Cassini spacecraft has two main engines and four RCS pods, each with four thrusters. Each RCS pod has two thrusters pointed along the +Z-axis and two thrusters pointed along either the +Y-axis or the –Y-axis depending on whether the pod is located on the +Y or –Y side of the X-Z plane. The thrusters are also separated into two

branches, A and B, each with four +Z thrusters, two +Y thrusters, and two –Y thrusters. The spacecraft currently uses the B branch due to premature degradation of some of the +Z thrusters in the A branch. While there is no indication of any B branch thruster degradation at this time, should it occur before the end of mission, the spacecraft could operate in a mixed branch mode, using thrusters from both the A and B branches.

The bipropellant system uses nitrogen tetroxide (NTO) as its oxidizer and monomethylhydrazine (MMH) as its fuel. The spacecraft uses the MEA solely for orbital trim maneuvers greater than 250 mm/s. The spacecraft uses the RCS for small translational maneuvers, attitude control, and spacecraft momentum management. The spacecraft can also use the RCS for larger translational maneuvers, the maximum being approximately 4 m/s in a single burn executed during a standard nine-hour pass.

3.4 Orbital Trim Maneuvers

An orbital trim maneuver (OTM) requires time for orbit determination, maneuver design, and execution windows (primary and back-up). A pop-down maneuver is most efficient when performed at apoapsis, which means the Navigation Team would have a little over three days to obtain tracking data, determine the orbit, and design the maneuver. The minimum duration required to perform the aforementioned tasks is shown in Table 1.

Table 1: Minimum durations for pop-down maneuver design.

Task	Minimum Duration
Obtain tracking data (two, daily, nine-hour passes)	33 hours
Orbit determination	3 hours
Maneuver design	3 hours
Navigation team review	1 hour
Total	**40 hours**

3.5 Propellant Levels

The amount of propellant predicted to be remaining in the spacecraft during the proximal orbits is of vital importance to feasibility of this scenario, as without sufficient propellant the spacecraft could not perform a pop-down maneuver.

As of the completion of OTM-456 (2 Aug 2016), there is just under a 7% chance of depleting the bipropellant before the end of the mission. However, even with the assumption that the spacecraft depleted the bipropellant at the end of that OTM, there is about 25 m/s of margin between the ΔV required to fly the remaining mission and the ΔV that the monopropellant system alone can provide. Depending on how long the bipropellant lasts, the hydrazine margin could grow to be as large as 28 m/s by the time of this scenario. In addition, the bipropellant mean margin is predicted to be 20 m/s during this scenario.

4 Events and Timeline

4.1 Detection of Low Density Atmosphere

As discussed in section 3.3.1, this scenario uses the AACS as a density detector. By analyzing the RCS thruster duty cycles during the atmospheric transits and comparing them to the predicted values, the project can infer the density of the atmosphere. Each atmospheric transit will result in two, peak, duty cycle estimates, one for the Y-thrusters and one for the Z-thrusters. The AACS team calculated the predicted peak Y and Z duty cycles for the atmospheric transits of the final five orbits. In addition, the Mission Planning team did an uncertainty analysis to determine the feasibility of distinguishing differences between predicted and actual duty cycles caused by the density of the atmosphere from those caused by other uncertainties. The sources of the other uncertainties that MP considered are navigation dispersions, spacecraft aerodynamics, mass properties, and RCS characteristics. The sources and their associated uncertainty values are shown in Table 2.

Table 2: Uncertainty sources of the duty cycle uncertainty analysis

Source	Unc. (1σ)	Units
Duty Cycle Calculation	0.5%	---
Navigation		
Radius	6.9	km
Velocity	10	m/s
Spacecraft		
Drag Coefficient	0.033	---
Drag Area	0.117	m^2
Center of Press.		
CPx	0.011	m
CPy	0.204	m
CPz	0.080	m
Center of Mass		
CMx	0.003	m
CMy	0.007	m
CMz	0.019	m
RCS Thrust	0.010	N

The results of the uncertainty analysis are shown in Figure 6. The peak duty cycles (Y and Z) for the final five orbits are shown with 2σ error bars from the sources identified above assuming a nominal atmosphere as predicted by the model, as well as 2σ-off-nominal atmospheres (high and low).

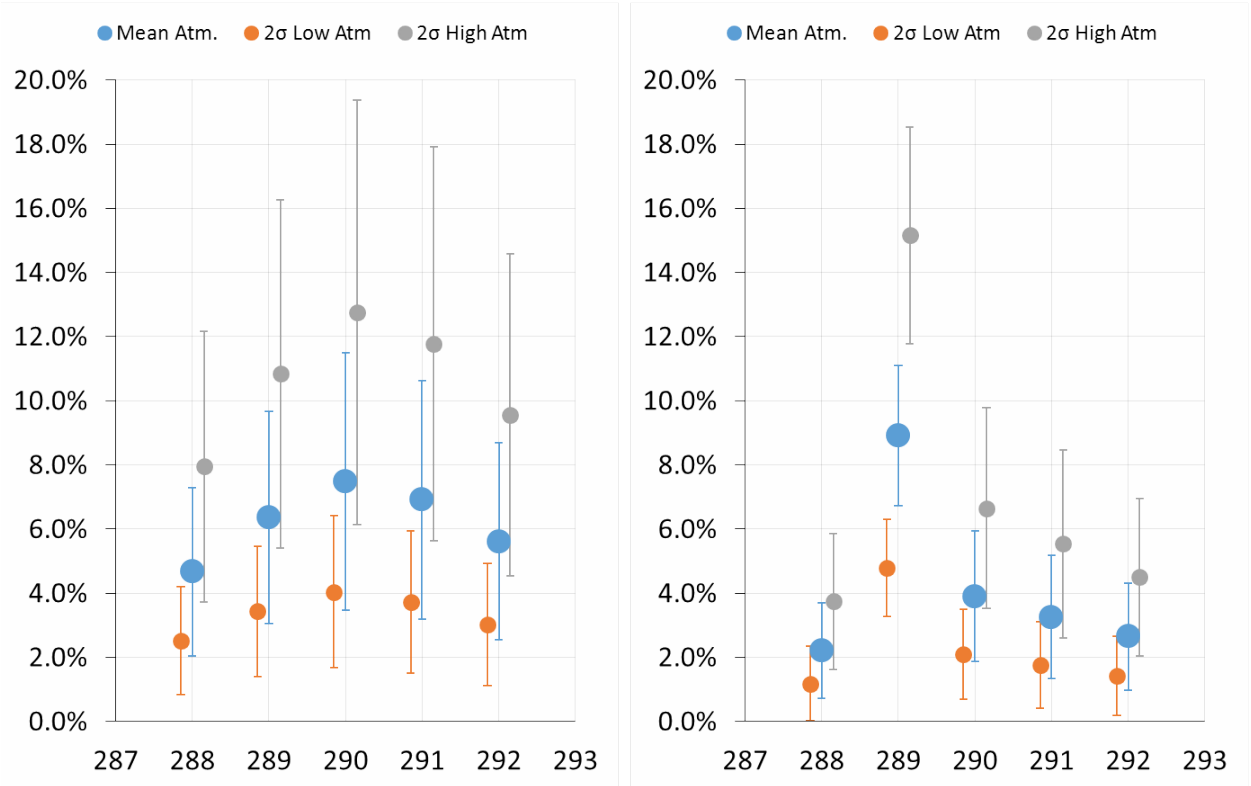

Figure 6: Predicted peak duty cycles of the RCS thrusters during the final five proximal orbits for nominal (blue) and off-nominal atmospheres, high (gray) and low (orange). Y duty cycle is on the left, Z is on the right.

Both plots in Figure 6 show that the predicted duty cycles, even for a 2σ high atmosphere, are well below the RCS limit. As a point of reference, the T57 Titan flyby, the lowest in the Cassini Equinox Mission, had a peak duty cycle of 69%. Therefore, the capacity exists for the spacecraft to dip deeper into the atmosphere. The plots also show that Z-thruster duty cycle is a slightly better indicator of atmospheric density than the Y-thruster duty cycle, though they both suffer from the uncertainties in Table 2 making it difficult to distinguish between atmospheric densities.

The Y-thruster duty cycles have significantly larger error bars due to the large uncertainty in the y-coordinate of the center of pressure. Looking back at Table 2, the y-coordinate of the center of pressure has an uncertainty that is nearly an order of magnitude larger than the other two coordinates. The Z-thruster duty cycles show less overlap between the nominal and 2σ-off-nominal atmospheres; however, Rev 289 is the only one with a distinct separation between them, a result of the planned attitude during that transit. Given these results, the spacecraft should not perform a pop-down maneuver until it has completed the Rev 289 transit, as that transit will give the best indication of the actual state of the atmosphere. In addition, collecting more data from subsequent transits before a pop-down would serve to further reduce the uncertainty in the atmospheric state.

4.2 Pop-down Maneuver Design

A pop-down maneuver performed near apoapsis will reduce both periapsis altitude and orbital period. Assuming the pop-down maneuver to be an instantaneous burn performed exactly at apoapsis, Figure 7 shows the change in periapsis and period resulting from a pop-down maneuver performed at the Rev 291 apoapsis.

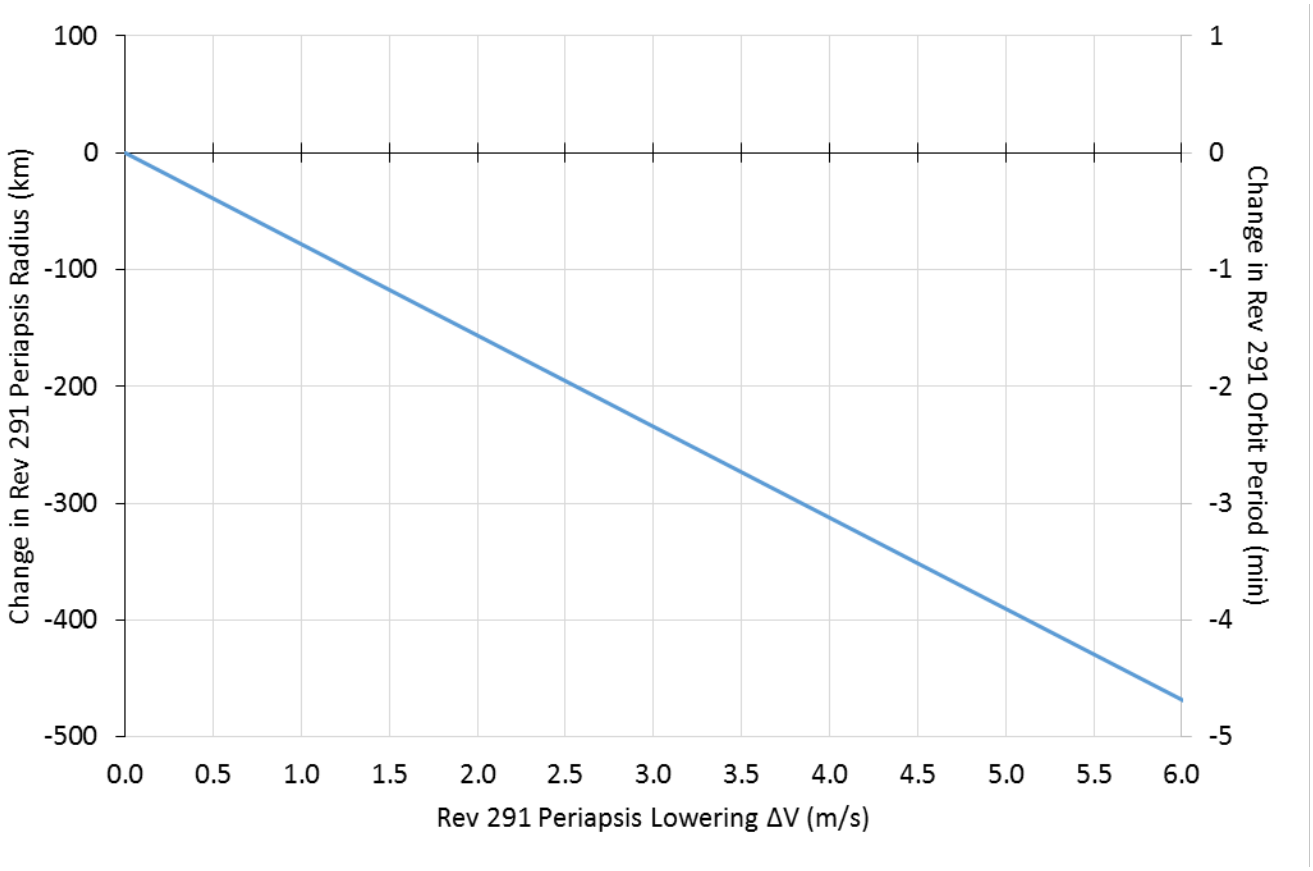

Figure 7: Effects of a pop-down maneuver on Rev 291 periapsis radius and orbit period.

Two constraints limit the magnitude of a pop-down maneuver: maximum burn time in a single nine-hour pass and maximum thruster duty cycle of subsequent, post-pop-down, atmospheric transits. The former requires the burn to be no larger than 4 m/s if performed with the RCS thrusters; the latter can be inherited from that used for Titan flyby designs, which is 70%. In order to see how much a pop-down maneuver could change the predicted peak duty cycle of a given transit, Rev 291 will again be used as an example. The ΔV required to achieve a given peak Y-thruster duty cycle during the Rev 291 atmospheric transit is plotted in Figure 8. At 0.0 m/s (no pop-down maneuver), the three lines have the same duty cycles as shown in the left plot of Figure 6, above. The duty cycle values at 4.0 m/s give the maximum peak duty cycle that could be achieved by performing a single pop-down maneuver with the RCS thrusters. For a nominal atmosphere, a single RCS maneuver could increase the peak duty cycle from 7% to 50%. Increasing the duty cycle to the 70% limit would require either another pop-down maneuver on RCS with an additional 0.6 m/s of ΔV, or using the main engine for the original pop-down in order to perform all 4.6 m/s in one burn.

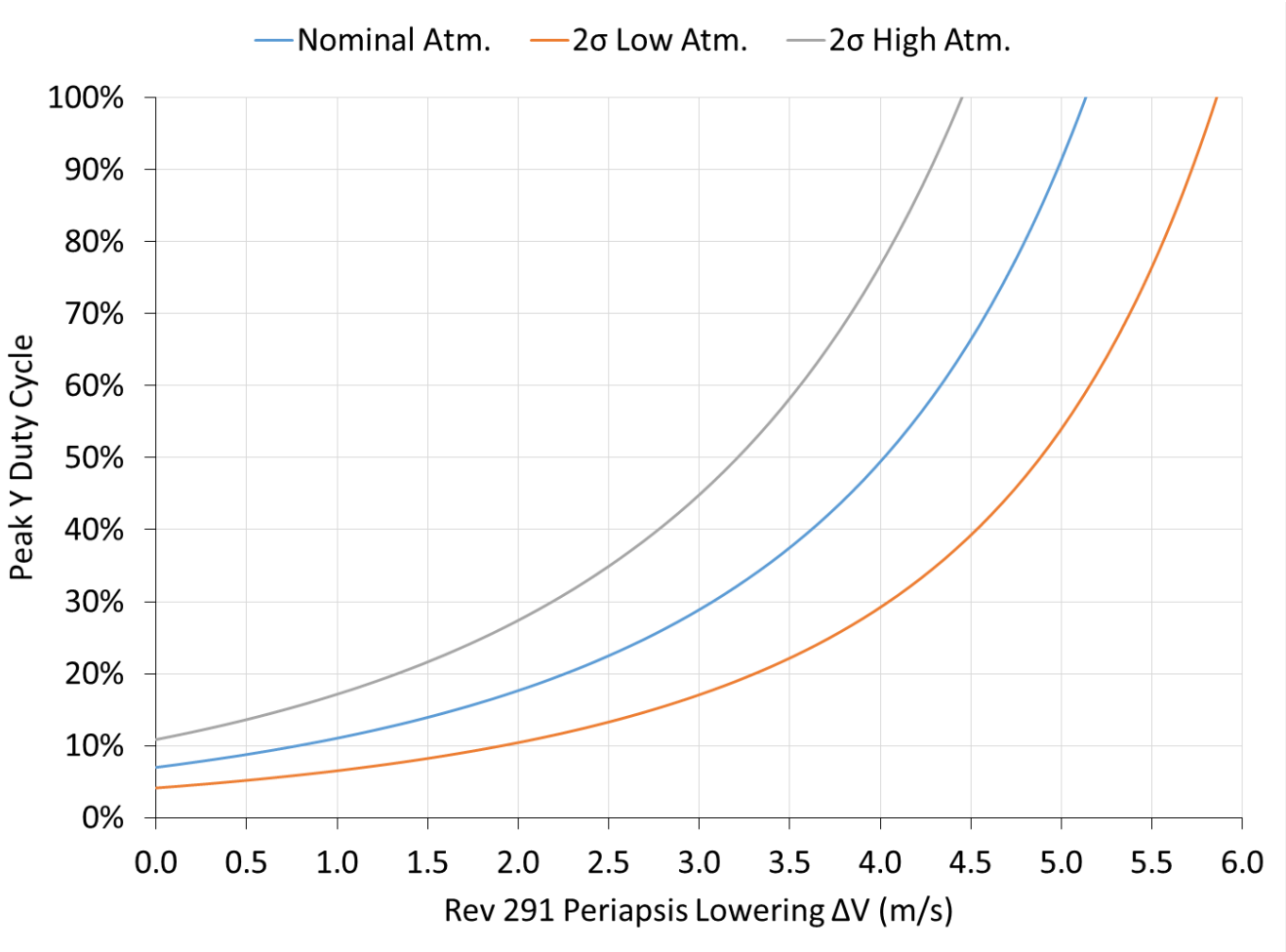

Figure 8: Peak Rev 291 Y-thruster duty cycle vs. ΔV for a pop-down maneuver performed at the Rev 291 apoapsis. Each line represents a different atmospheric state: nominal (blue), 2σ-high off nominal (gray), and 2σ-low off nominal (orange).

Figure 8 also helps alleviate concerns about the duty-cycle detection method not providing enough resolution to design a safe pop-down maneuver, as a 4.0 m/s burn is not enough to take even a 2σ-high atmosphere case beyond an 80% peak duty cycle. Moreover, the actual ΔV required to achieve the shown changes in duty cycle will be larger due to the inefficiencies introduced when removing the assumption of an instantaneous burn right at apoapsis.

4.3 Downstream Effects on the Trajectory

The primary effect of a pop-down maneuver on the trajectory is the lowering of all subsequent periapsis altitudes. In addition, the earlier the spacecraft performs a pop-down maneuver and the larger it is, the greater its effects will be on the downstream trajectory, specifically on the timing of events. Of particular concern are the subsequent periapsis passes as these are the periods with the highest priority science observations and most sensitivity to timing errors. Figure 9 shows the effects of a single, max-duration, 4.0 m/s pop-down maneuver performed at the Rev 290 apoapsis on the position of the spacecraft. The maneuver lowers the points of minimum altitude above the tumble boundary by about 300 km for revs 290-292.

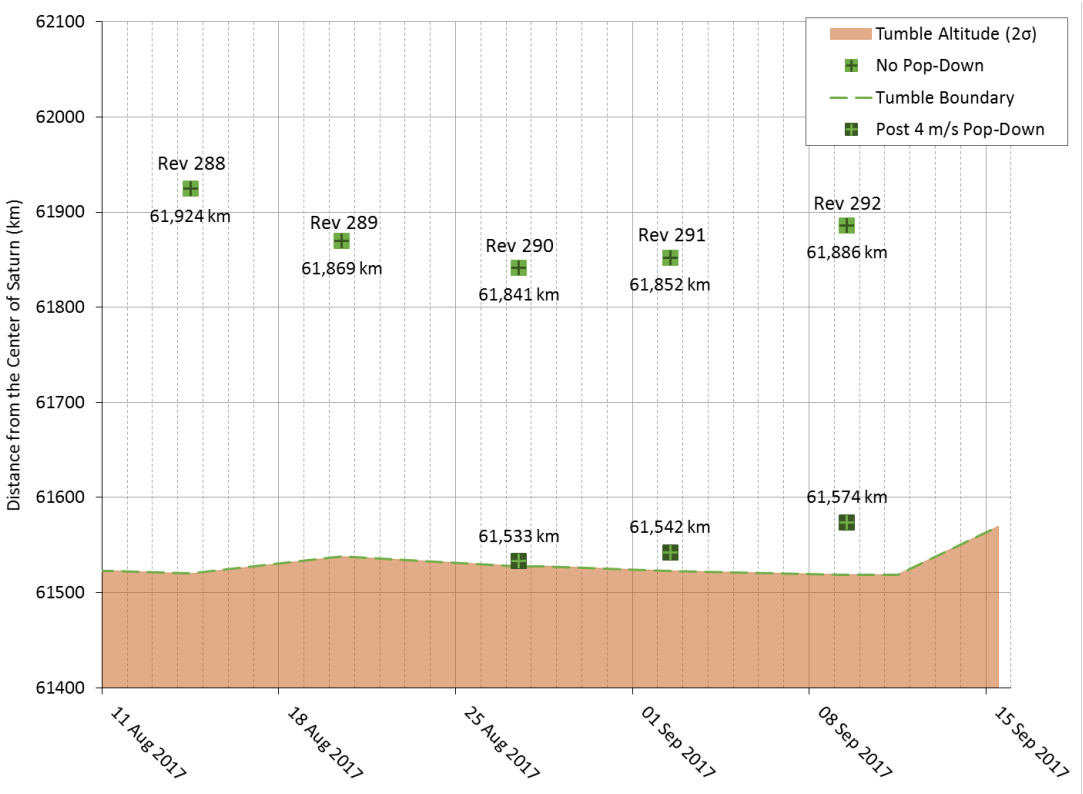

Figure 9: The points of minimum altitude above the tumble boundary for the nominal trajectory (light green) and for a trajectory with a 4 m/s pop-down maneuver at the Rev 290 apoapsis (dark green).

A pop-down maneuver not only reduces the periapsis radius of the trajectory but also the period of the orbits. The longer the spacecraft spends in a reduced-period orbit the more timing error accumulates with respect to the reference trajectory. Out at apoapsis, because the spacecraft is moving more slowly and targets of interest tend to be farther away, timing error tends to have less of an effect on observations. That said, the effect is likely not negligible and observations may be degraded. The periapsis designs are even more sensitive, which is why they have been padded with dead time on either side to allow them to be shifted in time to remove any error. Table 3 shows the shift in event times associated with a pop-down maneuver of various magnitudes performed at the Rev 290 apoapsis.

Table 3: Timing shifts resulting from a pop-down maneuver at the Rev 290 apoapsis. Times shown are mm:ss, and negative times indicate the shift is earlier than the nominal timing.

Rev		Nominal Timing	Rev 290 Pop-Down Maneuver Magnitude				
			0.5 m/s	1.0 m/s	2.0 m/s	3.0 m/s	4.0 m/s
290	Apoapsis	23 Aug 2017 20:56	-00:00	-00:00	-00:00	-00:00	-00:00
	Periapsis	27 Aug 2017 02:25	-00:12	-00:24	-00:49	-01:13	-01:37
291	Apoapsis	30 Aug 2017 07:54	-00:24	-00:49	-01:37	-02:26	-03:15
	Periapsis	02 Sep 2017 13:23	-00:37	-01:13	-02:26	-03:39	-04:52
292	Apoapsis	05 Sep 2017 18:54	-00:49	-01:37	-03:15	-04:52	-06:29
	Periapsis	09 Sep 2017 00:24	-01:01	-02:02	-04:03	-06:05	-08:07
293	Apoapsis	12 Sep 2017 05:44	-01:13	-02:25	-04:51	-07:18	-09:47
	Tumble	15 Sep 2017 10:52	-01:25	-02:50	-05:40	-08:31	-11:22

For the sake of conservatism, let us consider the instruments that are prime during the periapsis passages for revs 290-293 and their sensitivity to timing error assuming no ability to shift their designs. Working backwards, Rev 293 is the final plunge into Saturn. The spacecraft will be pointing the high-gain antenna towards Earth. As this is effectively an inertial target, it is unaffected by timing error. Revs 291 and 292 have INMS as the prime instrument. The entire reason for this scenario is to put INMS in as thick of an atmosphere as is safely possible, which means any timing error introduced by the pop-down is more than compensated for by the increase in science value. During Rev 290, RADAR is prime with the high-gain antenna pointed to Saturn. As the first opportunity for a pop-down maneuver is the Rev 290 apoapsis, the timing error will not accumulate to a large value by the Rev 290 periapsis (97 seconds for a 4 m/s burn), leaving the pointing design relatively unaffected. In addition, the scenario baseline is to wait until Rev 291 to do the pop-down, which would leave the Rev 290 periapsis completely unaffected.

4.4 Reference Timeline

The timeline for this scenario is highly dependent on the DSN pass schedule. The first pass after each atmospheric transit determines the earliest the spacecraft can downlink the RCS thruster data. The time between the second pass after each transit and the pass nearest apoapsis determines how long the navigation team will have to design the maneuver. The time between the pop-down pass and the last pass before periapsis determine how long the navigation team will have to determine the new orbit such that the science planning and sequencing team can send the commands to shift the pointing design by the necessary amount of time. Table 4 shows the planned DSN passes during the final five proximal orbits, in blue, along with the pre-integrated events (PIEs), in orange. Additional rows have been added to distinguish certain types of passes: candidate pop-down maneuver passes (red), post-transit-pre-maneuver passes (green), and post-maneuver-pre-transit passes (purple).

Table 4: Schedule of all DSN passes and pre-integrated events (PIEs) in the final five proximal orbits.

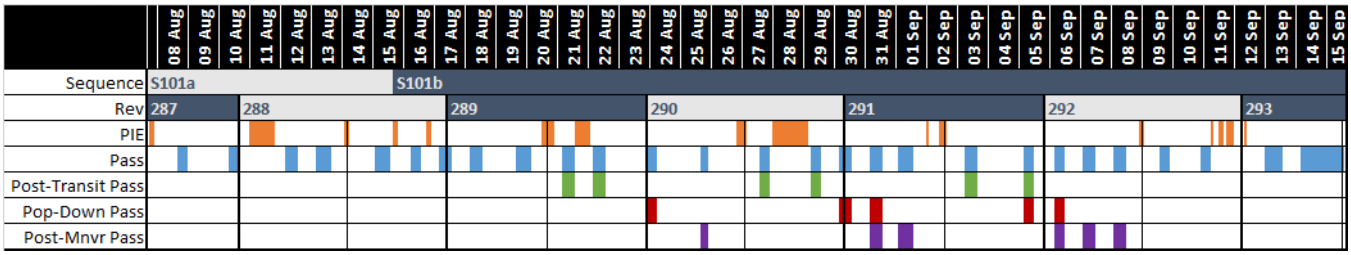

The red passes are those nearest to apoapsis, and the best candidates for pop-down maneuvers. Ideally, each apoapsis would have two passes straddling it, one on either side. This would provide prime and backup opportunities for the OTM with minimal losses in burn efficiency due to the shift off apoapsis. This only occurs at 291/292 opportunity. The 290/291 opportunity has a prime window right at apoapsis and a backup over a day later, which might not result in too great a loss of efficiency. The 289/290 opportunity has only one pass, with no good backup. The green passes are those required for designing the pop-down maneuver; the navigation team requires at least two nine-hour passes. Note that 291/292 opportunity can either meet this requirement or the previous requirement, but not both. The purple passes are those available for determining the new orbit and uplinking the associated timing shifts for subsequent periapsis pointing designs. Since the design value for the timing shift may be used, only one of these passes is required before the next periapsis. The 290/291 opportunity is the only one that meets all the tracking requirements for a pop-down maneuver; however, 291/292 opportunity can be done just without a back-up window for the OTM, which is acceptable given the optional nature of a pop-down.

In addition to meeting the tracking requirements, there needs to be enough time between the downlink of a transit's RCS thruster data to the prime maneuver window for:

- The AACS team to calculate the duty cycle
- The Project to make a decision on whether or not to perform a pop-down
- Mission Planning and Project Science to convert duty cycle to an appropriate navigation target altitude
- The navigation team to design the maneuver to the target altitude

From the last column in Table 5, there are over eight days between the time the Rev 289 thruster data is returned and the prime opportunity for the Rev 291 pop-down maneuver. The minimum amount of time available for the above activities is 32 hours, which would only happen should the project decide to perform the pop-down at Rev 290. Even then, MP would have 16 hours to calculate a target altitude and Nav would have 16 to design the maneuver.

Table 5: Date and time of key events with the duration from their completion to the start of the next pop-down maneuver pass.

Rev	Event	Date (SCET)	Time to Next Pop-Down
288	Periapsis	14 Aug 2017 04:26	-9d 17h
	RCS Downlink Complete	15 Aug 2017 13:40	-8d 8h
289	Periapsis	20 Aug 2017 15:27	-3d 6h
	RCS Downlink Complete	21 Aug 2017 12:54	-2d 8h
	OD Tracking Complete	22 Aug 2017 12:34	-1d 9h
290	Apoapsis	23 Aug 2017 20:56	-0d 0h
	Prime Pop-down Pass Start	**23 Aug 2017 21:24**	**---**
	Periapsis	27 Aug 2017 02:25	-3d 1h
	RCS Downlink Complete	27 Aug 2017 21:54	-2d 5h
	OD Tracking Complete	29 Aug 2017 13:23	-0d 14h
	Prime Pop-down Pass Start	**30 Aug 2017 02:58**	**---**
291	Apoapsis	30 Aug 2017 07:54	-5d 19h
	Periapsis	02 Sep 2017 13:23	-2d 13h
	RCS Downlink Complete	03 Sep 2017 15:38	-1d 11h
	OD Tracking Complete	03 Sep 2017 15:38	-1d 11h
	Prime Pop-down Pass Start	**05 Sep 2017 02:37**	**---**
292	Apoapsis	05 Sep 2017 18:54	+0d 16h

As there are no PIEs in the apoapsis regions of these orbits, the project could change the tracking schedule should the navigation team deem the above times inadequate to safely design and execute a pop-down maneuver.

5 Risks and Mitigations

The main risk of this scenario is performing a pop-down maneuver that takes the spacecraft too deep into the atmosphere causing a loss of control authority and spacecraft safing. The larger the size of a pop-down and the earlier it takes place in the final five orbits, the more the likelihood of this risk increases as the spacecraft would be jumping deeper into the atmosphere with less information. There are three main mitigations to this:

complete more transits before performing a maneuver, design the maneuvers to a peak duty cycle of 70% (TBD) for subsequent transits, and perform multiple maneuvers.

As was shown in Figure 6, using duty cycle to detect atmospheric state can be a challenge given the uncertainties involved. However, the more transits completed, the more duty-cycle data points will be available to help reduce the uncertainties and hone in on the actual state of the atmosphere. While Figure 6 shows that waiting for the Rev 289 transit data is practically a necessity, it also shows that waiting for subsequent transits has diminishing returns.

Limiting the magnitude of the pop-down maneuver to increase the peak duty cycles of subsequent transit to be well below 100% further mitigates the risk of going too deep. Using the state of the atmosphere determined by the transit duty cycles, the mission planning team would calculate a target altitude that would yield a peak duty cycle of 70% (TBD) during the remaining transits. This would leave 30% margin for other torques and the uncertainties in both the atmosphere and those listed in Table 2.

Performing multiple pop-down maneuvers not only has the benefit of allowing for the collection of more transit data between the maneuvers, but also, the additional transit data would be from deeper in the atmosphere. As can be seen in Figure 10, lowering altitude increases the separation in duty cycle values created by the off-nominal atmospheres. This means both the quantity and quality of the transit data would increase. Multiple maneuvers also allow the spacecraft to perform more than 4 m/s of total ΔV if using the RCS, increasing the range of reachable altitudes and further improving science value.

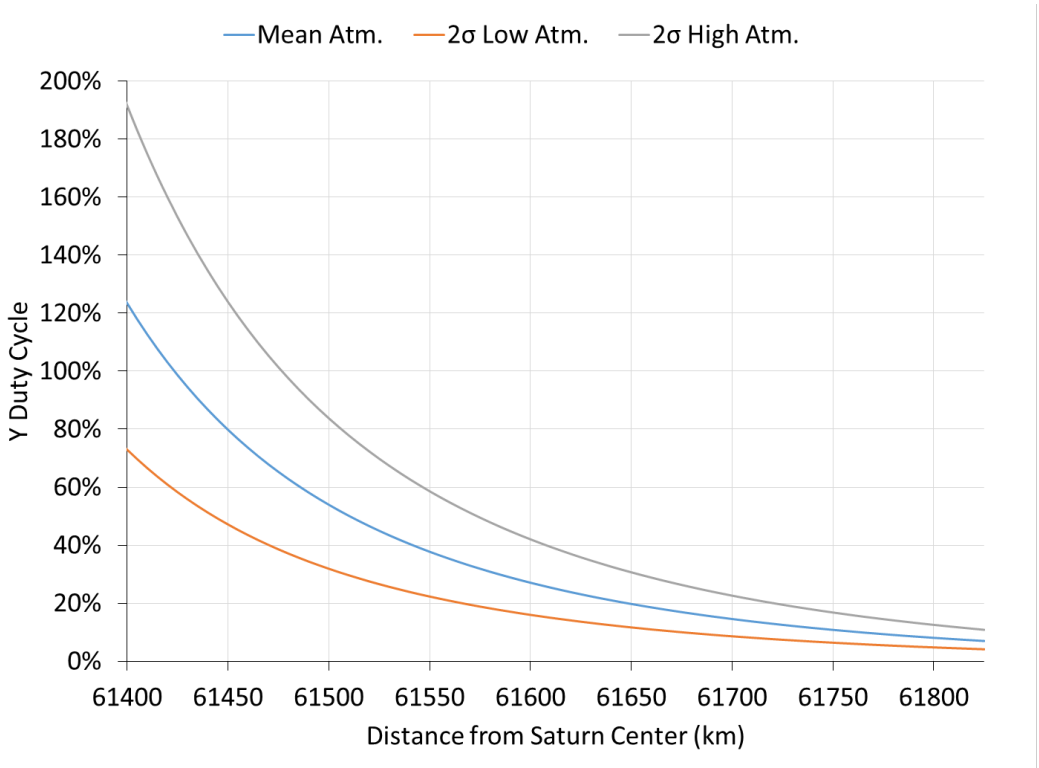

Figure 10: RCS Y-thruster peak duty cycle versus radial distance from Saturn's center.

6 Conclusion

6.1 Summary

Given the current thermosphere model, mission planning predicts that the maximum RCS thruster duty cycle during the final five proximal orbits will be less than 13% (2σ). This compares to the previous value of 71%, shifting the concern from spacecraft health-and-safety to science value. To that end, this document explores a "make-better" science scenario for modifying the Cassini spacecraft's trajectory to dip deeper into Saturn's atmosphere during the final five proximal orbits by performing one or more pop-down maneuvers near the orbits' apoapses.

The catch comes in accurately determining the state of the atmosphere in order to design a pop-down maneuver. Using RCS thruster duty cycles as a proxy for atmospheric state is a viable method, though not without its shortcomings. Multiple data points should be obtained from atmospheric transits before executing a pop-down in order to reduce uncertainties. In addition, designing the maneuver to a 70% (TBD) predicted peak duty cycle would ensure adequate margin for absorbing errors in the estimate of atmospheric state.

The current DSN passes provide only one opportunity for a pop-down maneuver that meets all tracking requirements, near the apoapsis of Rev 291. However, the opportunity near the apoapses of Rev 292 is also acceptable.

The priority placed on obtaining high-quality, in-situ atmospheric measurements combined with the fact that Titan flybys have been designed to 70% duty cycles suggests that lowering periapsis passages during the final five orbits is a viable option worth considering.

6.2 Open Issues, Concerns, Future Work

6.2.1 Choice of Propulsion System

Propulsion System (Propellant)	Pros	Cons
Main Engine Assembly (NTO-MMH)	• Can perform burns >4 m/s • May inadvertently yield a burn-to-depletion	• May be depleted • May inadvertently yield a burn-to-depletion
Reaction Control System (Hydrazine)	• Very likely to have sufficient propellant (>20m/s margin) • Will not deplete mid-burn	• Could cause catastrophic failure of an RCS thruster

6.2.2 Duty Cycle Limits

Need to finalize the design limits on the duty cycle for the target altitude calculation. Currently suggested at 70% for the mean predicted peak duty cycle, but may also need +2σ predicted peak duty cycle limit, 90%. These may need to be more conservative like 50% mean, 75% +2σ.

6.2.3 Thermosphere Model Update

More occultations of Saturn's atmosphere are planned in 2016 and early 2017. The thermosphere model and duty cycle predicts will be updated as necessary and this scenario modified accordingly.

Jet Propulsion Laboratory

Interoffice Memorandum
IOM xxx-xx-xxx
February 2, 2011

To: The Cassini Project

From: The Saturn Atmospheric Modeling Working Group (SAMWG)

Subject: The "Shape" of Saturn

Distribution: J.B. Jones, D. Roth, E.A. Manor-Chapman, D.A. Seal, K.A. Magee, K. Weld

Abstract

We determine the location of the 100 mbar and 1 bar pressure surfaces on Saturn. The pressure surfaces are determined by the gravitational moments, the rotation rate, and the zonal winds in the appropriate frame of reference. These pressure surfaces can differ by up to 130 km from those modeled with the oblate spheroids currently being used to describe these surfaces. We provide equations for both of the above listed pressure levels in the form of Legendre polynomial expansions, which give the radius of the surface as a function of geocentric latitude. Tables for these pressure surfaces are also provided. This work is expected to impact folk whose analyses are dependent on the precise knowledge of the "surface" of Saturn, e.g. for determining Constraint Monitor Table (CMT) limits related to the boresight to Sun flight rules and for determining atmospheric mass density profiles.

Introduction

As with any gas giant or star, the shape of Saturn is a somewhat nebulous concept due to the lack of a hard physical surface. The question is very much tied to questions about the location of specific pressure levels and the location of where the atmosphere becomes opaque to visible wavelengths. Such information is often difficult to ascertain, requiring a combination of numerous occultations, gravity and wind measurements, and assumptions of the basic fluid properties of their atmospheres. Furthermore, they can often vary with time, season, local wind speeds, and the composition of the atmosphere. Nevertheless, it is still important to place the best constraints on the shape as is possible. For Saturn, we fortunately have the orbiting Cassini spacecraft, which can provide a large number of the observations required for constraining this particular problem.

This work was originally motivated by the necessity to protect the optical remote sensing (ORS) instruments from looking too closely at the solar disk (which subtends ~0.05576 degrees at Saturn) during a solar occultation. Several of Cassini's instruments provide cones of avoidance that must not be compromised for health and safety reasons. Often, though, these same instruments wish to observe the unlit side of the planet at high phase for ultraviolet and infrared dayglow, to searching for lightning flashes, and to characterize the atmospheric haze particles. Thus, there is a need for accurate timing for CMT management. An additional motivation for this work is for the improvement of the atmospheric mass density profiles provided to the Cassini Project, which are then used for the planning and assessment of Cassini's Proximal Orbits.

The Oblate Spheroid

To first order, the shape of a giant planet is usually described with an oblate spheroid uniquely specified by an equatorial and polar radius (note that this is sometimes referred to the NAIF ellipsoid in spacecraft navigation circles). The "surfaces" typically used are those of the 1 bar (R_e=60268 km, R_p=54364 km) or 100 mbar (R_e=60330 km, R_p=54438 km)[1] pressure surfaces. As such, the shape can be described with the following functional form:

$$\frac{1}{r(\theta)^2} = \frac{\cos^2\theta}{r_p^2} + \frac{\sin^2\theta}{r_e^2}, \quad (1)$$

where θ is the co-latitude (=π/2-λ). Rearranging, we obtain

$$r(\theta) = r_e \frac{(1-f)}{\sqrt[2]{1-(2f-f^2)\sin^2\theta}} = r_e\left[1 - \frac{f}{3} - f\frac{2}{3}P_2(\theta) - \frac{3}{8}f^2\sin^2 2\theta + \cdots\right], \quad (2)$$

where f is the dynamical oblateness which is related to both the J_2 gravitational moment and the rotation rate, ω, and is given by

$$f = 1 - \frac{r_p}{r_e} \approx \frac{3}{2}J_2 + \frac{1}{2}\frac{\omega^2 r_e^2 r_p}{GM}. \quad (3)$$

The last relation is obtained by equating the Legendre polynomial expansion of the oblate spheroid to the first order Legendre polynomial expansion derived from the exact gravitational potential theory, which is detailed below. As such, this is an approximation for the true shape of the body and, as illustrated below, can result in large enough errors for problems requiring knowledge of the precise location of particular pressure levels in the atmosphere.

Potential Theory and the Theory of Figures

Level surfaces can be determined by using the Theory of Equilibrium Figures (e.g. Jardetzky, 2005). In this theory, surfaces of constant gravitational potential are determined by using information provided by the gravitational moments (measured by radio science gravity determinations) and the rotation rate of the planet. The gravitational potential is solved self-consistently by assuming that hydrostatic equilibrium is applicable and that the atmosphere is barotropic. The equations governing the fluid body are given by

$$\rho\nabla\left(\Phi_{gravity} + \Phi_{rotation}\right) = -\nabla p, \quad (4a)$$

$$\rho = \rho(p), \quad (4b)$$

and

$$\Phi_{gravity} = -\oint G\frac{\rho(\vec{r}')}{|\vec{r}'-\vec{r}|}d\vec{r}' = -\frac{GM}{r}\left[\sum_{l=0}^{N}\left(\frac{a}{r}\right)^l J_l(a)P_l(\cos\theta)\right], \quad (4c)$$

θ is the co-latitude. The simplest tractable solutions involve the assumption that the rotation of the body is constant (no differential rotation), i.e.

$$\Phi_{rotation} = -\frac{1}{2}\omega_0^2 r^2\sin^2\theta = -\frac{\omega_0^2 r^2}{3}[1 - P_2(\cos\theta)], \quad (5)$$

[Note, however, that a potential can also be defined if the rotation rate is a function solely of the distance from the axis of rotation, i.e. $\omega = \omega(r\sin\theta)$, (Trubitsyn, *et al.*, 1976).]

The Theory of Equilibrium Figures finds the equation that describes the constant potential surface of the body in question (Zharkov and Trubitsyn, 1976 and Efimov, *et al.*, 1977), i.e.

---

[1] It should be noted here that this value of the equatorial radius of the 100 mbar level is from an older Pioneer determination. The value determined by Lindal, *et al.*, (1985) from Voyager measurements is 60367 km.

$$r(\cos\theta) = s[1 + \sum_{n=1}^{\infty} s_{2n}(s) P_{2n}(\cos\theta)]. \quad (6)$$

In practice, one works to find a solution for the s_{2n} up to order N (=5) which best approximates this surface. In general, the s_{2n} will be functions of the gravitational moments and the rotation rate of the body. The values for these parameters for using the gravitational moments of Jacobson, *et al.*, (2006) and both of the Voyager and Anderson & Schubert (2007) rotation rates can be found in the appendix. Further, to improve upon that *N*th order solution, we apply several Newton iterations steps to reduce the truncation error and, thus, ensure that we are indeed on the gravitational potential surface.

Figures 1a and 1b illustrates the differences between the reference ellipsoid and the level surfaces for the Voyager rotation rates. Results provided by RSS/CIRS from the analysis of radio occultations are shown. Figures 2a and 2b illustrate the differences using the Anderson and Schubert (2007) rotation rates. It should be noted that the deviation from the reference ellipsoid is maximal at 45ºN and 45ºS (primarily due to a substantial J_4 term). Errors up to 130 km can be observed. *What should be obvious is that the largest "uncertainty" in the location of a particular geopotential surface is due to the use of a simple oblate spheroid to model the actual geopotential surface.* What is also apparent is that the calculated geopotential is very dependent on the chosen rotation rate (the latter being quite arbitrary at this time). As we show below, zonal winds will introduce additional perturbations from the geopotential surface and nicely accounts for the differences between the geopotential surface and a given pressure level surface.

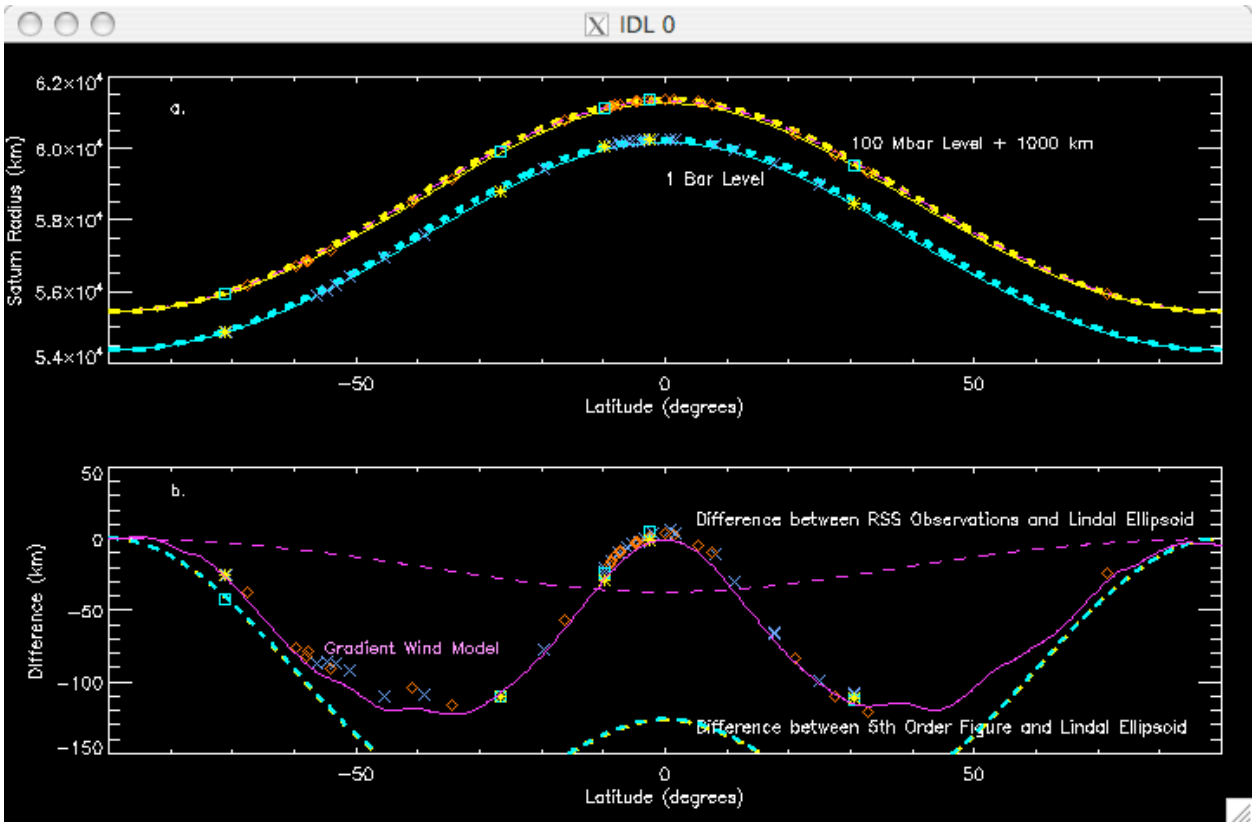

Figure 1a: Shape of Saturn and the Location of the 100 mbar and 1 bar Levels using the Voyager rotation rate. NAIF Reference Ellipsoid for 100 mbar and 1 bar surfaces (yellow dashed and blue dashed curves, respectively). 5th-Order Figure for 100 mbar and 1 bar surfaces (yellow solid and blue solid curves, respectively). Orange ◊ represent the preliminary results for 100 mbar from RSS/CIRS analysis (Flaser, private communication). Green X represent the preliminary results for 1 bar from RSS/CIRS analysis (Flaser, private communication). Voyager data points are shown by the □ and *. In all cases, the 100 mbar curves have been offset by 1000 km to illustrate the differences.

Figure 1b: *Difference* between the Shape of Saturn and the reference ellipsoid for the 100 mbar and 1 bar Levels. The difference for the 1 bar level is represented by the dashed blue curve. The difference for the 100 mbar level is represented by the dashed yellow curve. The orange ◊ represent the preliminary results for 100 mbar from RSS/CIRS analysis (Flaser, private communication). The green X represent the preliminary results for 1 bar from RSS/CIRS analysis (Flaser, private communication). Voyager data points are shown by the □ and *. The purple dashed curve represents the difference of the NAIF ellipsoid and the Lindal ellipsoid for the 100 mbar level.

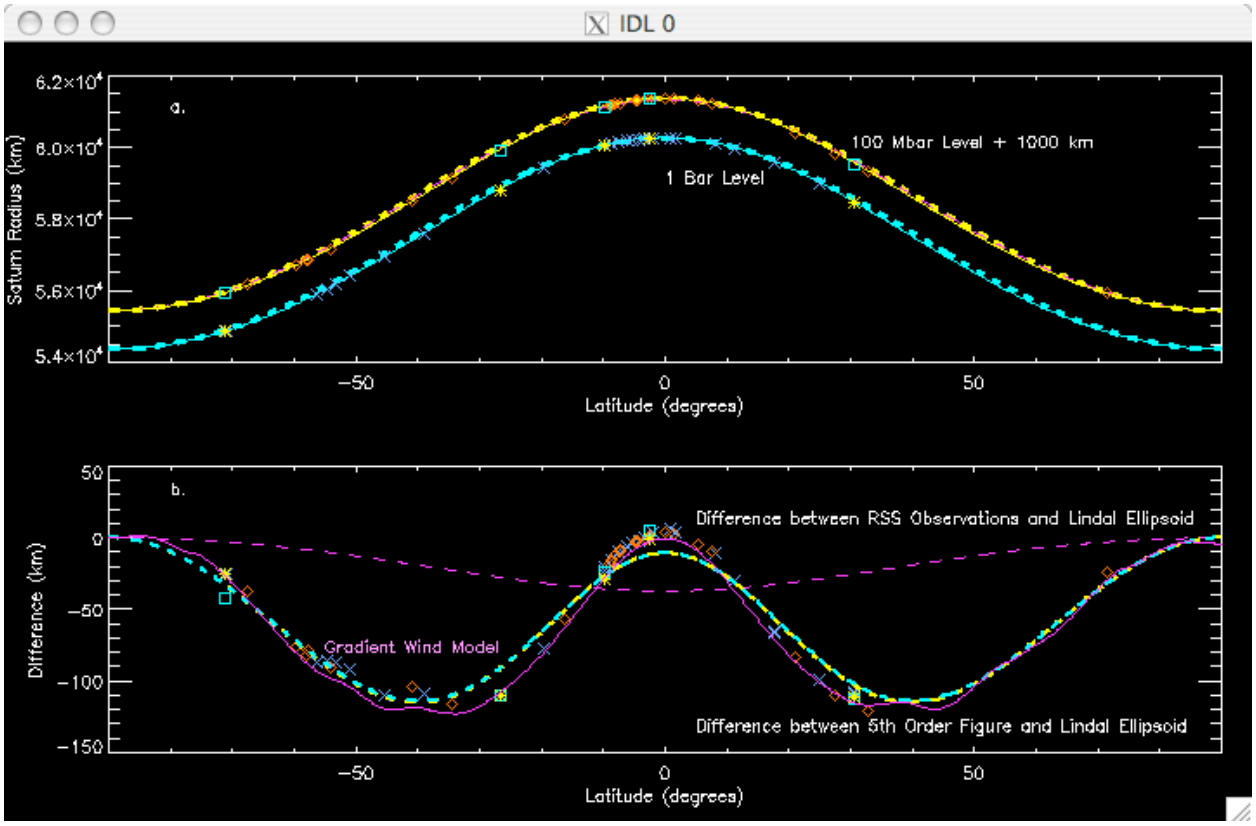

Figure 2a: Shape of Saturn and the Location of the 100 mbar and 1 bar Levels using the Anderson and Schubert (2007) rotation rate. NAIF Reference Ellipsoid for 100 mbar and 1 bar surfaces (yellow dashed and blue dashed curves, respectively). 5th-Order Figure for 100 mbar and 1 bar surfaces (yellow solid and blue solid curves, respectively). Orange ◊ represent the preliminary results for 100 mbar from RSS/CIRS analysis (Flaser, private communication). Green X represent the preliminary results for 1 bar from RSS/CIRS analysis (Flaser, private communication). In all cases, the 100 mbar curves have been offset by 1000 km to illustrate the differences.

Figure 2b: *Difference* between the Shape of Saturn and the reference ellipsoid for the 100 mbar and 1 bar Levels. The difference for the 1 bar level is represented by the solid blue curve. The difference for the 100 mbar level is represented by the solid yellow curve. The orange ◊ represent the preliminary results for 100 mbar from RSS/CIRS analysis (Flaser, private communication). The green X represent the preliminary results for 1 bar from RSS/CIRS analysis (Flaser, private communication). Voyager data points are shown by the □ and *. The purple dashed curve represents the difference of the NAIF ellipsoid and the Lindal ellipsoid for the 100 mbar level.

Zonal Winds

Following Ingersoll (SAMWG, 2010) and Lindal, *et al.* (1985), we determined the degree to which zonal winds assumed to be in geostrophic/cyclostrophic balance can cause deviations of a pressure level surface from a given geopotential surface. The basic equation (derived using the meridional momentum equation with the assumption that zonal winds dominate and modified to account for oblateness) is

$$\frac{\cos(\varphi_g - \varphi_c)}{r} \frac{\partial \Phi_{gravity} + \Phi_{rotation}}{\partial \varphi_c} = -\left(\frac{u^2}{r \cos \varphi_c} + 2\Omega u\right) \sin \varphi_g \,, \quad (7)$$

This equation is integrated along the pressure surface, thus giving the deviation from the constant geopotential surface. Once the perturbed potentials are determined, the radial location of the

pressure surface is determined by Newtonian iteration beginning with the fifth-order solution derived above. The resulting pressure surface can then be fit to a Legendre series expansion similar to that in equation (6). The results using this approach are given in Equations 8a, 8b, 9a, and 9b and are shown in Figures 3b and 4b. We note that this approach can be shown to be invariant to the rotation rate.

The Legendre expansion representing the 1 bar and 100 mbar surfaces (assuming the Voyager rates) are, respectively:

$$r(\cos\theta) \approx s[1 + \sum_{n=1}^{10} s_n(s) P_n(\cos\theta)] \quad (8a)$$

$$s = 58113.501 \quad (8b)$$
$$s_1 = 1.8444684x10^{-5}$$
$$s_2 = -0.069578323$$
$$s_3 = -3.0122526x10^{-5}$$
$$s_4 = 0.0056924209$$
$$s_5 = -5.7401771x10^{-5}$$
$$s_6 = -0.00075962418$$
$$s_7 = 1.2933112x10^{-5}$$
$$s_8 = 0.00034638233$$
$$s_9 = 1.2565650x10^{-5}$$
$$s_{10} = -0.00021321543$$

and

$$r(\cos\theta) \approx s[1 + \sum_{n=1}^{10} s_n(s) P_n(\cos\theta)] \quad (9a)$$

$$s = 58193.787 \quad (9b)$$
$$s_1 = 1.8511821x10^{-5}$$
$$s_2 = -0.069603096$$
$$s_3 = -3.0201519x10^{-5}$$
$$s_4 = 0.0056999799$$
$$s_5 = -5.7573189x10^{-5}$$
$$s_6 = -0.00076190019$$
$$s_7 = 1.2991131x10^{-5}$$
$$s_8 = 0.00034766766$$
$$s_9 = 1.2584999x10^{-5}$$
$$s_{10} = -0.00021399433$$

We also note here that a parallel analysis of the RSS/CIRS data by Flaser, *et al.* (private communication) incorporate zonal winds by determining the absolute rotation rate (rotation of the planet + zonal winds) and assuming that this rotation rate adheres to $\omega = \omega(r \sin\theta)$ in Equation 5, thus guaranteeing the existence of a centrifugal potential. The potential and levels surfaces are then determined computationally. Their analysis yields very similar results to those presented here due to the assumptions inherent in both approaches.

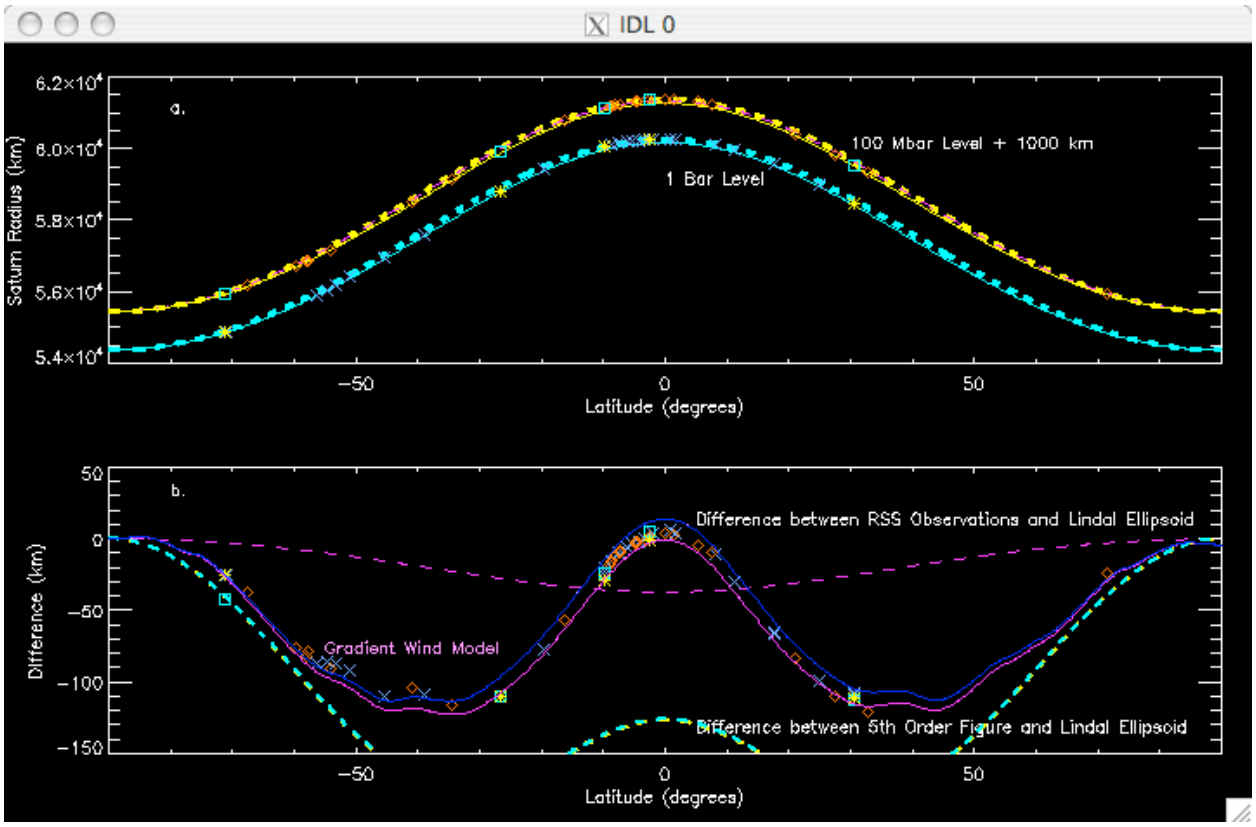

Figure 3a: Same as Figure 1a.

Figure 3b: The effect of winds (in the Voyager reference frame) are illustrated by the solid blue and solid purple curves. Zonal winds perturb airflow causing the pressure surface to differ from the potential surface.

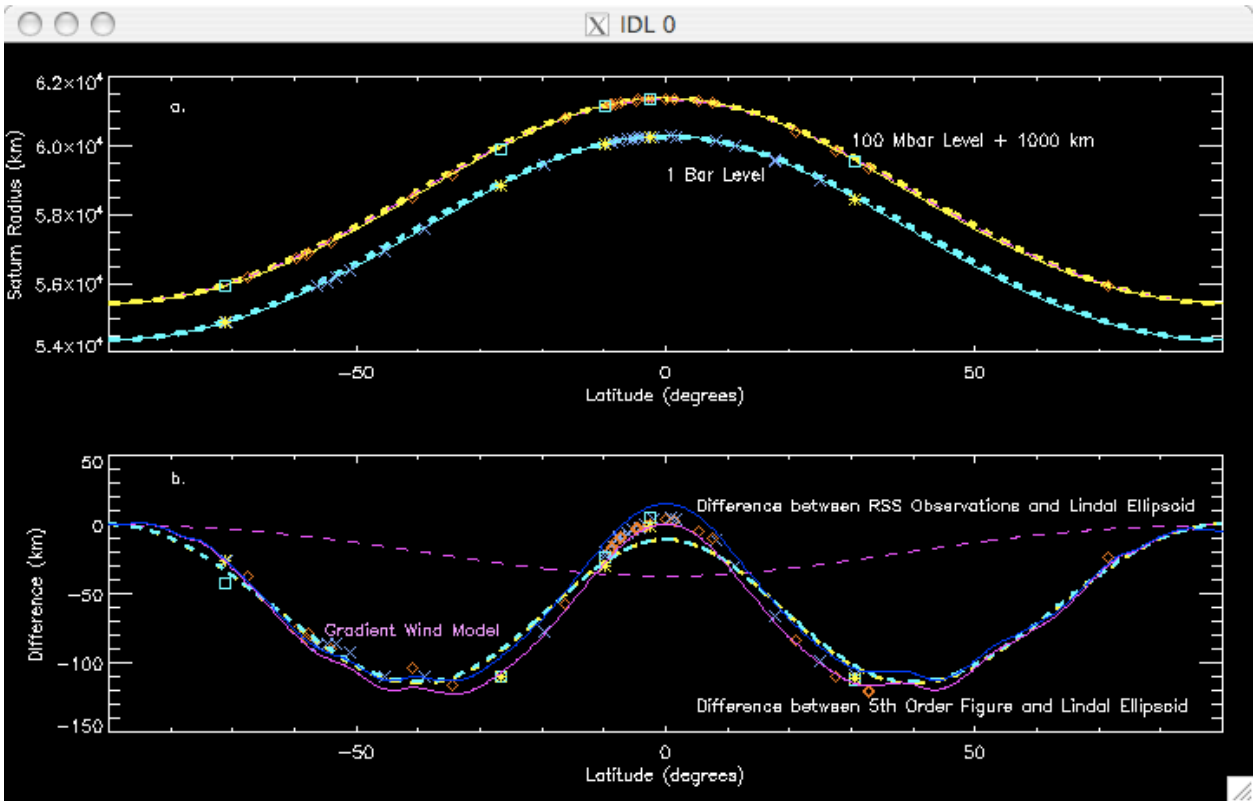

Figure 4a: Same as Figure 2a.

Figure 4b: The effect of winds (in the Anderson and Schubert (2007) reference frame) are illustrated by the solid blue and solid purple curves. Zonal winds perturb airflow causing the pressure surface to differ from the potential surface.

SAMWG Recommendation

In cases where the knowledge of the "shape of Saturn" is critical, the SAMWG recommends that the Project make use of the results of the higher-order theory presented in this document, i.e. equations (8a) and (8b) for the 1 bar pressure level and equations (9a) and (9b) for the 100 mbar pressure levels. A table of radius versus latitude can be provided.

Impacts

This work will directly affect the determination of the "safe-light levels" associated with the boresight for Sun flight rules (memo forthcoming), where improved modeling of the above pressure surfaces will improve timing associated CMT commanding. These calculations are typically conducted by MP and NAV. It will also impact the location of pressure levels in the upper atmosphere where it is important to model the tumbling altitude correctly. To the author's knowledge, there are no known impacts on other software used by Cassini.

References

Anderson, J.D. and G. Schubert, 2007. Saturn's Gravitational Field, Internal Rotation, and Interior Structure. *Science*, **317**, 1384-1387.

Efimov, A.B., V.N. Zharkov, V.P. Trubitsyn, and A.M. Bobrov, 1977. Figure parameters and gravitational moments of Jupiter and Saturn. *Sov. Astron.*, **21**, 635-640.

Jacobson, R.A., P.G. Antresian, J.J. Bordi, K.E. Criddle, R. Ionasescu, J.B. Jones, R.A. Mackenzie, M.C. Meek, D. Parcher, F.J. Pelletier, W.M. Owen, Jr., D.C. Roth, I.M. Roundhill, and J.R. Stauch, 2006. The Gravity Field of the Saturnian System from Satellite Observations and Spacecraft Tracking Data. *Astronom. J.*, **132**, 2520-2526.

Jardetzky, W.S., 2005. Theories of Figures of Celestial Bodies. Dover Publications, Inc., Mineola, New York.

Lindal, G.F., D.N. Sweetnam, and V.R. Eshleman, 1985. The atmosphere of Saturn - an analysis of the Voyager radio occultation measurements. *Astronom. J.*, 90, 1136-1146.

Trubitsyn, V.P., P.P. Vasil'ev, and A.B. Efimov, 1976. Gravitational fields and figures of differentially rotating planets. *Sov. Astron.*, **20**, 724-729.

Zharkov, V.N. and V.P. Trubitsyn, 1976. Fifth-approximation system of equations for the theory of figure. *Sov. Astron.*, **19**, 366-372.

Appendix: Gravitational Potential Surfaces

Using the Voyager rotation rate of 10h 39m 22.4s (ref???), the first five moments are for 1 bar and 100m bar are, respectively:

$$r(\cos\theta) \approx s[1 + \sum_{n=1}^{5} s_{2n}(s) P_{2n}(\cos\theta)] \text{ (A1a)}$$
$$s = 58115.075 \text{ (A1b)}$$
$$s_0 = -0.00093299054$$
$$s_2 = -0.068370275$$
$$s_4 = 0.0050883419$$
$$s_6 = -0.00036107985$$
$$s_8 = 3.3043764x10^{-5}$$
$$s_{10} = 0.0$$

and

$$r(\cos\theta) \approx s[1 + \sum_{n=1}^{5} s_{2n}(s) P_{2n}(\cos\theta)] \text{ (A2a)}$$
$$s = 58204.012 \text{ (A2b)}$$
$$s_0 = -0.00093810893$$
$$s_2 = -0.068557100$$
$$s_4 = 0.0051208159$$
$$s_6 = -0.00036495593$$
$$s_8 = 3.351783x10^{-5}$$
$$s_{10} = 0.0$$

Using a rotation period of 10h 32m 35s (Anderson and Schubert, 2007), the fifth-order theory of results in for the 1 bar surface:

$$r(\cos\theta) \approx s[1 + \sum_{n=1}^{5} s_{2n}(s) P_{2n}(\cos\theta)] \text{ (A3a)}$$
$$s = 58187.704 \text{ (A3b)}$$
$$s_0 = -0.00096931749$$
$$s_2 = -0.069686144$$
$$s_4 = 0.0053017520$$
$$s_6 = -0.00038498967$$
$$s_8 = 3.5993303x10^{-5}$$
$$s_{10} = 0.0$$

and for the 100 mbar surface:

$$r(\cos\theta) \approx s[1 + \sum_{n=1}^{5} s_{2n}(s) P_{2n}(\cos\theta)] \text{ (A4a)}$$
$$s = 58276.369 \text{ (A4b)}$$
$$s_0 = -0.00097470685$$
$$s_2 = -0.069879088$$
$$s_4 = 0.0053361290$$
$$s_6 = -0.00038920046$$
$$s_8 = 3.6519296x10^{-5}$$
$$s_{10} = 0.0$$

When is it Safe to Look at the Saturn during a Solar Occultation?

Scott G. Edgington, Andy P. Ingersoll, and David Seal

The question of when it is safe to view Saturn when Cassini is passing thru the shadow of Saturn occurred multiple times during the mission. Following a solar occultation ingress and prior to egress, Cassini scientists would often want look at Saturn and/or the rings. Such situations often would violate the flight rules designed to prevent damage to the optical remote sensing instruments. However, since the Sun was safely being occulted by Saturn, these flight rules could be waived. The flight team often opted for conservatism by requiring the direct line of sight to the Sun to occur at pressure levels greater than the one bar pressure level. No formal documentation of this particular issue was produced by the Saturn Atmospheric Modeling Working Group. However, the following is taken from email threads written at the time and represents the guidance that we were providing to the project.

From: Andrew Ingersoll <api@gps.caltech.edu>
Subject: **Re: Shape of constant pressure surfaces**
Date: November 3, 2009 at 6:06:21 PM PST
To: "Edgington, Scott G (317D)" <scott.g.edgington@jpl.nasa.gov>
Cc: "Darrell F. Strobel" <strobel@jhu.edu>, "Flasar, F M. (GSFC-6930)" <f.m.flasar@nasa.gov>, "Edgington, Scott G. (JPL-317D)[Caltech-JPL]" <scott.g.edgington@nasa.gov>, Don Shemansky <dons@hippolyta.usc.edu>, Ron Vervack <Ron.Vervack@jhuapl.edu>, "Seal, David A. (JPL-313C)[Caltech-JPL]" <david.a.seal@nasa.gov>, "French, Richard G (4500-Affiliate)" <rfrench@wellesley.edu>, "West, Robert A. (JPL-3222)[Caltech-JPL]" <robert.a.west@nasa.gov>, "Pappalardo, Robert T. (JPL-3220)[Caltech-JPL]" <robert.t.pappalardo@nasa.gov>, "Schinder, Paul J (4500-Affiliate)" <schinder@astro.cornell.edu>, "Ingersoll, Andrew P (4500-CalTech)" <api@gps.caltech.edu>

Scott,

It could be phrased as a defined ellipsoid if you made the ellipsoid a function of distance to the spacecraft. It's really a constraint on the bending angle alpha, which cannot be too small because then the ray is passing too high and will not be scattered or absorbed. Something like the following:

Don't look back at the planet during a solar eclipse unless the direct line to the Sun intersects an ellipsoid defined by the equation

$$r^2 + z^2 * e^2 = (a_0 - alpha*R)^2$$

Here r and z are cylindrical coordinates on the surface of the ellipsoid, e is the ratio r_equat/r_polar for the NAIF/SPICE reference ellipsoid, a_0 is the equatorial radius r_equat of the NAIF/SPICE reference ellipsoid, R is the distance between Cassini and Saturn, and alpha is the critical angle - about 0.01 radians or 0.6 degrees.

A modification of the NAIF/SPICE reference ellipsoid is probably good enough. At my request, Mike Flasar and Paul Schinder have provided us with radio occultation data that would define the shape more carefully, but it won't matter except possibly on the proximate orbits. At R = 2.5 Rs from Saturn, requiring that the Sun be 0.6 degrees below the reference ellipsoid translates to alpha*R = 1580 km below the reference ellipsoid. As long as the reference ellipsoid approximates the opaque

layer (e.g., the 500 mbar pressure level) to +/- 50 km, then we are OK. During the proximal orbits we won't be looking that close to the bright limb anyway, because there's not time to turn the spacecraft away when the Sun pops out. The information that Mike Flasar and Paul Schinder did is still useful, but probably not for this solar occultation constraint. I will still use their data to generate a table of constant pressure surfaces.

Andy

From: Andrew Ingersoll <api@gps.caltech.edu>
Subject: **Re: Action Items - Proximal Mission Atmospheric Models**
Date: October 31, 2009 at 12:49:22 PM PDT
To: "Edgington, Scott G (317D)" <scott.g.edgington@jpl.nasa.gov>
Cc: "Darrell F. Strobel" <strobel@jhu.edu>, "F M. (GSFC-6930) Flasar" <f.m.flasar@nasa.gov>, Don Shemansky <dons@hippolyta.usc.edu>, Ron Vervack <Ron.Vervack@jhuapl.edu>, "Seal, David A (313C)" <seal@jpl.nasa.gov>, "French, Richard G (4500-Affiliate)" <rfrench@wellesley.edu>, "West, Robert A (3222)" <robert.a.west@jpl.nasa.gov>, "Ingersoll, Andrew P (4500-CalTech)" <api@gps.caltech.edu>

Hello everyone,

I got worried about the brightness of the refracted Sun and safety constraints when looking back at the planet during a solar occultation. Since time is short, I decided to derive it myself. Here's the summary statement: The instruments are safe if the Sun is a certain angle below the horizon as viewed from the spacecraft. That angle depends on extinction due to clouds and haze as well as on how much sunlight the instruments can tolerate. I need help with those numbers, but assuming the tangent ray is fully extinguished if it passes deeper than the 100 mbar level, the angle is 0.0043 radians.

Start with the bending angle of a ray that passes tangentially through an atmosphere with a density scale height H, where H << R, and R is the radius of the planet. The estimate is valid for small angles and spherical planets, and the numerical constants are approximate.

angle = C (n-1) sqrt(R/H), where C = 2.5. For hydrogen, (n-1) = (1.4E-04)(P/1 bar)(273/T)

This formula gives angle = 0.024 at 1 bar, and angle = 0.0043 at 100 mbar. The units are in radians. Depending on where you think the clouds and haze are, the spacecraft is safe if the angle between the straight line to the Sun - a line that passes through the planet - and the top of the haze layer is greater than the bending angle. For example, if the spacecraft is at 40 Rs and the top of the opaque layer is at 100 mbar, then the sunlight will not reach the spacecraft if the sun is 0.172 Saturn radii below the nominal limb. This number is just (angle)(range) = 0.0043*40 Rs = 0.172 Rs. Things are ~10 times better if the opaque layer extends up to 10 mbar, and they are ~10 times worse if the atmosphere is clear above the 1 bar level. In that case the Sun has to be 0.024*40 Rs = 0.96 Rs below the horizon, which means even with the Sun on the straight line through the center of the planet, sunlight will be reaching the spacecraft.

It's not really that bad, because refractive de-focusing will diminish

the amount of sunlight reaching the spacecraft even if the atmosphere is clear. The reduction factor F (large is good) goes as angle*(d/H), where d is the distance between the spacecraft and Saturn. For the 1 bar case, angle = 0.024, H = 51 km, d = 40 Rs, I get

F (refractive de-focusing at 1 bar, d = 40 Rs) = angle*(r/H) = 1136

F (refracitve de-focusing at 100 mbar, d = 40 Rs) = 296

These factors help, but the Sun is a pretty bright source and even reducing it by three orders of magnitude might not protect the instruments. I need help with two questions: At what pressure level does a tangent ray pass through the atmosphere without significant extinction? How much sunlight relative to the unattenuated Sun at Saturn can the instruments tolerate?

We have some data from the famous eclipse mosaic (PIA08329), where the range was ~36 Rs (2.2E06 km). The Sun is about 0.3 Rs below the horizon in that mosaic. It's not very bright, but you can still see it. If the light were getting through at the 1 bar level, the refracted Sun would wrap all around the planet. Since it doesn't, I infer that the opaque layer extends up to the ~100 mbar level. A combination of extinction and refractive de-focusing is bringing the sunlight down to manageable levels.

I would appreciate comments and help with information about haze layers and instrument tolerances.

Andy

"Seal, David A (313C)" <seal@jpl.nasa.gov>
Re: S56 - DOY359/360 LMB Uncertainties
To: "Roumeliotis, Chris (317B)" <chris.roumeliotis@jpl.nasa.gov>
Cc: "Martin, Nicole P (4500-Affiliate)" <nicole@ciclops.org>, brad <bwallis@frazmtn.com>, "Jones, Jeremy B (3430)" <jeremy.b.jones@jpl.nasa.gov>, "s56_leads@cdsa.jpl.nasa.gov" <s56_leads@dcs04.jpl.nasa.gov>, "Roth, Duane C (343J)" <duane.c.roth@jpl.nasa.gov>, rs <rs@jpl.nasa.gov>, "Grazier, Kevin R (317D)" <Kevin.R.Grazier@jpl.nasa.gov>, "Burk, Thomas A (343S)" <thomas.a.burk@jpl.nasa.gov>, "Scott G. Edgington" scott.g.edgington@jpl.nasa.gov

We are definitely cutting it very close. If we exit the 12.0 deg cone at 360T00:10:58 (or 11:05?) this is three minutes and change later than what I would have done.

If you hammer on the conservatism a bit, you can reduce my "complications" down to 25 sec (solar limb exposure) + 15 sec (1 bar level) + 17 sec (for nav) = about one minute, or 360T00:11:18. That's a minimum margin of ~20 sec. I think that's too small.

Also Jerry dropped off an updated plot; our numbers agree pretty well now, updated text as follows. Changes only to the third paragraph. FYI if you use Jerry's egress time, that wipes out all 20 sec of margin.

So all of this is my own analysis and I wouldn't bet the safety of instruments on it unless it agrees with a bunch of other people's own analyses. Remember we missed the plume on a radio occ some years ago because we got the direction of light time wrong. Anyway:

My events program run on 091005 has the occ at **359T20:41:28 - 360T00:12:18**. This is computed as when the center of the Sun pierces the oblate spheroid defined as 60330 km x 54438 km. These times are exactly the same as they were for 090721, and within four seconds of the EVENTS 091005 run which uses the same Saturn shape. This

shape is close to the 100 mbar level, as opposed to the 1 bar level which is the official IAU convention and what Jerry is using. So Kevin's and my program are agreeing quite well, and things haven't changed.

If I use 60268 x 54364, which is what Jerry uses, I get ingress and egress at 359T20:41:40 - 360T00:12:12. Nav gets 259T20:41:05 - around 360T00:12:00. That's pretty close.

Here are my list of "complications", or uncertainties, what you will, that I would think about:

1. Time it takes one-half of disk of the Sun to travel across Saturn at this time: 25 sec
2. Light time Cassini-to-Saturn: 1-2 sec
3. Time it takes the center of the Sun to travel about one scale height in atmosphere (which is up to ~ 120 km; adjusted for obliquity of trajectory with respect to Saturn contours of equal atmospheric density): 15 sec
4. Navigation uncertainties in trajectory: 17 sec three-sigma
5. Spacecraft clock uncertainties: small
6. Stuff I haven't thought of or screwed up: 120 sec

I would put all this together and say that the maximum time that *I personally* would be comfortable violating sun-pointing flight rules would be the point at which the outermost limb of the sun gets to about, let's say, 100 Earth atmospheres (that's 7 scale heights below the 100 mbar surface, i.e. e^7 = 100), plus the various other "complications". So that's 7 * 15 sec + 25 sec + 2 sec + 17 sec + 120 sec = 4 minutes 30 sec inside of the quoted 091005 occ time.

In other words, **flight rules can be waived from 359T20:45:58 - 360T00:07:48,** in Dave's humble opinion.

The ISS observation is 359T21:23 - 360T00:37. Obviously, the start is fine. As for the end, that depends on where the turn to waypoint starts. Someone needs to make sure you're far enough off ISS-to-Sun by 00:07:48. Enceladus is 26 degrees from the Sun at that time (and getting further away).

Dave

David Seal (818)354-2707 work
Mission Planning Lead, Cassini Mission to Saturn (818)434-7935 cell
Supervisor, Mission Engineering and Planning group http://space.jpl.nasa.gov
Jet Propulsion Laboratory, NASA / Caltech